

**IMAGING MASS SPECTROMETRY OF  
POLYMERIC MATERIALS**



The work described in this thesis was performed at the  
FOM Institute AMOLF  
Science Park 104  
1098 XG Amsterdam  
The Netherlands

ISBN/EAN: 978-90-77209-38-7

Imaging mass spectrometry of polymeric materials  
2009, L.A. Klerk (l.a.klerk@gmail.com)

A digital copy of this thesis can be downloaded from [www.amolf.nl](http://www.amolf.nl). Paper copies are available through the library of the FOM Institute AMOLF ([library@amolf.nl](mailto:library@amolf.nl)).

**IMAGING MASS SPECTROMETRY OF  
POLYMERIC MATERIALS**

**PLAATSOPGELOSTE MASSASPECTROMETRIE VAN  
POLYMERE MATERIALEN**  
(met een samenvatting in het Nederlands)

Proefschrift

ter verkrijging van de graad van doctor aan de Universiteit Utrecht op gezag van de rector magnificus, prof.dr. J.C. Stoof, ingevolge het besluit van het college voor promoties in het openbaar te verdedigen op woensdag 9 december 2009 des middags te 4.15 uur

door

Leendert Aart Klerk

geboren op 6 december 1982  
te Eindhoven

Promotor: Prof.dr. R.M.A. Heeren

This thesis was financially supported by funding from the Strategic Research Fund (SRF) of ICI plc (now part of Akzo Nobel). Part of this work was done in the framework of the Computis Program, 6th European Framework Program for Research and Technological Development (FP6), project no. LSHG-CT-2005-5181194. The imaging MS facilities were supported by the "Stichting voor Fundamenteel Onderzoek der Materie (FOM)", which is financially supported by the "Nederlandse organisatie voor Wetenschappelijk Onderzoek (NWO)".

*Voor mijn ouders*



# TABLE OF CONTENTS

<b>1</b>	<b>INTRODUCTION</b>	<b>11</b>
1.1	General introduction	11
1.2	Mass spectrometry	13
1.3	Scope of the thesis	14
<b>2</b>	<b>IMAGING MASS SPECTROMETRY: FUNDAMENTALS, INSTRUMENTATION AND SAMPLE PREPARATION.</b>	<b>15</b>
2.1	Introduction	15
2.2	Ionization techniques in mass spectrometric imaging	17
2.2.1	Secondary Ion Mass Spectrometry	17
2.2.2	Laser Desorption and Ionization techniques	24
2.2.3	Other techniques	27
2.3	Mass analysis techniques	28
2.3.1	Time of flight MS	29
2.3.2	FTICR-MS	32
2.4	Imaging mass spectrometry	33
2.4.1	Microprobe mode MS imaging	33
2.4.2	Microscope mode MS imaging	34
2.5	MS imaging instrumentation used for this work	35
2.5.1	TRIFT imaging systems for TOF-SIMS and MALDI-TOF	35
2.5.2	Other (imaging) MS instrumentation	37
2.6	Sample preparation techniques	38
2.6.1	Sample handling and treatment	39
2.6.2	Matrix deposition	40
2.6.3	Sample metallization	42
2.7	Complementary techniques	45
2.7.1	Optical microscopy	45
2.7.2	FTIR imaging	45
2.7.3	Regular MS techniques	45
2.8	Data analysis	46
2.8.1	Data pre-treatment	47
2.8.2	Manual data exploration	47
2.8.3	Automated data exploration	48
2.9	Polymer mass spectrometry	49

Table of contents

2.9.1	Polymer properties commonly identified by MS	50
2.9.2	Analytical techniques	51
2.10	Current status in imaging mass spectrometry	54
<b>3</b>	<b>MASS SPECTROMETRIC IMAGING OF POLYMER SYSTEMS</b>	<b>55</b>
3.1	Introduction	56
3.2	Experimental challenges	57
3.2.1	Sample preparation	57
3.2.2	Data acquisition techniques	60
3.3	Data analysis matters	61
3.3.1	Manual analysis	61
3.3.2	Automated analysis	65
3.4	Conclusions and recommendations	65
<b>4</b>	<b>FAST AND AUTOMATED LARGE-AREA IMAGING MALDI MASS SPECTROMETRY IN MICROPROBE AND MICROSCOPE MODE.</b>	<b>67</b>
4.1	Introduction	68
4.2	Experimental details	70
4.2.1	Instrumentation	70
4.2.2	Spectral detection system	70
4.2.3	Microscope image recording	72
4.2.4	Laser system	73
4.2.5	Materials	73
4.2.6	Sample preparation	73
4.3	Results	74
4.3.1	Whole rat section	74
4.3.2	Droplet standards	76
4.3.3	Rat brain sample: microprobe and microscope imaging MS	77
4.4	Conclusions	77
<b>5</b>	<b>C<sub>60</sub><sup>+</sup> SECONDARY ION MICROSCOPY USING A DELAY LINE DETECTOR</b>	<b>79</b>
5.1	Introduction	80
5.2	Experimental	83
5.2.1	Mass microscopy	83
5.2.2	Mass spectrometric imaging in microprobe mode	83
5.2.3	C <sub>60</sub> primary ion gun	83
5.2.4	Delay line detector	84
5.2.5	Colored TEM grids	85



5.2.6	Imaging of a hybrid polymer-tissue sample	85
5.3	Results	87
5.3.1	Comparison of image quality between microscope and microprobe modes	87
5.3.2	Comparison of spectral quality between microscope and microprobe modes	88
5.3.3	Large area imaging	90
5.3.4	On-tissue imaging	91
5.4	Discussion and conclusions	92
<b>6</b>	<b>DATA ANALYSIS STRATEGIES IN IMAGING MASS SPECTROMETRY</b>	<b>93</b>
6.1	Introduction	94
6.2	Experimental	96
6.2.1	Sample preparation	96
6.2.2	Data acquisition	97
6.2.3	Data preprocessing	98
6.3	Methods for multivariate analysis	100
6.3.1	PCA	100
6.3.2	PCA and VARIMAX	101
6.3.3	PARAFAC	102
6.3.4	3D visualization of extracted features	103
6.4	Results	103
6.4.1	PARAFAC	103
6.4.2	PCA on sparse datasets	107
6.4.3	VARIMAX post-processing	110
6.4.4	Computation time vs. results	113
6.4.5	3D visualizations	115
6.5	Conclusions and discussion	117
<b>7</b>	<b>MASS SPECTROMETRIC IMAGING OF A POLYMERIC HYDROGEL IMPLANT</b>	<b>119</b>
7.1	Introduction	120
7.2	Experimental	122
7.2.1	Sample preparation	122
7.2.2	Histological staining	123
7.2.3	Comparison with in vitro polarized macrophages	124
7.2.4	Statistical data analysis	125
7.3	Results	126

## Table of contents

7.3.1	Hydrogel implantation	126
7.3.2	Macrophage standards	131
7.3.3	Combining knowledge from macrophage standards with the hydrogel implant	131
7.4	Discussion and outlook	134
	<b>BIBLIOGRAPHY</b>	<b>137</b>
	<b>SUMMARY</b>	<b>153</b>
	<b>SAMENVATTING</b>	<b>157</b>
	<b>DANKWOORD</b>	<b>161</b>
	<b>CURRICULUM VITAE</b>	<b>163</b>
	<b>LIST OF PUBLICATIONS</b>	<b>165</b>
	Publications	165
	Presentations at conferences	165

# 1 INTRODUCTION

## 1.1 *General introduction*

An old proverb says “a picture is worth a thousand words“. In mass spectrometry, this could be changed into “a picture is worth a thousand spectra”\*. The original proverb refers to the fact that it is much easier for the human brain to interpret data that is visualized in an image, than when it is written down. In mass spectrometry (MS), the same holds. A large collection of mass spectra can, although information-rich, easily get the analyst lost in interpretation. Not to even talk about presenting the data to a less-experienced audience. One of the key powers of imaging MS lies in exactly the fact that molecular distributions can be visualized in an intuitive manner. Imaging MS is therefore a solution to making data more insightful when MS data is obtained from samples that have different spatial origin.

Being part of the solution, imaging MS is part of the problem too. The fact that a mass spectrum is measured at a raster of positions on a surface, results in a tremendous amount of data. The increased amount of data, in turn, makes it more difficult to interpret. However, both analysis and, more importantly, presentation can still be based on images and therefore this is more of a mass spectrometrists’ problem rather than a general problem. Eventually, the data can still be presented in an insightful way, i.e. by using images. And images tend to appeal to the general audience, which is especially important in modern-day science, which often involves multi-disciplinary collaborations and in which the call for valorization demands the presentation of scientific results in an increasingly insightful way.

Although imaging MS has been around for quite some time already, it has become increasingly popular during the last decade. The first broadly applied and commercially available imaging mass spectrometers were secondary ion mass spectrometers. The recent developments in imaging MS have mainly taken place in the matrix assisted laser desorption and ionization (MALDI) imaging MS field. These developments originate from the impact this technique has made in life sciences. Secondary ion mass spectrometry (SIMS) has made an increasing impact in life sciences as well. Although its origin in inorganic analysis has long been broadened to materials analysis in general, including polymer analysis, biological applications are more recent and still scarce. The development of more efficient primary ion sources as well as the development of surface modification techniques have increased the

---

\* This proverb has been paraphrased like this before, albeit in a different context.

effective mass range of SIMS and consequently its usefulness in the analysis of biologically relevant molecules.

Even though SIMS and MALDI are two completely distinct techniques, the vast majority of the challenges that are faced in imaging mass spectrometry hold for both the techniques. Therefore, many novel methodologies that are developed for one of these techniques can as well be applied for the other.

In the imaging mass spectrometry field, just like in any other imaging field, there is an ever-lasting demand of more detail in both the spectral and the image dimension. In connection to this, there is the demand of faster acquisition of larger samples. These demands require extensive instrumental improvements, dealing with novel detection methods and instrument automation to cope with the lower number of atoms that can be probed from a smaller area per pixel (table 1.1) and expanding analysis areas.

With the increase of resolution and acquisition speed, the amount of data that is generated grows explosively (table 1.1). Apart from data-storage issues, which are more of an information technology issue, data analysis becomes more complex as the size and complexity of the dataset increase. Consequently, data analysis of data that is measured within a single day can take more than a week. To make life easier and interpretation faster, automated methods are developed. Most of these methods are based on statistical mathematical routines that make correlations within the dataset insightful.

**Table 1.1** A simple overview of data explosion due to resolution improvement \* a single spectrum file size of 100 kB is assumed. †  $10^{13}$  atoms/mm<sup>2</sup> is assumed.

<b>area (mm<sup>2</sup>)</b>	<b>number of pixels</b>	<b>Resolution (<math>\mu</math>m)</b>	<b>data size* (MB)</b>	<b>Number of atoms/pixel†</b>
1	16	250	1.56	6.3E+12
1	64	125	6.25	1.6E+12
1	256	62.5	25	3.9E+11
1	1024	31.25	100	9.8E+10
1	4096	15.625	400	2.4E+10
1	16384	7.813	1600	6.1E+09
1	65536	3.906	6400	1.5E+09

All these developments leave a lot of work for further improvement of the technique. On the other hand, these improvements offer new opportunities for the molecular imaging of scientifically relevant samples. Improvement of MS imaging techniques improves materials analysis and makes it possible to unveil more biological

information from histological tissue sections and cell samples. The combination of these two makes it even more unique and offers application possibilities in biomaterials engineering. Unlike classical histological staining methods, which are often incompatible with polymer samples and classical materials analysis methods which are insensitive to biological activity, imaging MS can visualize molecular information of both the biomaterial and the biological activity in a single image.

## ***1.2 Mass spectrometry***

Mass spectrometry (MS) is an analytical technique that is used to determine the mass of chemical compounds. Because the mass of a chemical compound is dependant on its elemental composition, it is an important measure for its identity

The introduction of what was later called a mass spectrograph was in 1920 by Aston, got him the 1922 Nobel Prize in Chemistry “for his discovery, by means of his mass spectrograph, of isotopes, in a large number of non-radioactive elements, and for his enunciation of the whole-number rule”. Since then, mass spectrometry has gradually grown from a very specialist analytical technique into a mature technique that is widely used on a routine basis. Fields of application include biology, medicine, forensics, organic and inorganic chemistry, materials engineering, food engineering and many others. Both in academia and in industry, MS is a widespread technique.

Typically, MS is not used as a stand-alone technique, but combined with one or several steps of separation techniques. These separation techniques include gas chromatography (GC), liquid chromatography (LC), solid phase microextraction and virtually any other analytical separation technique. Coupling of separation techniques to MS can either be indirect, in which separation is done in a stand-alone experiment and followed by a MS experiment, or directly in which both are combined in a single setup. The latter method (e.g. LC-MS) is very common for routine analysis of all kinds of complex mixtures.

To determine their mass, chemical compounds need to be brought into the gas phase, ionized, separated based on their mass and detected. All these steps are crucial in the successful generation of a mass spectrum. Gas phase ions are typically generated in vacuum or transferred into vacuum directly after they are created. Methods to do this include, but are not limited to, electron impact ionization (EI), electrospray ionization (ESI), (matrix assisted) laser desorption and ionization ((MA)LDI) and secondary ion mass spectrometry (SIMS). This thesis focuses mainly on SIMS and MALDI. The combination of several ionization techniques can be used to combine their specific advantages and generate complementary data. In most cases, the analytes are brought into the gas phase and ionized in a single step.

After bringing ions into the gas phase and into the vacuum, they have to be separated based on mass and detected. Mass analysis can be done using sequential mass filtering, in which ions that fit in a single mass window are transmitted and all other ions are blocked. The mass window is scanned and an ion intensity is detected for each mass window. Sequential filtering methods include quadrupole filtering and magnetic sector filtering. More efficiently, all present gas phase ions are analyzed in a single MS-run. The latter method is much more efficient because the loss of ions that is inherent to the sequential filtering method is circumvented. Methods that detect all ions in a single measurement step include fourier transform ion cyclotron resonance mass spectrometry (FTICR-MS), Orbitrap mass spectrometry and time of flight mass spectrometry (TOF-MS). Combinations of mass filters and mass analyzers are very common. In this thesis, most analysis is done using TOF analyzers. In the case of TOF-MS, ions that are given equal kinetic energy are detected after separation based on their flight time through a time of flight tube using fast acquisition electronics.

### *1.3 Scope of the thesis*

To do imaging MS, various steps have to be made and all have to be optimized. Sample preparation is a key issue in imaging MS, instrumentation needs to be optimized and sometimes adapted and the acquired data needs processing and analysis. All these subjects are covered in this thesis. A general introduction on MS, imaging MS and related, complementary, techniques is given in **chapter 2**. **Chapter 3** discusses the possibilities and challenges that are faced in the mass spectrometric imaging of polymers. Instrumentation developments are given in **chapter 4** and further elaborated on in **chapter 5**. Data acquisition results in very large datasets. When one knows what to look for it can be fairly straightforward to extract information from this data. However, one of the major advantages of imaging MS is the possibility to explore samples without any prior knowledge. To do this in an efficient way, statistical data processing methods are needed, which **chapter 6** is about. Finally all these subjects come together and are applied on a sample that combines biological and polymeric features in **chapter 7**. The simultaneous analysis of both polymer material and biological activity shows the power of MS imaging to chemically analyze diverse samples.

## **2 IMAGING MASS SPECTROMETRY: FUNDAMENTALS, INSTRUMENTATION AND SAMPLE PREPARATION.**

### ***2.1 Introduction***

A thorough understanding of the fundamentals of imaging MS is crucial to allow the further development of technology, sample preparation methodologies, data acquisition methods and data analysis strategies. A successful imaging mass spectrometry experiment starts with the preparation of the sample, including several sample pre-treatment methods. After this, the actual MS experiment is done, followed by the analysis of the data. For each of these steps, the method of choice depends on the information that is aimed for. Different types of samples require different sample preparation methods, dependant on the type of molecular information. The same sample can give completely different data depending on the sample preparation that is used. The sample preparation used needs to match the used data acquisition method.

The data acquisition method is another determining parameter for the type of data that is obtained. The way molecules are brought into vacuum, ionized, separated based on their mass and detected has to be chosen on accordance with the searched information. Different methods have different capabilities, depending on specimen type, mass range, spatial resolution, spectral resolution, chemical information and the possibility to perform additional analysis on the ionized ions like fragmentation or spectroscopy. The data acquisition method determines the type of data that is obtained, which influences the method of data analysis.

After finding the right combination of sample preparation and data acquisition, an enormous amount of data needs to be analyzed. Data analysis strategies are needed to extract information from this data. Manual methods, unsupervised automated methods or supervised automated methods can be used for this purpose, but typically they are combined. Data analysis often takes most of the researcher's time in imaging mass spectrometry applications; therefore the development of good methods is very important.

The proper combination of these three main steps in the MS imaging experiment, offers tremendous opportunities for the application of imaging MS as an imaging tool for solving complex scientific challenges. Possible applications in which MS imaging can add value are in science, medicine, pharmaceuticals development and (bio)materials engineering. The fact that imaging MS can be used for the analysis of small and large biological molecules as well as synthetic molecules ranging from

small functional compounds up to long-chain polymers, makes it a very versatile tool, especially when analyzing complex systems. In order to cope with increasing complexity and to be useful as a wide-range applicable analytical tool, there still are some major hurdles to be taken.

Matrix effects are a major issue in MS imaging, irrespectively the ionization technique that is used. Matrix effects, also called ion suppression effects, are caused by the fact that different compounds have different ionization efficiencies. As a result, the easier ionizable compound will suppress the signal of a compound that is ionized much more difficultly. In an imaging experiment, this means that the concentration distribution of one compound can influence the MS imaging intensity distribution of another compound that is evenly distributed<sup>1-3</sup>, leading to an unreliable quantitative comparison in the images produced by imaging MS. Not only the molecular, but also the structural environment influences the intensity of the analyte signal. Several solutions have been proposed to this, including the application of a calibration standard on a blank sample to assess the ion suppression effect for that specific compound<sup>4</sup>. Running good calibration standards to circumvent ion suppression is important to give reliable distribution maps and inevitable when quantification is needed.

Characterization of compounds is another issue that requires close care. Quite often, an assessment of the molecular structure that belongs to a peak can be made based on correlating peaks or prior knowledge about the sample. In case of sufficiently high mass resolution, molecular formulas can be assigned to peaks based on their accurate mass measurement. These methods do however rely on indirect evidence. To be certain about a structure, MS/MS experiments are necessary. This is getting more focus in the imaging MS field nowadays. MALDI MS imaging instruments now often have MS/MS capabilities. In the SIMS field, traditionally a field in which people were looking at characteristic fragment ions and elements, the capability of detecting high-mass secondary ions now also requires MS/MS methodologies. Unfortunately, tandem SIMS instruments are still very experimental<sup>5, 6</sup> and not currently commercially available, but they certainly will be in the near future.

This section gives a wide-range overview of the analytical possibilities and challenges in imaging mass spectrometry. Most of the imaging MS issues are covered, the focus is however on the techniques that were used for this thesis and related work.

Although the experimental steps are in a different order, the data acquisition methods are explained first. A good understanding of data acquisition possibilities is necessary to understand the issues related to sample treatment. Being the last step in the experimental process, data analysis is discussed next. Because this thesis has an



application focus in polymer analysis, an overview of the most important aspects in polymer mass spectrometry is given at the end of this chapter.

## ***2.2 Ionization techniques in mass spectrometric imaging***

To determine the mass of compounds from a surface, they need to be both desorbed and ionized. Several methodologies are in use for this purpose. The two most common techniques, also the techniques that were used for this work, are secondary ion mass spectrometry (SIMS) and laser desorption and ionization (LDI) mass spectrometry. SIMS uses an ion beam to generate ions from a surface with little or no sample preparation. LDI uses a laser beam to generate ions from the surface. The most common type of LDI is matrix assisted laser desorption and ionization (MALDI). For MALDI, a matrix layer is needed to assist the desorption and ionization of the analytes by the laser light. This involves extensive sample preparation but has the advantage of making the imaging of large, intact molecules possible whereas SIMS is generally limited to small molecules and molecular fragments.

This subsection focuses on the fundamentals of the SIMS and MALDI ionization techniques and gives a brief overview of other ionization techniques that can be applied for imaging.

### **2.2.1 Secondary Ion Mass Spectrometry**

The observation of ion and neutral particle generation at the surface through ion bombardment was first observed by the British physicist J.J. Thomson in 1910. After improved vacuum technology, this principle was used for mass spectrography (figure 2.1) in the late 40s and 50s of last century<sup>7,8</sup>. Further development was taken up by Benninghoven who improved acquisition sensitivity by introducing single-ion counting techniques and therefore made static SIMS possible.

Secondary ion mass spectrometry (SIMS) is a technique in which surface material from the sample specimen is sputtered away using an ion beam. A brief explanation of the technique is given in this section. A thorough explanation of the TOF-SIMS technique is given in a book edited by Vickerman and Briggs<sup>9</sup>.

SIMS is a widely used technique to analyze the chemical composition of solid surfaces and thin films. It can be applied to analyze both the elemental and the molecular composition of the surface. In the latter case, ion beam induced chemical damage to the surface plays an important role. Therefore, the amount of primary ions that is used for a certain surface area should not be too high. Static SIMS is a regime of SIMS in which only a small part of the surface is exposed to the primary ion beam. In this

regime, each measured secondary ion originates from an untouched part of the surface and is therefore representative for the measured surface. The possibility to do static SIMS, extended the SIMS technique from an elemental analysis technique to a molecular analysis technique. The static limit can be determined by calculating the lifetime  $t_m$  of the topmost atomic layer of the measured surface. It depends on the surface area exposed to the beam  $A$  in  $\text{cm}^2$  (with a typical  $10^{15}$  atoms per  $\text{cm}^2$ ), the primary beam flux density  $I_p$  and the sputter yield  $Y$  through the following relation:

$$t_m = \frac{10^{15} \cdot A}{I_p Y} \quad 2.1$$

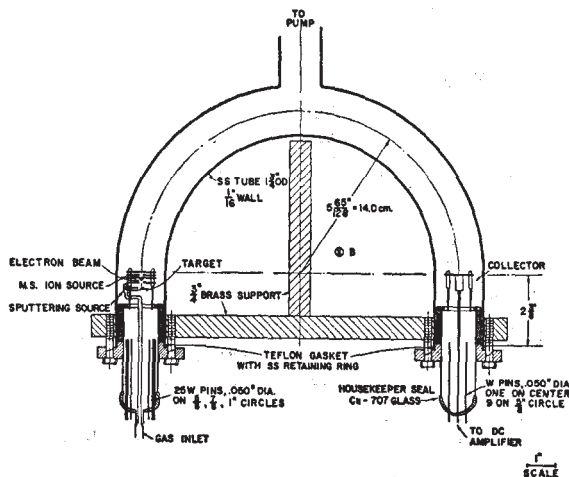


**Figure 2.1** The first secondary ion mass spectrometer by Honig was a  $180^\circ$  magnetic sector instrument (image taken from literature<sup>8</sup>).

In general, each primary ion is assumed to affect an area of about  $10 \text{ nm}^2$  so that an ion dose of  $10^{13}$  impacts  $\text{cm}^{-2}$  is the generally accepted static limit. The area of effect does however get larger with increased primary ion size and the use of cluster ions, so that this measure only holds for atomic primary ions. Note that the static limit is merely a theoretical measure that assures a certain chance of hitting a part of the surface that was not damaged by the ion beam. It does not mean that the affected area cannot give representative signal for the sample.

### 2.2.1.1 Primary ion sources

There is no real limitation to the type of ion used as a primary ion for SIMS but there is a large number of properties to consider when choosing a primary ion source. The primary ion source of choice depends on the goal of the analysis. First generation primary ions were inert gas ions ( $\text{Ne}^+$ ,  $\text{Ar}^+$ ,  $\text{Kr}^+$  and  $\text{Xe}^+$ ) at 30-400 eV<sup>8</sup>. These were duoplasmatron sources, a method of ion generation that is not common as a primary ion source anymore but still widely used as a sputtering source for depth profiling experiments. Mass analysis was typically performed with a magnetic sector analyzer or a quadrupole mass filter and therefore mass-sequential. Duoplasmatron sources were then followed by surface ionization sources, typically generating  $\text{Cs}^+$  ions<sup>10</sup>.  $\text{Cs}^+$  sources are still widely used, especially as sputter source. The introduction of the very bright liquid metal ion source (LMIS) made primary ion pulsing and therefore time-of-flight analysis possible (see chapter 2.3.1). A LMIS consists of a metal reservoir with a very thin (<1  $\mu\text{m}$ ) tungsten tip. Because the metal is liquid, if needed by heating it, a thin layer of metal is formed around the tip. This tip is placed in a very high (10s of kV) extraction field. The extraction field causes an instability in the liquid metal film comparable to a Taylor-Gilbert cone<sup>11</sup>. As a result, ions are extracted from the tip of the source through the field. A LMIS is typically operated at 10-25 keV primary ion energy. Examples of LMIS generated ions are  $\text{Ga}^+$ ,  $\text{In}^+$ ,  $\text{Au}_n^{m+}$  and  $\text{Bi}_n^{m+}$ . The latter two class of ions offer the advantage of polyatomic ions and possible multiple charges. Multiple charges give the primary ions a multiple of the energy compared to singly charged ions in the same electric field.

Already quite early in the development of SIMS, it was acknowledged that heavier primary ions yield more high-mass molecular fragments and more secondary ions in general, proven on polymer samples<sup>12</sup>. Only a few years later, comparison of  $\text{Cs}^+$  and  $\text{SF}_6^{(-/0)}$  showed that, at the same energy, poly-atomic ions have much higher ionization efficiencies than mono-atomic ions of the same mass<sup>13,14</sup>. This is due to more superficial and therefore more efficient energy coupling into the surface caused by fragmentation at the surface rather than deep penetration into the surface. This was also shown by molecular dynamics simulations comparing  $\text{Ga}^+$  and  $\text{C}_{60}^+$  primary ions<sup>15-19</sup>. The use of buckminsterfullerene ( $\text{C}_{60}^+$ ) is a quite recent addition to the spectrum of ion sources, offering high secondary ion formation efficiency and low sub-surface chemical damage<sup>20-24</sup>.  $\text{C}_{60}^+$  is readily generated from heat-generated  $\text{C}_{60}$ -vapor that is ionized through electron-impact, gives an high secondary ion formation efficiency<sup>25</sup> and high day-to-day operation stability. In addition,  $\text{C}_{60}$  is cheap, allowing low-cost operation even when doing very large area experiments<sup>24</sup>, especially in comparison with other common primary ion sources like liquid metal ion sources. The low chemical sub-surface damage by  $\text{C}_{60}^+$  primary ions makes

molecular depth profiling and analysis far beyond the static limit possible<sup>6, 26</sup>. Low chemical damage and high secondary ion yields have also been shown for even larger cluster primary ions like Au<sub>400</sub><sup>+</sup><sup>27, 28</sup>.

### 2.2.1.2 Secondary ion generation mechanism

Many computational and experimental studies have been performed on the generation of secondary ions under influence of impinging primary particles. Only the use of ions as primary particles will be discussed here but a large deal of these mechanisms hold for neutral particles as well. There are several aspects of importance in this process: Energy transfer into the surface, desorption of material from the surface, damage done to the surface and ionization of the desorbed material.

#### *Energy transfer into the surface and desorption*

As the primary ion hits the surface, it exerts a force on the molecules it hits. The primary ion transfers energy from to the surface material, resulting in a collision cascade. This leads to a recoil process, generating particles with a velocity in the direction off the surface. Theoretical background on the atomic cascade and recoil processes is given in the book referred to earlier<sup>9</sup>. A more qualitative overview is given elsewhere in literature<sup>29</sup>.

Another part of the imposed primary ion energy is absorbed as thermal energy by the molecules in the surface region. Given the fact that a typical primary ion has an energy of 5-40 keV, only a minute portion of this energy needs to be absorbed and thermalize the molecules to readily break even the strongest molecular bonds, which have a bond energy <10 eV. The impact of the primary ion generates an energy gradient around the impact site. For atomic primary ions, this results in three areas that can be distinguished around the impact site. The molecules close to the impact are destroyed and observed as atomic secondary ions or a-specific molecular rearrangement products, mainly in the mass range below 40 Da<sup>30</sup>. In the surrounding area, enough energy is present to fragment the surface molecules but rearrangement is scarce and specific molecular fragments are generated. Because fragmentation is compound-specific, SIMS could therefore be considered an in-situ fragmentation technique. The outer area delivers low-energy desorbed molecular ( $M^+/M$ ) and quasi-molecular ( $M\pm H$ )<sup>±</sup> as well as large and specific fragment (e.g. H<sub>2</sub>O loss) secondary ions (figure 2.2).

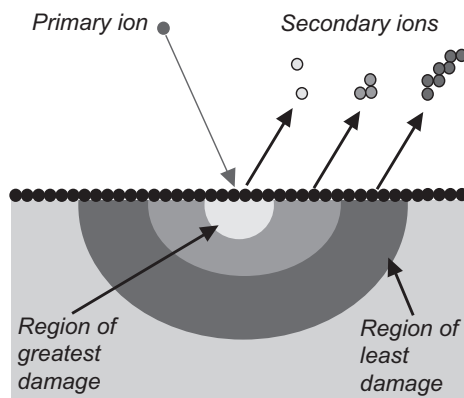


**Figure 2.2** Schematic cross-section of the impact region of a primary ion in SIMS. The center part is the highly energetic region where atomic and rearranged fragment ions are formed, in the region next to this molecular fragment formation is predominant, in the outer region molecular and quasi-molecular ions are emitted. (Figure taken from [www.phi.com](http://www.phi.com)).

Many simulations have been done using molecular dynamics calculations, especially focusing on the explanation of increased secondary ion yield and reduced sub-surface chemical damage when using cluster primary ions<sup>16-19, 30-35</sup>. It was found that the primary ion impact breaks the molecular structure at the surface into pieces, leading to a kinetic energy loss of the impinging ion<sup>35</sup>. After this, the primary ion follows a trajectory through the next layers, several atomic layers down the surface. The primary ion fragments generate most of the molecular ions and molecular fragment ions. An important parameter determining the penetration depth is the stopping power. The stopping power is dependant on the amount of interaction (energy transfer) between the primary ion and the surface and depends on the nature of both the primary ion and the analyzed surface. It is higher for dense surfaces and large primary ions. Due to the low interaction of small atomic primary ions with the surface, these penetrate deeply into the surface causing molecular damage down to 7.5 nm sub-surface (figure 2.3)<sup>18</sup>. The molecular damage depth is much shallower for polyatomic primary ions like  $C_{60}^+$ . One reason for shallower penetration depth of polyatomic, but also high-mass atomic, primary ions is the larger collision cross-section, which leads to interaction with more surface atoms. For polyatomic primary ions, the major reason is however their dissociation in the surface region, which reduces the penetration depth and therefore reduces the sub-surface damage. For  $C_{60}^+$  ions with an energy of 15 keV, the effective energy per atom is only 250 eV. As a result, both energy deposition and damage mainly take place in the first 3 nm sub-surface. Another important advantage of the shallow penetration depth of polyatomic primary ions is the much larger amount of material that is removed per

impact. This results in higher sputter rates and a much higher secondary ion yield. Penetration depth is important in another respect as well. It has been shown for lipid mono- and multi-layers on a metal substrate, that ions do not only originate from the topmost surface layer, but also from sub-surface region<sup>36</sup>. The fact that also sub-surface material is probed, shows that there is considerable mixing of the components present in the topmost layers, as also shown by simulations<sup>37</sup>. It should be noted that the amount of mixing depends on the nature of the sample and could be completely different for organic amorphous substrates.

#### *Ionization mechanisms*

The desorption or sputtering of secondary particles as well as the ionization of secondary ions is of fundamental importance in SIMS. Several suggestions have been made about the underlying mechanisms. It is widely known that most of the secondary particles are neutral and only about  $10^{-3}$  part of the generated particles are ions<sup>9</sup>. One possibility of ion formation is the fragmentation of highly-energetic molecular ions into charged fragments. This presumes a highly polar configuration as the particle leaves the sample surface. This model shows parallels with the desorption-ionization model, in which ions are formed through ion-molecule reactions above the surface in the desorption plume. Another possibility is the pre-formation of ions at the surface which are then physically desorbed. For metallic substrates, this is however in contradiction with the electronic transition times, which are about at least an order of magnitude shorter than the time needed for the sputtered species to cross the near-surface region (about  $10^{-13}$  s), which means that ions would be neutralized before they are desorbed. Things get more complex when analyzing polymer samples. Just like in the model describing three zones with different desorption regimes (figure 2.2), a polymer produces three types of fragments, be it that the generation of molecular species is limited up to polymers with a molecular weight of a few kDa. As a consequence of the long chains polymers have, which can range distances much longer than the diameter of the impact region, molecular damage is much more of an issue for polymer analysis. A study comparing different types of polymers showed large variations in sputter rate between different polymers, which indicates a predominant chemical sputtering process<sup>38</sup>.

The chemical nature of the sample largely determines the ionization efficiencies. Especially salts have been shown to have a strong suppression effect when analyzing biological specimens, which is of crucial importance when comparing peak intensities between samples or within one imaging sample<sup>1</sup>. In addition, the gas-phase basicity of the analytes was shown to play an important role in the formation of secondary ions as well as in ion suppression<sup>2</sup>.

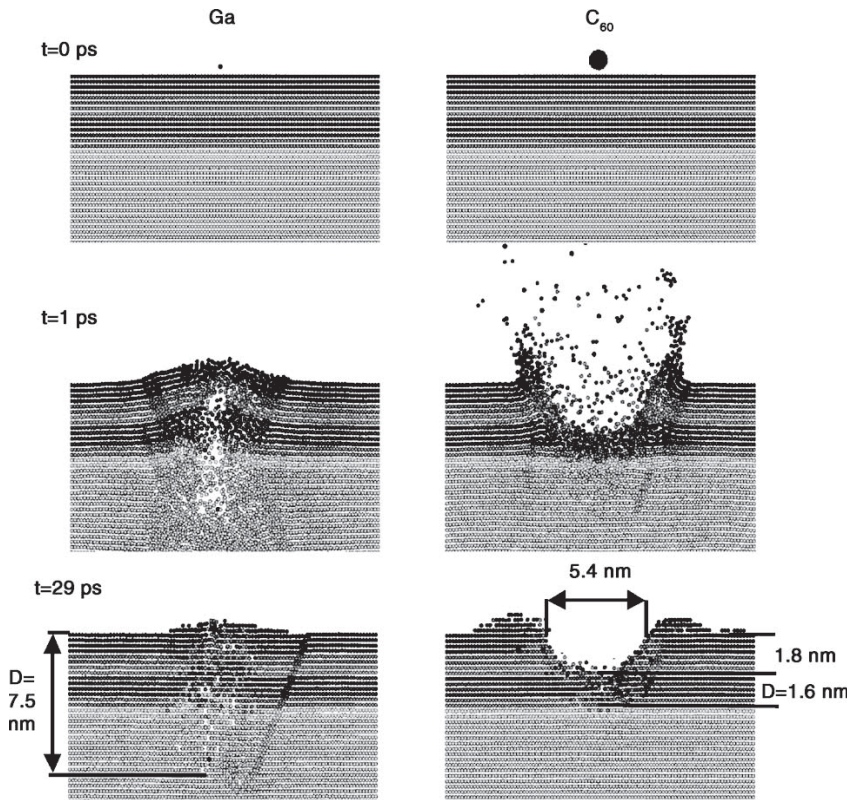


**Figure 2.3** A cross sectional view showing molecular dynamics simulations on the temporal evolution of collision events for Ga and C<sub>60</sub> bombardment at 15 keV energy at normal ion incidence. The figure also shows molecular damage as atomic volume mixing.  $D$  is the maximum depth at which this mixing is observed. Figure taken from literature<sup>18</sup>.

### 2.2.1.3 Surface charging

When SIMS is used for the analysis of insulating materials, surface charging may occur. The deposition of positive primary ions and the emission of secondary electrons at the surface generate a positive charge at the sample surface in positive ion SIMS experiments that is much larger than the amount that is emitted through positive secondary ions. The release of negative ions and secondary electrons in negative ion SIMS has the same, but even stronger, effect. This positive charge buildup on insulating sample surfaces increases the sample surface potential by up to several hundreds of volts. This potential increase moves the primary beam position and influences the secondary ion energy, which is detrimental for both spectral and spatial accuracy of the experiment. Two solutions for this are common:

Preventing charge-buildup by making the surface conductive. This is either done by surface metallization (further detailed out in 2.6.3) or by putting a metal grid on top of the sample. For imaging SIMS, the latter method is generally not preferred, because it limits the view on the sample.

Compensate the charging effect. An electron flood gun delivers low-energy (<50 eV) electrons at the sample surface between the primary ion pulses. These electrons compensate the negative charge loss during the SIMS process. Care should be taken about possible sample surface damage induced by the electrons <sup>39</sup>.

#### **2.2.1.4 Surface modification techniques in SIMS**

The fact that SIMS by nature requires hardly any sample preparation, does not mean that surface pre-treatment cannot be beneficial. Sample surface metallization is often done to enhance the (quasi-) molecular ion yield and reduce surface charging. The use of matrix molecules can be beneficial for the high-mass (quasi-)molecular ion yield in SIMS. This technique called matrix enhanced SIMS (MESIMS) <sup>40-44</sup> was developed to analyze peptides, proteins and other molecules up to a  $m/z$  of 10000 Da at a picomolar concentration. A disadvantage that is inherent to matrix application is the reduced spatial detail that can be obtained. Moreover it introduces inhomogeneity due to the dislocation and concentration of salts in certain parts of the matrix crystal <sup>45</sup>. A broader description of matrix application and gold coating is given in sections 2.6.2 and 2.6.3 respectively.

### **2.2.2 Laser Desorption and Ionization techniques**

Although laser desorption and ionization (LDI) had been known for quite some time before <sup>46-48</sup>, even for the desorption of biomolecules <sup>47</sup>, the real breakthrough of using laser light to generate ions for mass spectrometry came from Karas and Hillenkamp <sup>49, 50</sup> with the introduction of matrix assisted laser desorption and ionization (MALDI). A very extensive description of the desorption process in MALDI is given by Dreisewerd <sup>51</sup>. A highlight of the most important aspects as well as an extension with issues relevant for imaging mass spectrometry is given below.

#### **2.2.2.1 MALDI mechanism**

MALDI is based on the principle of collective desorption in which the analyte molecule is dissolved in a matrix. This matrix can be liquid but is most commonly a solid crystal. Matrix compounds are chosen such that they absorb the laser light by electronic or vibrational excitation through ultraviolet (UV) and infrared (IR) light respectively. Due to this process, a sudden expansion takes place in the solid matrix layer that leads to desorption of the matrix molecules together with the analyte molecules (figure 2.4). During this process, matrix-analyte reactions take place,



resulting in analyte ionization, typically by proton transfer. The extent of ionization is a result of a thermodynamic equilibrium<sup>52</sup>. Furthermore, the high abundance of matrix in the MALDI plume, gives a locally elevated pressure, resulting in collisional cooling.

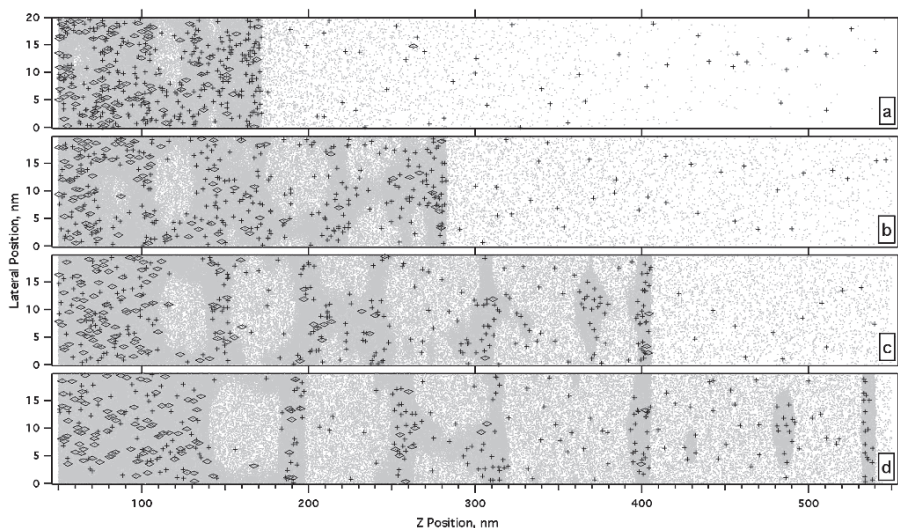


**Figure 2.4** A side-view of the MALDI process as obtained by molecular dynamics simulation. Snapshots of the MALDI plume are given at time intervals. From top to bottom: (a) 500, (b) 750, (c) 1000, and (d) 1250 ps. A distinction between neutral molecules (gray points), positive ions (crosses) and negative ions (diamonds) is made. This image gives a good indication of the process of ion and cluster formation during the MALDI process. Note the positive charge accumulation at the surface, which is due to electron emission from the top 10 nm of the sample. Image was taken from a simulation paper by Knochenmuss et al.<sup>64</sup>.

For an efficient MALDI process, the ratio between analyte and matrix needs to be low enough to reduce interaction between the analytes and have sufficient incident laser absorption. A typical analyte concentration is 1/1000 to 1/100 per matrix molecule, but depends on the size and nature of the analyte as well as the matrix and is often determined by trial-and-error. Unlike generally agreed in the MALDI society for a long time, complete incorporation of the analyte is not necessary as shown by successful dry matrix preparation methods. The amount of desorbed material is highly dependant on the laser fluence. There is a certain minimum laser fluence needed to have proper desorption and ionization, named the MALDI threshold<sup>53</sup>. Above this fluence value, signal increases up to a certain level and below this threshold, there is no signal at all. Too high laser energies lead to in-source or post-source fragmentation of analytes<sup>54-57</sup>. The amount of desorbed analyte and the

amount of fragmented analyte are not only dependant on the fluence, but also on the used matrix and the laser spot size<sup>56, 58</sup>. A decrease in spot size results in an increase of the minimum laser fluence needed for ionization, which is a disadvantage because of increased fragmentation at high laser fluence. This decrease in desorption/ionization efficiency is of crucial importance in the development of MALDI imaging at high image resolution. For high resolution MALDI using a focused laser, the amount of signal per laser shot does not only decrease because of the decreased surface area, but also because of the decreased ionization efficiency.

It is important to realize that the MALDI plume at threshold typically contains a few femtomoles of sample material for laser spot sizes in the order of a few 100  $\mu\text{m}^2$ . This includes clusters, molecules and ions. Only about 1 out of 10000 is an ion, which means that there are in the order of 10-100 analyte ions per laser shot that can make it to the detector. This does allow for attomol detection limits<sup>59</sup> but on the other hand shows that the MALDI process is not very efficient. Elevated-pressure and atmospheric-pressure MALDI sources have been shown to stretch this limit to the sub-attomole range<sup>60</sup>. This is due to increased collisional cooling of the ions in the source region, which reduces fragmentation.

The choice of laser mainly depends on analytical preference, but does determine the choice of matrix. The matrix needs to have an absorption maximum as close to the energy of the laser as possible. In most cases, near-UV lasers are used. Either  $\text{N}_2$  lasers (337 nm) or frequency tripled Nd:YAG (355 nm) lasers are used. Although  $\text{N}_2$  lasers have the advantage of a natural intensity fluctuation, which is believed to enhance signal due to local “hotspots”, Nd:YAG lasers are becoming the default laser of choice, because of higher possible shot frequency (1 kHz) and longer lifetime, which is especially important for imaging experiments. The issue with the “hotspots” has been circumvented by Bruker Daltonics through the SmartBeam<sup>®</sup> technology, which modifies the laser spot inducing a shot-to-shot varied pattern. Laser pulse widths are in the order of 0.5 to 10 ns. Shorter-wavelength UV lasers have been tried but induce a higher degree of fragmentation and matrix-analyte reactions. IR lasers are another commonly used type of lasers in MALDI<sup>61</sup>. They deposit their energy into the surface by excitation of O-H or N-H stretch vibrations. This offers opportunities for the use of glycerol or water at low temperature as a matrix<sup>62, 63</sup>.

#### 2.2.2.2 MALDI matrix considerations

To do proper MALDI analysis, it is very important to choose the optimal matrix for the analyte. Important parameters are the matrix polarity, acidity and “temperature” under laser illumination conditions. Sufficient acidity is necessary for proper protonation of the analytes in the matrix layer. Gas-phase protonation is driven by

the gas-phase basicity of analyte and matrix<sup>65</sup>. Acids are commonly added for this purpose as well. The appearance of matrix peaks and matrix fragment peaks make some matrixes less applicable for the analysis of low-mass compounds because they cause a high background in the spectral region of interest. The matrixes that are currently most-used in MALDI of biomolecules are 2,5-dihydroxybenzoic acid (DHB), 3,5-dimethoxy-4-hydroxycinnamic acid (sinapic acid, SA),  $\alpha$ -cyano-4-hydroxycinnamic acid (HCCA). In polymer analysis many types of matrixes are used. DHB and HCCA are very popular<sup>66, 67</sup>, but dithranol is a common matrix too, especially for very apolar polymers. A general guideline for polymer analysis is that the polarity of the matrix should match the polarity of the polymer<sup>67</sup>. This was quantified using reverse-phase HPLC, in which the combination of polymer and matrix with the closest matching retention time gave the best MALDI result<sup>68</sup>. The addition of additives, can in some cases improve analyte signal significantly. Addition of salts as cationization agents is very common for polymers<sup>67</sup>. The addition of acidic compounds to the matrix solution is common in the analysis of peptides and proteins. Both methods give an increase of the quasi-molecular ion (typically  $(M+X)^+$  with  $X=H$  or a cation) signal.

Alternative matrixes have shown various advantages. To improve stability of MALDI signal new matrixes have been developed. Ionic solid and liquid matrixes were shown to give equal or superior MALDI signal in some cases, when compared to the more traditional matrixes<sup>69</sup>. Liquid matrixes would not be suited for imaging experiments because of diffusion issues. Solid ionic matrixes<sup>70</sup> have been shown successful for tissue imaging, giving better reproducibility, sample stability and overall data quality. Gold has been used to reduce sample charging and therefore spectral quality<sup>71, 72</sup>. Gold nanoparticle coating<sup>73</sup> or large gold cluster implantation<sup>74, 75</sup> were shown to function as matrix as well. The latter is also named matrix implanted LDI (MILDI). Also titanium dioxide microparticles and nanoparticles have been reported as a MALDI matrix<sup>76, 77</sup>. Several solvent-free sample preparation methodologies are reported as well, especially for insoluble analytes like some types of polymers<sup>78-82</sup>. Solvent-free methods have so far not been successful for imaging experiments, mainly do to the extensive surface contact that is involved and typically requires long mixing. Altogether, MALDI is a versatile ionization tool that can be used for virtually any class of molecules.

### 2.2.3 Other techniques

Although MALDI and SIMS are by far the most commonly used ionization techniques in imaging mass spectrometry, there are a few others as well. Also methods for post-ionisation of the large fraction of neutrals that is present near the surface in MALDI

and SIMS are used. Desorption electrospray ionization (DESI), uses electrospray ionization (ESI) generated droplets to desorb and ionize material from the surface<sup>83</sup>. A technique that uses an ESI source as well, called electrospray droplet impact ionization (EDI) uses ESI-generated charged droplets, which are accelerated to a surface and result in desorption and ionization of compounds at the surface in a manner that is to a certain extent similar to SIMS<sup>84</sup>. These techniques have shown certain advantages for small molecules, but are so far less effective for high-molecular weight compounds. Also their spatial resolution in imaging experiments is rather limited. The main advantage for DESI and EDI is the limited sample preparation that is needed.

Because neutrals encompass the major part of the desorbed material in both SIMS and MALDI, post-ionization techniques can be applied as well. SIMS with electron or laser postionization<sup>85-87</sup> was shown to give signal increase in certain cases. Atmospheric-pressure (MA)LDI has recently been reported in various variants, using a combination with an ESI source and named matrix assisted laser desorption electrospray ionization (MALDESI)<sup>88-90</sup>, electrospray-assisted LDI (ELDI)<sup>91</sup>, electrospray desorption and ionization (EDI)<sup>92, 93</sup>, matrix-assisted laser desorption electrospray ionization (MALDESI)<sup>89, 90</sup> or infrared laser ablation with electrospray ionization (LAESI)<sup>94</sup>. These ESI-assisted ionization methods have the benefit of producing multiply charged species, which is necessary for certain types of MS/MS experiments. Laser post-ionization has been reported for MALDI too<sup>95</sup> but is not widely applied.

### 2.3 Mass analysis techniques

The crucial step after ion generation is mass analysis. The quality of the mass analyzer determines largely the quality of the eventual data and therefore the quality of the analysis. Many different designs of mass analyzers are known. The mass analyzers that are used for the work in this thesis will be covered in-depth and other mass spectrometers that are commonly used for MS imaging will be mentioned. A full overview of available mass analyzers can be found in literature.

The choice of mass analyzer is dependant on many criteria<sup>96</sup>. The ones that are most important criteria for imaging MS are listed below. Most of these criteria are fairly generic and hold for regular MS as well.

- It should use a highest possible fraction of the generated ions for mass analysis. This is especially important when doing imaging, where many samples (namely each pixel) have to be analyzed at the smallest possible pixel size, offering very little analyte per pixel.

- It should fulfill vacuum requirements that come with the transmission of ions and the detector operation. Sometimes differential pumping will be necessary to go from an atmospheric pressure source to a high-vacuum analyzer. This is a rather generic requirement
- It should detect ions based on their mass/charge ratio, irrespective of their initial properties at the source, including initial kinetic energy spread. This is a rather generic requirement.
- It should detect ions with the highest possible accuracy and reproducibility. This is important for all MS application. For imaging MS the reproducibility is important to be able to make fair distribution maps of the presence of compounds at the surface.
- It should have a sufficiently large mass range, preferably with constant detection efficiency over the whole mass range. A generically important issue in MS, although often not fulfilled. Many detectors (e.g. microchannelplate-based detectors) have a lower sensitivity at higher mass. Some mass analyzers have an inherent maximum- $m/z$  limit and are therefore unsuitable for high-mass applications.
- It should be sufficiently fast. This is especially important for imaging mass spectrometers, in which typically thousands to millions of mass analyses are performed in a single imaging experiment. Acquisition time plays an important role in this kind of experiments.

Because a mass spectrometer can usually not completely fulfill all these requirements at the same time, a trade-off is usually made between these. The hybrid mass spectrometers, can circumvent some of these limitations. The combination of ion optics that can accumulate generated ions and a mass analyzer that can then detect these accumulated ions, while the next package of ions is accumulated, makes faster experiments possible.

Most mass analyzers are actually mass filters, in combination with a time- or space-differentiated detector that consecutively detects the separated ions. FTICR-MS and orbitrap MS are exceptions to this and record all ions simultaneously.

### 2.3.1 Time of flight MS

The first time of flight (TOF, but also written “ToF”) mass spectrometer was reported by Stephens in 1946<sup>97</sup>. TOF-MS is a method in which all ions that are fed into the mass spectrometer can be measured in a single experimental cycle. Mass

separation is based on the flight time difference of ions with equal energy. When ions are accelerated in an electrostatic field, they all get the kinetic energy  $E$

$$E = zU \tag{2.2}$$

in which  $U$  is the electric potential and  $z$  is the charge of the ion. Because all this electric potential energy is converted into kinetic energy and kinetic energy is related to velocity ( $v$ ) and mass ( $m$ ) as  $E=1/2mv^2$ , the velocity of the ions will be dependant on their mass ( $m$ ) and charge ( $z$ ):

$$\frac{m}{z} = \frac{2U}{v^2} \tag{2.3}$$

Because the mass spectrometer has a fixed field-free flight path with length ( $l$ ) and the electrostatic extraction field is kept constant, this leads to the time relation

$$\frac{m}{z} = \frac{2U}{l^2} t^2 \tag{2.4}$$

in which there is a quadratic relation between  $m/z$  and time ( $t$ ) with and the time-of-flight path length ( $l$ ) and electrostatic energy ( $U$ ) are constant.

At the end of the time-of-flight path, ions are detected. This is usually done using a combination of one or multiple microchannel plates (MCPs) that convert the ions into electrons through a cascade process, and a detector that detects the electrons from the MCP, which could be a faraday cup collector or a phosphor screen. The signal from the detector is then fed into an analog to digital convertor (ADC) or into a constant fraction discriminator (CFD) in combination with a time to digital convertor (TDC). ADC's are most useful when multiple ions strike the detector within a short time frame (<10 ns, depending on the recovery speed of the detector and the electronics) and therefore normally used for MALDI-TOF experiments. The CFD/TDC combination records single ion hits. Recording single ion hits has the advantage that data is only recorded when there is actually an event. TDC acquired data is therefore also called "event-based data". TOF-SIMS experiments are often recorded using a TDC acquisition system because of the small number of secondary ions that are generated by each primary ion pulse. All peak information of the hits is lost and only the time at which an ion hits the detector is recorded. This implies that multiple ions hitting the detector at the same time within dead-time of the detection system are counted as a single event.

Because the time of flight of all ions is measured, it is important that all ions have the same departure time at the beginning of the flight path. To fulfill this requirement, the ions in the beginning of the analyzer need to be pulsed. For MALDI, and in most cases SIMS, ion generation, this is quite straightforward because of the pulsed nature of these ionization sources. For continuous sources, like electrospray ionization (ESI), the continuous stream of ions from the source needs to be split into small packages, preferably with no loss of ions. This can be done by first trapping the ions and then pulsing them out of the trap into the analyzer, by bunching the ions together or by sending “long” packages of ions into an orthogonal TOF tube. Orthogonal TOF systems usually use ion “cooling” and focusing to decrease kinetic energy variation and improve time focus. Linear bunching can be used to compress continuously generated ions into a short time focus<sup>6</sup>.

Apart from a sufficiently short duration of the ion pulses, energy distribution of the ions is important for the quality of the obtained mass spectrum. For pulsed experiments, like in the case of MALDI-TOF MS, ions are generated that have different kinetic energies. One way to compensate for this is through delayed extraction, also called “time lag focusing”. With this method, the initial kinetic energy is compensated for by allowing the generated ions to move through a field-free area before the extraction field is applied. In this way, ions with a high energy in the direction normal to the sample plate experience a smaller extraction field and therefore the energy spread between ions with different initial kinetic energies is reduced.

The use of ion mirrors, which are used in reflectron TOF systems, can compensate for kinetic energy differences too. Electrostatic ion mirrors reflect the incident ions in such a way, that the high-energy ions follow a longer path in the mirror than the low-energy ions. In this way, the path of high-energy ions becomes longer in the mass spectrometer. Most commonly, this is done once, resulting in a “V” type of reflectron TOF analyzer but for more compact mass spectrometer designs or longer flight paths, “W”-type analyzers are used as well.

The same principle of adjusting the path length based on the ion energy is used in electrostatic sector instruments. This is for instance done in the triple focusing time of flight (TRIFT) system, which was intensively used for the work in this dissertation. Multi-turn TOF systems use the same principle, and feature a flexibly elongated flight path in addition to this<sup>98</sup>.

The great advantages of TOF mass analyzers is their practically infinite mass range and the high acquisition speed. There is no fundamental high-mass limit for TOF analyzers because the high-mass limit of the analysis merely depends on the time that is allowed for ions to travel through the TOF tube. Because of high mass range, TOF

analyzers are very suitable for high-mass applications in, e.g. polymer or protein analysis. The high acquisition speed makes them ideal for imaging MS applications.

### 2.3.2 FTICR-MS

Fourier transform ion cyclotron resonance mass spectrometry (FTICR-MS, or just: FT-MS) is a mass analysis technique that simultaneously measures all ion  $m/z$  values that are in the mass analyzer<sup>99, 100</sup>. FTICR-MS is not very commonly used for imaging experiments but gaining increased interest. The long acquisition time per spectrum and the high operation cost that comes with the use of superconducting magnets are the major setbacks for this type of analysis. Because of its advantages, especially in mass resolution, it has however proven its value in the MS imaging field. High mass resolution experiments showed that a single peak in a TOF analyzer can be resolved into multiple different peaks in FTICR-MS, each having distinctly different spatial distributions<sup>101, 102</sup>. The introduction of the Orbitrap mass analyzer, has added a new dimension to Fourier transform mass spectrometry. The lower operation cost of this type of mass spectrometer, still giving high mass resolution (albeit not as high as FTICR-MS), makes it a hot prospect for the future of imaging MS.

In a FTICR-MS, ions are trapped in a magnetic field with electrostatic trapping plates on both ends. Around the cylindrical trapping region, there are four plates (typically equally distributed over  $90^\circ$  each), two of which bear the excitation signal perpendicular to the magnetic field and two of which record the induced space image charge. The excitation signal excites the ions off the axis of the magnetic field, which makes them resonate in an orbit around the cell axis. This movement is recorded on the detection plates. The resonance frequency of the ions depends on the  $m/z$  ratio and the magnetic field ( $B$ ), by good approximation through the relation

$$\omega = \frac{zB}{m} \quad 2.5$$

Because the excitation signal consists of a broad-band AC field, all ions in the cell are excited during their presence in the cell. The detection plates however only record the resonance frequencies of the ions in the cell. By Fourier transformation of this frequency spectrum, an  $m/z$  spectrum can be obtained. The resolution of the mass spectra is dependant on the number of oscillations by the ions in the cell and therefore depends on the length of the analysis.

The main advantages of FTMS are unsurpassed mass resolution and mass accuracy, which can be benefited from when doing analysis based on accurate mass, or the



analysis of complex mixtures. In addition, the range of  $MS^n$  possibilities is much larger for FTICR-MS than for any other MS technique.

## 2.4 *Imaging mass spectrometry*

In imaging mass spectrometry, images are created based on mass spectral information. A sample surface is exposed to an ionization source that generates ions from the surface material. The generated ions are then detected in a mass analyzer. The resulting dataset contains a full mass spectrum for each image pixel. A mass spectrum could contain intensity values for thousands of  $m/z$  values. When a peak of interest is observed by the analyst, an intensity plot can be made that visualizes the distribution of the related compound at the sample surface. When this is done for multiple  $m/z$  values of interest, each  $m/z$  value can be assigned a color, giving a pseudo-color plot that visualizes the distribution of several compounds throughout the sample. The acquisition of a full mass spectrum at multiple image pixels results in a datacube, a collection of intensities for each x-position, y-position and  $m/z$  value. The way data is actually stored varies per acquisition type. The choice of data storage during or after acquisition depends on the way data is acquired.

Two modes of imaging MS can be distinguished: microprobe mode MS imaging and microscope mode MS imaging, as explained in the next two sub-sections.

### 2.4.1 **Microprobe mode MS imaging**

Microprobe mode MS imaging is the most commonly used MS imaging method. The sample is analyzed by rastering the ionization source (usually an ion beam or laser beam) over the sample. At each position, a mass spectrum is recorded (figure 2.5 left). Rastering of the ionization beam over the sample surface is done by either rastering the beam itself and keeping the sample in a steady position or by moving the sample and keeping the beam in place. The rastering method is faster but offers a limited field of view on the sample. A combination of beam and stage rastering is an obvious other possibility and is used to image large areas using with a beam-rastering instrument. Rasterizing the ionization beam is most common in SIMS, often combined with stage rastering. MALDI is normally done by moving around the sample. The resulting image dataset has a maximum image resolution that depends on the diameter of the ionization beam at the surface and the step-size or accuracy of the ionization beam and/or the sample movement. In MALDI microprobe imaging, resolution higher than the laser spot size at the surface has been achieved using an over-sampling approach<sup>103</sup>.

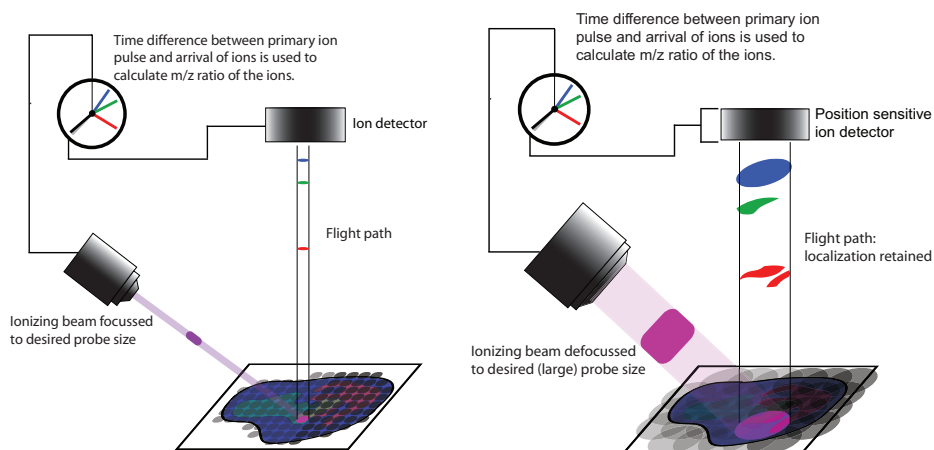


**Figure 2.5 left:** schematic representation of a microprobe mode imaging mass spectrometer; **right:** schematic of a microscope mode mass spectrometer.

## 2.4.2 Microscope mode MS imaging

Microscope mode imaging is a less mainstream MS imaging technique. The key difference with microprobe imaging is that the dataset is not collected by acquiring a range of mass spectra, but by recording a direct image off the sample surface (figure 2.5 right). Rather than scanning the sample, the sample and ionization beam are kept still and the generated ions are detected in a position sensitive manner. The spatial distribution of the ions that are generated within the exposed area is retained throughout the mass spectrometer and projected onto a position sensitive detector. Microscope mode imaging has so far been limited to recording either total ion images, or selected ion image of one single mass. This thesis will show ways to both resolve localization and  $m/z$  for each of the ions (chapter 5). The sample size that can be measured using microscope imaging is not limited by the diameter of the laser spot, because a combination of a microscope and microprobe can be used: the sample is rastered and a microscope image is recorded at each position. These individual microscope images can then be composed into one large microscope image, giving a high-resolution image of a large area (figure 2.5, figure 2.6; further described in chapter 4).

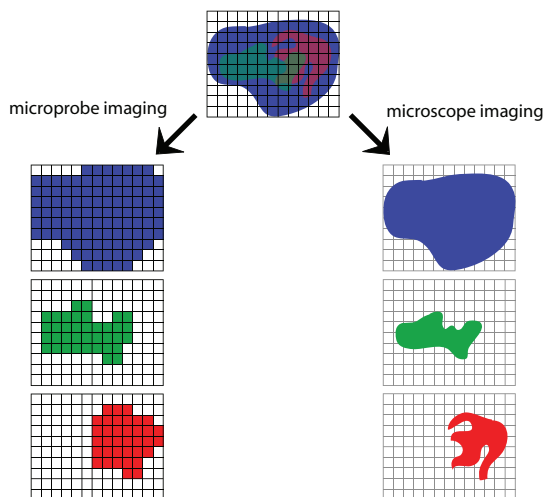


**Figure 2.6** Comparison of the results of a microprobe (left) and a microscope (right) mode imaging mass spectrometry experiment. The raster in the microscope images is shown as a guide to the eye for means of comparison and has nothing to do with the actual measurement in which a larger distance is used between the different laser shot positions.

## 2.5 MS imaging instrumentation used for this work

Several imaging instruments that were used for this work are described below. The main focus is on the triple focusing time of flight (TRIFT) systems because this has been used most extensively. Other instruments are briefly described and finally, a comparison is made in section 2.9 on what the performance is of choice of instrumentation on the quality of the eventual spectra and the information that can be obtained from them, using a polymer standard sample.

### 2.5.1 TRIFT imaging systems for TOF-SIMS and MALDI-TOF

An instrument that is capable of doing both microscope and microprobe mode imaging MS is the triple focusing time of flight II (TRIFT-II) system, built by Physical Electronics (Eden Prairie, MN, USA). This commercial instrument is a TOF-SIMS instrument with ion optics suited for stigmatic ion microscopy. On a regular basis, this instrument is however operated in microprobe mode. Throughout this project, two of these instruments have been used. One of the instruments is routinely used for SIMS imaging in the microprobe mode. The other instrument is highly customized to do microscope mode MALDI and SIMS imaging. Initial developments to make MALDI MS imaging possible on this instrument were done by Luxembourg<sup>104</sup>. Further customizations encompass a major part of this thesis and are described in chapters 4 and 5.

The TRIFT<sup>105, 106</sup> consists of a flight path that is bent through three electrostatic sectors that each encompass one-fourth of a circle (figure 2.7). Detection is therefore done orthogonal to the surface at an angle of  $270^\circ$ . The dimensions and electrostatic potentials are chosen in such a way that the elongation of the path length of ions with a higher energy is exactly large enough to compensate for their higher velocity. Accordingly, the flight path of lower-energy ions is compensated for by their shorter path length. Also, the angular distribution of the emission angle of ions at the surface is compensated for. A contrast diaphragm can be put in place to constrict the angle of emission that is tolerated, which improves spatial resolving power at the cost of lower sensitivity. Moreover, metastable ions are rejected from the TOF path because of the curved design. Therefore only surface-generated ions are detected, resulting in low background noise. Energy filtering can be done to set a certain kinetic energy window of the secondary ions that is let through to the detector.

### 2.5.1.1 TOF-SIMS imaging

Most of the TOF-SIMS imaging done for this thesis was done using a TRIFT system. Some of the results shown in this thesis were done elsewhere and are indicated as such. The TRIFT system is equipped with a liquid metal ion gun (LMIG), which is most commonly used as a primary ion source. Part of the work presented in this dissertation was done with an  $\text{In}^+$  primary ion source. This ion source was upgraded to a gold-germanium source and therefore the most recent experiments were done using Au primary ions. An Au-Ge LMIS mainly gives  $\text{Au}^+$  primary ions but also  $\text{Au}_2^+$  and  $\text{Au}_3^+$  cluster ions. Also Ge-related ions are formed, including  $\text{Ge}^+$ ,  $\text{Ge}_2^+$ ,  $\text{AuGe}^+$ ,  $\text{Au}_2\text{Ge}^+$  and  $\text{Au}_3\text{Ge}^+$ , but these are normally not used for analysis. Cluster filtering is done using a quadrupole blanker. The primary ion energy of LMIS generated ions can be adjusted to preference, but in the work presented here it is typically 15 keV for  $\text{In}^+$  ions and 22 keV for  $\text{Au}^+$  ions. The angle of incidence of LMIS generated ions is  $35^\circ$  with respect to the sample normal.

The TRIFT system is also equipped with a  $\text{Cs}^+$  primary ion source, which is mainly intended as a sputtering gun for depth profiling. It can however also be used as a pulsed primary ion source, but only in the microscope mode because of its limited focusing capabilities. The  $\text{Cs}^+$  source has an angle of  $42^\circ$  with respect to the sample normal.

### 2.5.1.2 MALDI-TOF imaging

MALDI or LDI-TOF imaging is done on the customized TRIFT instrument. The flange on which the LMIG is normally connected to the analysis chamber is

customized to fit an optical fiber. Most of the details on the instrument are given by Luxembourg<sup>107</sup>. A general description is given here and more details are given in the respective chapters of this thesis.

The third harmonic of a Nd:YAG laser (355 nm) is used for UV-MALDI. Other wavelengths are filtered out using mirrors with wavelength-selective reflection. The laser light is focused and collimated into an optical fiber. This fiber is used to transfer the light from the optical table to the TRIFT. A telescope setup for adjusting the laser spot size is mounted in front of the TRIFT entrance window. A focusing aperture is present in the vacuum for fine adjustments of the laser spot focus.

### 2.5.2 Other (imaging) MS instrumentation

Apart from the setups described above, other imaging and non-imaging MS equipment was used during this project. Most of these setups were not extensively used for this work, therefore a only a brief description suffices.

MALDI-TOF mass spectrometry was done using a Bruker Ultraflex 3 (Bruker Daltonik GmbH, Bremen, Germany). Large, automated imaging experiments can be done routinely in the microprobe imaging mode. A special LIFT technology enables conversion of the TOF instrument into a TOF/TOF instrument for MS<sup>2</sup> experiments. A Waters Synapt HDMS (Waters Corporation, Manchester, UK) is used as a MALDI imaging instrument, but can be readily converted into an API instrument for, e.g. ESI experiments. It combines ion mobility spectrometry (IMS) separation through a Triwave<sup>TM</sup> cell with an orthogonal TOF setup. This enables both IMS separation followed by a TOF measurement and MS/MS experiments.

An almost completely in-house built 7 T Fourier transform ion cyclotron resonance mass spectrometer (FTICR-MS) is equipped with a MALDI source which is readily changed into an ESI source. FTICR-MS offers the possibility of MALDI imaging MS at high accurate mass and high mass resolution. It can also be used for MS<sub>n</sub> experiments using several types of dissociation techniques. MALDI-FTICR-MS thus offers opportunities for measurements that cannot be done otherwise. The disadvantage of FTICR-MS is the long acquisition time that is inherent to an FTICR experiment. Therefore, spatial resolution needs to be compromised when analyzing large samples.

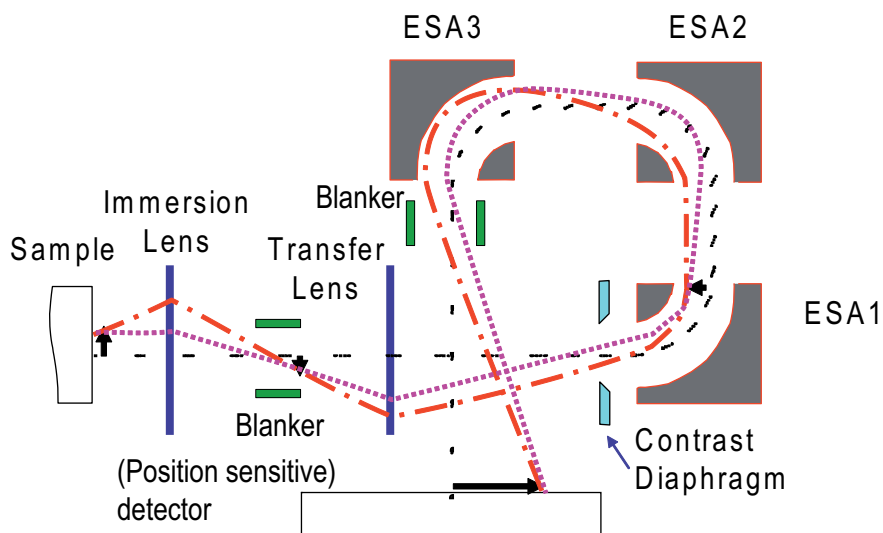


**Figure 2.7** Schematic representation of the ion optics of a TRIFT system (figure adjusted from Physical Electronics documentation). The image shows both compensation for lateral and longitudinal momentum spread. The black dots at the center of the flight path show kinetic energy compensation. The pink (dotted) line and the red (dot-dashed) line show compensation for ions leaving the surface with a normal and off-normal emission angle respectively. The black arrows show points in which ions have their original lateral distribution. The two lenses determine the final magnification factor. A contrast diaphragm can be put in place to filter out a certain range of emission angle. Electrostatic blankers can be used to block certain parts of the TOF spectrum.

## 2.6 Sample preparation techniques

The proper treatment of samples before the imaging MS experiment is crucial for its success. It depends on the used analytical technique, which sample-handling step is most important, but generally spoken, each sample handling step can introduce contamination, a bias in the results or even complete loss of eventual data. Sample treatment and preparation pathways are different for MALDI and SIMS. Taking a biological tissue sample as an example, its explantation is the first step. After this, it is typically frozen and sometimes embedded, after which cryo-sectioning takes place. Subsequently, the section can optionally be washed, in which the solvent determines which molecules are washed away. Thereafter, sample coating can be done with a variety of matrixes or metals.

## 2.6.1 Sample handling and treatment

Insights in sample handling and treatment show more and more clearly that the sample treatment before matrix deposition or before the measurement has a large influence on the final result.

As a first step of sample preparation one has to make sure the sample is flat. This is especially critical when doing TOF analysis, in which sample roughness can ruin mass resolution because of differences in path length between ions with a high and a low origin <sup>108</sup> and it can cause inhomogeneous sensitivity due to primary beam shadowing effects in SIMS. Sample flatness can be achieved using a cutting technique, like a (cryo-)microtome. During cryo-sectioning, the proper temperature is important and depends on the nature of the sample. Different tissue types require different cutting temperatures and the combination of different types of tissue or the combination of tissue and a non-biological specimen like a polymer implant makes the proper temperature choice even more important because of differences in elasticity at set temperature. Other techniques include polishing techniques, which show disadvantages of a high risk of smearing (in case of polishing paper) or molecular damage (in case of ion-milling).

When samples have high water content, like it is usually the case for biological samples, proper drying procedures are important. Too quick drying can lead to tissue rupturing, insufficient drying before bringing tissue into vacuum can also make tissue sections rupture.

During sample preparation, cleanliness of all materials that are used is crucial. Because detection limits can be very low and ion suppression effects can be strong, contamination of samples should be avoided at all time. Human skin-related lipids can influence lipid patterns seen in the samples. Siloxanes, e.g. poly(dimethyl siloxane) (PDMS) are a known contaminant that SIMS is very sensitive to due to its high surface mobility which makes it spread out evenly over the surface, which is detrimental for SIMS given its surface sensitive nature. PDMS is a common mold release agent for plastics but also present in many personal care products including hair-gels, and hair-conditioners, skin cream etc. and therefore abundant pretty much everywhere. Sample handling compounds should be chosen with care. Optimum cutting temperature (O.C.T.) media (like TissueTek<sup>®</sup>, Sakura Finetek Europe B.V., Zoeterwoude, the Netherlands) tend to contain components that are smeared out over the surface, thus masking the analytes of interest or at least suppressing their signal intensity.

Washing is another important step for peptide and protein analysis from biological tissue sections. The choice of washing solvent mixture determines to which extent

salts, lipids and hemoglobin are removed. Removal of high-abundant compounds like salts and lipids improves signal quality and strength for several reasons. Salts are known to have a bad effect on analyte incorporation and matrix crystallization and are known to segregate from the matrix, which leads to an inhomogeneous matrix distribution and consequently inhomogeneity in the signal intensity, giving for instance both  $[M+H]^+$  and  $[M+Na]^+$  depending on the position in the matrix crystal<sup>45</sup>. Washing was shown to be an effective way of removing salts with aqueous ethanol solutions<sup>43</sup>. Recent developments tend towards more rigorous washing procedures to also remove lipids and thus enhance the peptide and protein signal. The choice of solvent then determines which components are washed away. Commonly used solvents for this purpose are hexane, acetone, toluene, xylene and chloroform<sup>109, 110</sup>, either purely or in solvent mixture or combination. Several washing steps can be performed to get optimized removal of the compounds of choice. A major disadvantage of washing is the spreading of analytes over the surface. Localization of compounds is only inherited to a certain extent. This is not a big issue when doing lower resolution techniques like microprobe MALDI which typically has a resolution of  $>100\ \mu\text{m}$ . However, when doing SIMS, me-SIMS or high-resolution MALDI, analyte diffusion becomes a major issue. Moreover, SIMS or me-SIMS are mainly sensitive to low-molecular weight compounds, exactly these are the compounds that diffuse the most.

### 2.6.2 Matrix deposition

Matrix deposition is a crucial part of sample preparation for both MALDI and MESIMS experiments. The quality of the matrix coating process determines the quality of analyte extraction from the surface, and therefore the signal quality. The matrix coating process has to meet several requirements:

- retain localization of molecules at the sample
- extract molecules from the sample to an extent that results in the most optimal analyte/matrix ratio
- form crystals that give good MALDI/MESIMS signal
- form crystals small enough to match the resolution requirements of the used analytical technique

The first two requirements have to do with the wetting process of the sample. The sample should not get too wet (would result in diffusion), yet get wet enough (otherwise extraction will not take place). Also, the matrix crystals should be small enough. These crystals are composed of the matrix and an extract from the underlying surface. Because the material in the crystal is, within the constraints of



the extraction process, representative for the underlying region, the size of these crystals limits the spatial resolving power. This is usually not an issue when microprobe mode MALDI is done with a laser spot size much larger than the crystals. Given the very small probe size typical SIMS, crystal size is limiting the spatial resolving power for ME-SIMS. When performing ME-SIMS or MALDI ion microscopy, the crystals are typically larger than the resolving power of the ion optics and therefore limit the spatial detail that can be resolved. The produced crystal size depends on the type of matrix used, the type of solvent that is used, the amount of wetting of the surface during the coating process and the surface morphology. The choice of deposition method depends on analytical preference, availability and solvent compatibility of spotting instrumentation.

With the evolution of imaging mass spectrometry, researchers and companies have developed instrumentation to reproducibly cover surfaces with matrix. An extensive description and overview of these techniques and specific instruments is given in literature <sup>3, 111</sup>. Generally spoken, matrix deposition techniques can be divided in three categories: solution spraying techniques, dry deposition techniques and localized droplet deposition techniques.

Spraying techniques deposit a spray of small solution droplets onto the sample surface. This nebulization can be done using a pressure-driven device (manual or robotic <sup>112</sup>), an electrospray source <sup>113</sup> or a vibrating membrane. Generally spoken, nebulization can give small droplets and therefore small (down to 10  $\mu\text{m}$ ) matrix crystals, homogeneous matrix deposition and good control over the wetting of the surface. It can be time-consuming, but good automation methods are available.

Dry deposition techniques include electrospray nebulization <sup>113</sup> (at a large distance to let the solvent evaporate completely before the nebula reaches the surface) and the completely solvent-free deposition of dry crystals using a brush and a sieve <sup>114</sup>. Another solvent-free deposition technique is matrix sublimation <sup>115</sup>. Solvent-free and dry deposition methods give a very homogeneous layer of matrix with the smallest ultimate crystal size, but at the cost of sensitivity for certain compounds. There is no dissolution of analytes from the surface, so the signal that is measured mainly originates from surface material that is adsorbed onto or incorporated in the matrix crystals.

Solution droplets can be deposited manually, using a pipette, or with the help of an automatic spotting device. Manual spotting results in poor spatial resolution and is therefore only suitable in situations where image resolution is not of interest. Automatic spotting devices offer the possibility to deposit arrays of microdroplets with about 150  $\mu\text{m}$  inter-spot distances, using a piezoelectric inkjet method or acoustic droplet ejection. At the cost of image resolution, these methods offer the

guarantee that there is no diffusion between droplets during matrix deposition. Because these droplets have a size of about 150  $\mu\text{m}$ , which is wetted completely during the deposition process, segregation of salts takes place concentrating these in the droplet rim. The decrease of salt concentration is known to improve the eventual MALDI signal in biological tissue samples because of improved matrix crystallization and a decrease of ion suppression effects. Robotic spotters have the advantage of low solution consumption and are therefore ideal for the deposition of expensive compounds like some proteolytic enzymes.

For this project, several of the above mentioned techniques were used. Nebulization was done by hand, using a thin layer chromatography (TLC) sprayer, or automated, using a robotic pneumatic sprayer that was built in-house according to a design developed by Stoeckli et al. at Novartis<sup>112</sup> or with a Bruker ImagePrep (Bruker Daltonics) vibrational coater. Both the pneumatic spraying robot and the ImagePrep offer control over the sample environment to prevent too fast drying, which is detrimental for the analyte extraction. An electrospray deposition system is available for small-crystal and very homogeneous matrix coatings. Droplet deposition is done with a Shimadzu CHIP-1000 (Shimadzu Biotech), chemical inkjet printer, which is a piezoelectric-driven spotting device. The CHIP offers limited environmental control and an in-house built temperature-controllable sample plate.

### 2.6.3 Sample metallization

Sample metallization has proven to be beneficial in some experiments for both SIMS<sup>44, 71, 116-123</sup> and MALDI<sup>71</sup>. For metal-assisted SIMS (metA-SIMS), the enhancement is most obvious: higher (quasi-) molecular ion signal and better image quality. Although most organic compounds give an enhanced signal after sample metallization, some are suppressed. Phosphocholine signal from tissue is known to decrease upon gold coating (see figure 2.8). Silicones like poly(dimethyl siloxane) (PDMS), which are notorious contaminants in SIMS due to their surface-mobile property are also suppressed in some cases.

Most commonly used metals for sample metallization are silver and gold, with gold giving the highest enhancement<sup>116</sup>. Metal deposition is done by sputter coating. Typical layer thicknesses are in the 0.5-10 nm range for Au, depending on the analysis technique used. A typical value for SIMS is 1 nm, for MALDI 5 to 10 nm is common. A nm-thick layer is known to not cover the surface completely, but rather form small islands on the surface<sup>119, 123</sup>. This is due to the high surface energy of Au, which makes island formation more favorable than the formation of a closed layer. Not surprising with an atomic radius in the order of 1.4 Å, which results in only a 7-atomic layers thick layer when a 1 nm coverage would be complete.

Although improvement of signal is obvious, especially for SIMS, the exact mechanism behind the enhancement is not fully understood. Several mechanisms are proposed to account for the gain in signal, many of which are speculative.

Charge compensation is a major aspect of signal enhancement. Both image quality and intensity of the signal are enhanced. This holds for both SIMS<sup>124</sup> and MALDI<sup>125</sup>. A thin metal layer on top of an insulator facilitates charge-evacuation due to its conductivity and connection with the sample holder.

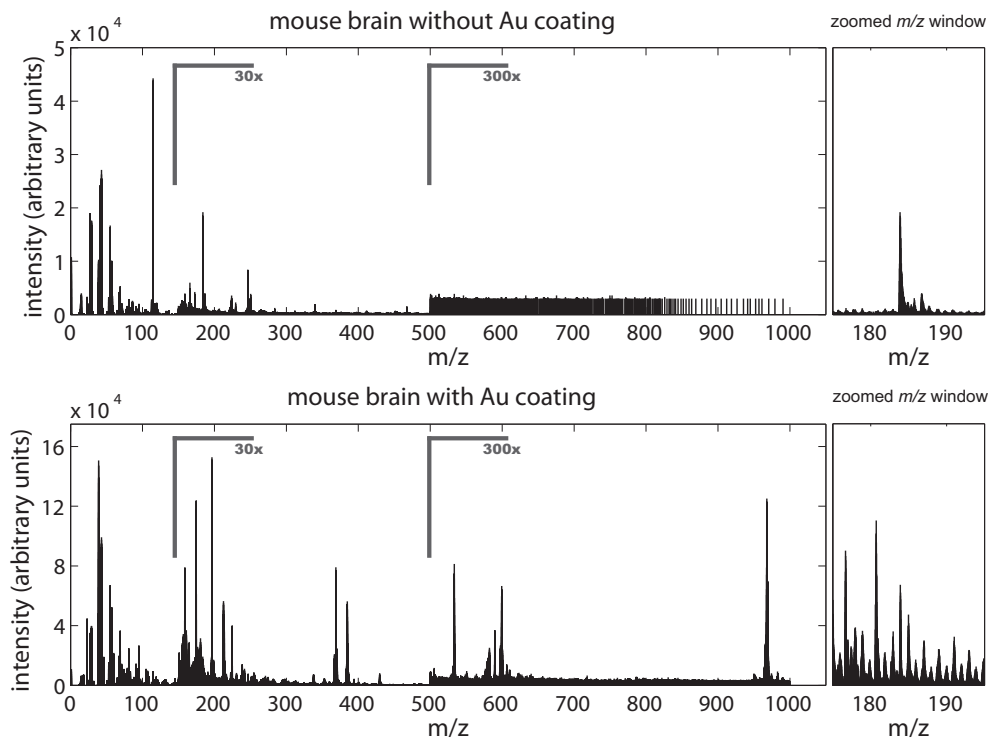


**Figure 2.8** A comparison between the total image spectrum of a mouse brain section (top) and a gold coated mouse brain section. The total intensity increase as well as the appearance of new peaks at high mass (e.g. the gold bound cholesterol dimer:  $[2M+Au]^+$  at  $m/z=970$ ) are obvious for the Au coated specimen. The phosphocholine headgroup ( $m/z=184$ ) is clearly visible in the uncoated sample but disappears in the background for the coated sample. Although the absolute intensity is the same (640 arbitrary units) for both samples, the relative intensity with respect to other major peaks changes dramatically and the peak at  $m/z=184$  is only seen when zooming in (right part of the image). This indicates that care should be taken about the introduction of biases in the mass spectrum when gold coating is applied.

Cationization enhancement <sup>116</sup> as well as chemical ionization enhancement, but also suppression could play a role in certain cases. The metal can donate a metal cation to the analyte and form analyte-cation complexes, that are readily measured in the mass spectrometer. Delayed ion formation is expected as well, based on the number of ions with a kinetic energy deficit that are detected.

An ionization potential decreasing effect is assumed to be caused by the proximity of a metal to the organic analytes. When an analyte is in the proximity of a metal, its orbitals interact with the filled or empty conduction band of the metal. This can have both an ionization potential increasing and an ionization potential decreasing effect. This effect would be the strongest when diffusion of organics onto the metal takes place, but could also take place at the interface between metal and organic substrate. The orbital interaction with the metal induces a raise in the energy of the highest occupied molecular orbital (HOMO) of the analyte and when the Fermi level of the metal is high enough, the lowest unoccupied molecular orbital (LUMO) could be populated by electrons from the metal, resulting in a decreased ionization potential. This is a mechanism that has been a proposed explanation for more efficient ionization at a metal-matrix interface for the photoionization process in MALDI <sup>126</sup>. It is therefore likely to be an explanation for signal enhancement by metallization of MALDI samples as well.

The stopping-power effect is assumed to contribute to the ionization of mobile surface components in SIMS. The analytes diffuse onto the metal islands and create a situation as if the sample was deposited in a monolayer onto a metal substrate, which is known to be an efficient way of analyzing certain compounds. The stopping power of the underlying metal causes the primary ion to deposit its energy much closer to the surface than in a completely organic sample. As a result, less fragmentation and less reactive rearrangement of ions occurs and more (quasi-)molecular signal observed. The fact that the total ion count enhancement effect of metallization is not significant when using C<sub>60</sub> primary ions <sup>119</sup> pleads for this theory. C<sub>60</sub> has a higher stopping power in organic compounds by its nature and therefore benefits much less from this effect than mono-atomic primary ions like Ga<sup>+</sup>, In<sup>+</sup> and Au<sup>+</sup>, which was also shown for molecular overlayers on metallic substrates <sup>16</sup>. The decrease in signal for the highly surface-mobile silicone is however in contradiction with this theory.

For this project, sample metallization was used for both SIMS and MALDI. Au was used for metallization and applied using a Quorum Technologies SC7640 sputter coater equipped with a FT7607 quartz crystal microbalance stage and a FT7690 film thickness monitor.

## 2.7 Complementary techniques

Although imaging mass spectrometry is very powerful at resolving both molecular and spatial information, the use of complementary techniques can add tremendous benefit in sample analysis. The complementary information that can be obtained offers more insight in the investigated sample.

### 2.7.1 Optical microscopy

Optical microscopy is the complementary imaging technique that is by far used the most in imaging mass spectrometry. During sample collection, the integrity and state of the sample is checked. During sample preparation, microscopy is used to again assess the integrity of the sample, as well as to determine matrix coverage in the case of matrix coated samples.

When an overlay of a MS image with an optical sample image is made, quite often optical microscopy is replaced by optical scanning equipment, but at high image resolution (<5  $\mu\text{m}$ ), a good microscope is still inevitable.

For the work presented in this thesis, a Leica DM-RX microscope equipped with a Nikon DMX 1200 CCD camera for high-resolution microscopy (100x-1000x magnification) and a Nikon Super Coolscan 5000 ED slide scanner for fast scanning of sample slides at 5  $\mu\text{m}$  resolution were used. In addition to this a small microscope (CETI, Belgium) was used for quick checking of samples, especially during sample preparation.

### 2.7.2 FTIR imaging

Just like regular Fourier transform infrared (FTIR) spectroscopy, FTIR imaging is capable of determining functional chemical groups. The analysis is based on the specific vibrational resonance that each molecular bond has. FTIR imaging is commonly applied in the analysis of polymers and polymer mixtures<sup>127, 128</sup>, art research<sup>129, 130</sup> as well as in biomedical studies<sup>131</sup>. RAMAN microspectroscopy<sup>132, 133</sup>, another member of the family of vibrational spectroscopy techniques, is also used as a complementary technique to imaging MS. Part of this work was complemented using a Bio-Rad FTS-6000 FTIR spectrometer extended with a Bio-Rad UMA-500 IR Microscope (nowadays Digilab, Cambridge, MA, USA).

### 2.7.3 Regular MS techniques

When looking for localization of chemically or biologically relevant compounds, identification is a key requirement for proper MS analysis as well. Identification cannot always be achieved by experiments from the sample surface. The small number of generated ions, especially in high-resolution experiments is often

insufficient for proper MS<sub>n</sub> analysis. Moreover, not all techniques allow MS/MS analysis. For instance commercial TOF-SIMS instruments are currently not capable of MS/MS. Also the presence of multiple compounds that, at the resolving power of the imaging mass spectrometer, have the same mass, is an obstacle in the proper identification of molecules. Especially for large molecules, accurate mass measurements have insufficient accuracy for determining even the elemental composition. Moreover, to determine the chemical structure, fragmentation of the analyte is necessary. Therefore, regular MS techniques, including sample preparation, extraction, purification, concentration and separation steps with HPLC are an important complement to imaging MS techniques for the successful analysis of many samples in imaging MS.

## 2.8 *Data analysis*

The amount of data generated in imaging mass spectrometry can be tremendous. A typical MS imaging dataset contains thousands of spectral channels and thousands of positions. Simple calculus tells for instance that a 128x128 image with a mass range up to 1000 Da contains over 16 million values at unit mass resolution. When mass and/or spectral resolution are increased even further, datasets get too large to deal with using regular desktop computers. To convert this enormous amount of data into information is not trivial and in many cases, specialized techniques are indispensable. Manual browsing of data gets increasingly complicated and therefore time-consuming. Therefore, data analysis methods tailored to the imaging MS type of datasets are becoming increasingly more important in imaging mass spectrometry. Software and algorithm development therefore forms an essential part of the MS imaging field.

Also data format standardization is currently a hot topic in imaging MS. Recently the i-mzML standard was introduced. This is a standard format highly based on the HUPO (Human Proteome Organization) MS data standard mzML but tailored to the type of, often large, datasets produced in an MS imaging experiment. Data standardization offers the opportunity for the user to use his analytical tool of choice independent of the way a dataset is acquired. This promotes exchange of software tools between MS imaging laboratories and offers the possibility to use the same data analysis tools for data acquired on different instruments from different suppliers.

Several methods are available to make the mass spectrometrists' life easier. A brief overview follows in the subsections below. A more in-depth approach to some of the techniques is given in chapter 6 of this dissertation.

### 2.8.1 Data pre-treatment

After acquisition of a MS imaging dataset, some clean-up of the dataset can be necessary. MALDI spectra are known to show strong background signals. Because an image is a comparison of spectral intensities, this background needs to be subtracted to avoid intensity variations due to background level variation. Besides background subtraction, also total ion image normalization can be applied. Normalizations should however be always be accompanied with a critical eye, because they can introduce unfair biases in some cases. Spectral normalization is sometimes applied as well, but has the drawback of ignoring the fact that ionization efficiencies are not the same for all compounds. Normalization on an internal standard would therefore be a better choice, but still largely neglects matrix effects.

Having well-calibrated spectra throughout the whole MS image, is very important. A mismatch in calibration, e.g. due to height differences in a TOF experiment, can create artifacts giving different distributions for the same sample, but each having a slight calibration mismatch. This becomes more important when high resolution mass spectra are used to produce distribution images.

Data reduction is another important step in data analysis. Data reduction is often necessary in order to be able to load a full imaging MS dataset into the memory of a standard desktop personal computer. Also when statistical analysis is done, the limited memory forces data reduction. Data reduction can be done by ‘binning’ spectra or images, which means that a set number of neighboring spectral or image points are summed, thus reducing spectral or spatial resolution. In addition to data reduction, binning is an excellent denoising method, enhancing contrast in both spectra and images<sup>134, 135</sup>.

Peak picking is another data reduction method that is commonly applied in the spectral dimension. Unlike binning, which decreases resolution and thus leads to a loss of information, peak picking retains the full-resolution information of each detected compound. In addition to reducing the data size, peak picking allows identification of the detected compounds by comparison with computed elemental composition or database comparison. The disadvantage of peak-picking performed on the total image spectrum, as it is most commonly done, is the risk of overlooking compounds that are only present in a small part of the sample and therefore give a very low peak in the total image spectrum.

### 2.8.2 Manual data exploration

The most basic and in many cases still the most insightful way of exploring MS imaging data is manual. Peaks of interest can be selected in the total image spectrum

and an intensity profile image or selected ion current (SIC) image of that peak can be made. Overlays of several SIC images give the distribution of the corresponding compounds at one single glance. Alternatively, a spectrum can be based on the addition of all spectra in a region of interest (ROI) of the image. This is often done to assess the spectral identity of a distinct region in the image.

Manual processing methods come with all commercial imaging mass spectrometers. It can nevertheless be interesting to look at data from a different perspective. Most packages look at data from a spectral point of view. This has the major disadvantage that trace compounds are often overseen or, due to noise, not seen at all in the summed spectrum, but nevertheless show a distinct distribution. The development of the DataCubeExplorer at AMOLF largely circumvents this. It loads data into memory from an imaging point of view rather than from a spectral point of view. This enables fast browsing through the image plains of all spectral values. It turns out to be an excellent and fast way of exploring data for small image features that would otherwise be overseen.

When only one or a few compounds are of interest, manual data analysis is by far the fastest to just visualize a SIC image of those compounds, which could already be done during analysis. For more complex samples, in which automated exploration methods are used for data exploration, manual data analysis is often used as a complementary method and for validation purposes.

### **2.8.3 Automated data exploration**

One of the great things of MS imaging is the fact that it is a non-specific technique. This means that it can be used for exploring molecular distributions without any prior knowledge of the sample. As an example, distributions of proteins can be visualized without having a targeting label, which is common practice in immunohistochemistry. To fully exploit this advantage, an understanding and visualization of correlations between spectral and spatial features is necessary. This can be done using statistical analysis tools. For instance one could like to find out which chemical components (represented by peaks in the mass spectra) are correlated. The most obvious example of correlated peaks would be for different fragments from the same molecule, but also compounds that are correlated otherwise, e.g. for biological reasons, or molecular mass distributions of polymers, will be grouped into one class. The number of resulting classes is typically orders of magnitude lower than the number of peaks in the spectrum, allowing for a much more concise representation of the dataset without disregarding any of the data. Many literature articles about this subject are available, many of them focusing on MS imaging.



By far the most common and most well-known method is principal component analysis (PCA)<sup>134, 136-148</sup>. PCA is a technique that is fairly fast and straightforward to use and is unsupervised, which means that it needs no initial user input. PCA is also often used as a starting point for other, more sophisticated techniques. Another unsupervised technique is independent component analysis (ICA) and is in many respects similar to PCA.

Parallel factors analysis (PARAFAC) is a much more computationally demanding technique that needs some user input but has been shown to give results that are superior to PCA<sup>149, 150</sup> (also see chapter 5). Its long computation time makes it however useless for the routine analysis of large datasets. It demands certain knowledge of the dataset because the number of resulting components has to be defined prior to computation.

Probabilistic latent semantic analysis (pLSA)<sup>149</sup> is a highly supervised technique, which needs classification of classes prior to analysis. This seems like a disadvantage, but most often, enough prior knowledge is available to define regions in the sample that are supposed to show specific spectral profiles. Using this technique, a very good classification of tissue types can be made. The needed prior knowledge is however a drawback compared to unsupervised techniques like PCA.

Many other techniques can be used but it is beyond the scope of this thesis to go into further detail on them. Canonical correlation analysis can be used to combine the information of two independently measured datasets originating from the same sample<sup>151</sup>. In this way, a correlation can be made between two complementary multidimensional datasets, e.g. acquired using both MALDI and SIMS analysis.

## 2.9 *Polymer mass spectrometry*

Mass spectrometry is an important analytical tool in polymer chemistry. Because mass spectrometry can be used for determining several chemical properties that are important to the materials properties of polymers, it is often used in polymer chemistry, both in industry and science. To give some background for the polymer imaging studies performed during this project, the most important analytical considerations as well as the most important properties that can be determined by mass spectrometry are given here. The focus lies on the techniques that are applicable for imaging MS. A more extended discussion about polymer imaging MS is given in chapter 3.

## 2.9.1 Polymer properties commonly identified by MS

### 2.9.1.1 Monomer identity

The monomer identity is the most important parameter of the physical and chemical properties of a polymer. With mass spectrometry, it can be determined by measuring the  $m/z$  difference between two repeating peaks in the polymer distribution spectrum. When using a sufficiently accurate mass analysis technique, this gives the elemental composition of the monomer unit.

### 2.9.1.2 Number average molecular weight

This parameter gives the average molecular weight of all the molecules in a polymer mixture, calculated by dividing the sum product of all molecular masses ( $m_i$ ) with their abundance ( $n_i$ ) by the total number of molecules. It is the best value to use when assessing properties in which only the number of particles counts, e.g. the change in solution properties.

$$M_n = \frac{\sum_i n_i m_i}{\sum_i n_i} \quad 2.6$$

### 2.9.1.3 Weight average molecular weight

This parameter takes into account the weight of each fraction of the polymer. This is especially important for applications in which the size of each molecule matters, e.g. light scattering.

$$M_w = \frac{\sum_i n_i m_i^2}{\sum_i n_i m_i} \quad 2.7$$

### 2.9.1.4 Polydispersity

Polydispersity gives an indication of how broad the range of polymer molecular weights is in the molecular weight distribution. The polydispersity varies based on the used synthetic method. In order to do reliable polymer analysis with MALDI-MS, a low polydispersity is needed because of mass-dependant sensitivity<sup>66, 67</sup>. A single-length polymer has unity polydispersity.

$$D = \frac{M_w}{M_n} \quad 2.8$$

### 2.9.1.5 Endgroups

The endgroups of polymers determine their properties to a very large extent<sup>152</sup>. For short chain polymers, endgroups are more important with regards to their physical and chemical properties than for long chains because they encompass a larger fraction of the polymer. A reliable identification of the endgroups is crucial for further processing of the polymer. Endgroups can be reactive chemical moieties. These can be used for co-polymerizing a variety of precursor polymers.

### 2.9.2 Analytical techniques

In principle, all MS techniques can be used for polymer analysis. The type of information that is obtained however depends on the chosen technique. The ionization method influences the type of data that is seen. Also the limited mass range of some mass analyzers can be a restriction and instrument settings can bias the results. It is crucially important to be aware of these limitations, but doing so, MS can provide information that cannot be obtained otherwise.

Because imaging MS is restricted to surface ionization methods, other methods, like electrospray ionization<sup>153</sup>, pyrolysis<sup>154</sup>, electron impact ionization and chemical ionization<sup>155, 156</sup>, although important to polymer MS, are not covered here. Separation methods, including chromatographic techniques are commonly used in polymer MS analysis, especially when blends are analyzed, but these are beyond the scope of this thesis.

MALDI is the most common off-surface polymer ionization method<sup>66, 79, 152, 157-159</sup>. It can be applied to analyze intact molecules of polymers with molecular weights ranging up to 106 Da when using time of flight analysis. MALDI is typically coupled to high resolution mass spectrometers and offers the possibility to do MS/MS analysis. Figure 2.9 e and f show MALDI mass spectra of poly(ethylene glycol (PEG) with  $M_n \approx 1500$ , using 2,5-dihydroxybenzoic acid (DHB) as a matrix. These spectra were acquired on respectively an in-house built 7 T MALDI-FTICR-MS and a Waters Synapt HDMS (Waters Corporation, Manchester, UK). The FTICR spectrum looks much cleaner, mainly due to more extensive filtering and collisional ion cooling before the final mass analyzer. The FTICR-MS measured spectrum shows  $\text{Li}^+$ -cationized PEG and the spectrum acquired on the Synapt shows mainly  $\text{Na}^+$ -cationized species. Both  $\text{Na}^+$  and  $\text{Li}^+$  are good cationization agents for PEG. The choice of ionization agent can greatly influence the MS results, especially the molecular mass distribution<sup>160</sup>. The added ionization agent is typically chosen dependant on the nature of the polymer. It is also important to match the polarities of the used matrix with the polarity of the polymer. Because MALDI sample preparation is typically done by solution-phase mixing, good solubility of the

complete polymer is important in order to get a reliable molecular weight distribution<sup>161</sup>. Dry preparation methods have shown to be advantageous, especially for the analysis of polymers that are hard to dissolve<sup>81, 82, 162</sup>. MALDI has so far not been successful in the imaging of polymers. Chapter 3 provides a more in-depth discussion about the applicability of MALDI for the imaging of polymer systems.

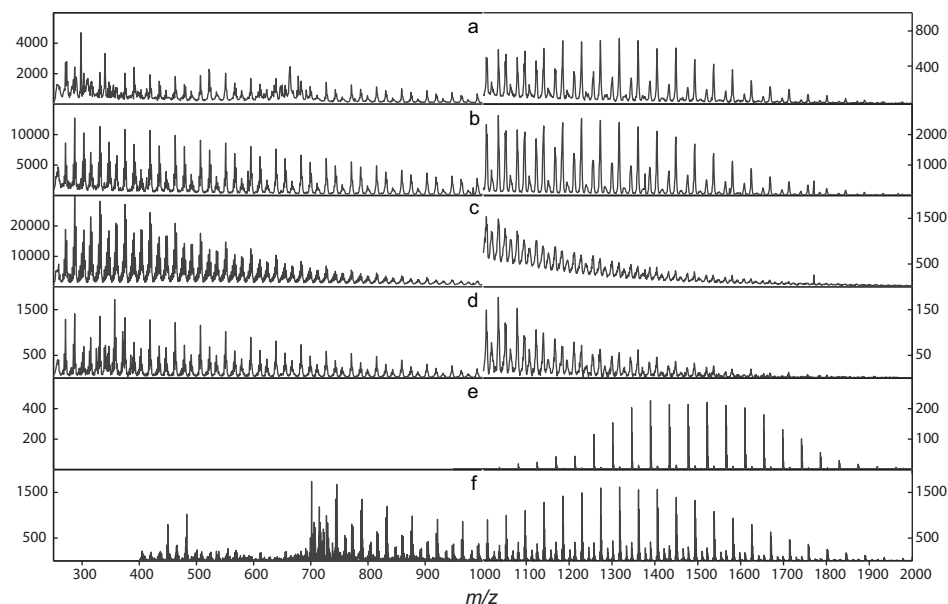


**Figure 2.9** A comparison of the spectra obtained from poly(ethylene glycol) ( $M_n \approx 1500$ ) with different MS techniques. The left and right panels for each spectrum show a different intensity scale. Experiments were done for a: MESIMS, b: meta-MESIMS using 1 nm Au metallization, c: meta-SIMS using 1 nm Au coating, d: SIMS without sample preparation, e: MALDI-FTICR-MS and f: MALDI orthogonal TOF using reflectron mode.

Desorption electrospray ionization (DESI) is suitable for analyzing low molecular weight polymers<sup>83, 163, 164</sup>. DESI delivers information that is similar to that obtained by MALDI or ESI however sample analysis times for DESI are much shorter due to the little sample preparation that is needed. DESI can be used for imaging, but the wetting of the surface poses a high risk of analyte diffusion and the imaging resolution is limited. Polymer mixtures will most probably give biased results, depending on which polymer ionizes more easily. However, more study would be needed to thoroughly assess the capabilities of DESI for the imaging MS of polymers. TOF-SIMS delivers a completely different type of information than MALDI and DESI. Due to the nature of this technique that causes fragmentation at the surface,

spectral analysis is typically based on structural fragment ions. The fragment ion peaks deliver useful structural information but no reliable molecular mass data. So far, out of all ionization techniques, only SIMS had been broadly applied for the imaging MS of polymers<sup>165-168</sup>, often in an industrial setting. The fact that little sample preparation is needed makes it more versatile for the analysis of a broad range of polymers. The advantage of little or no sample preparation makes imaging of samples containing multiple types of polymers feasible. When using the MALDI sample preparation, MESIMS can be done, giving results that are similar to MALDI. There is however the risk of segregation in the drying matrix/polymer mixture, which can cause sample inhomogeneity<sup>169, 170</sup>. Figure 2.9 a-d give SIMS spectra of poly(ethylene glycol (PEG) with  $M_n \approx 1500$ . The spectrum in Figure 2.9-a is an MESIMS spectrum and shows the result of matrix coating in SIMS: giving much higher intensity peaks for the intact polymer molecules, when comparing it to the non-treated SIMS sample (Figure 2.9-d), in which polymer fragments are predominant. The application of Au coating increases the spectral intensity over the whole mass range for both MESIMS (Figure 2.9-b) and regular SIMS (Figure 2.9-c) but does not significantly influence the molecular mass distribution.

**Table 2.1** Weight average molecular weight ( $M_w$ ), number average molecular weight ( $M_n$ ) and polydispersity ( $D$ ), compared for poly(ethylene glycol) ( $M_n \approx 1500$ ) using four different types of analysis methods. Comparison is made between two MALDI experiments: using FTICR analysis and orthogonal TOF analysis; and two SIMS experiments: MESIMS and metal assisted MESIMS (using 1 nm gold), both using TOF analysis.

<b>technique</b>	<b><math>M_w</math></b>	<b><math>M_n</math></b>	<b><math>D</math></b>
MALDI-FTICR	1518	1487	1.02
MALDI-O-TOF	1407	1371	1.03
MESIMS	1352	1318	1.03
meta-MESIMS	1330	1296	1.03

In table 2.1 the values for  $M_n$ ,  $M_w$  and  $D$  are compared. Because the SIMS spectra and the spectra acquired using the Synapt MALDI TOF do not show a molecular weight distribution that has the typical Gaussian-like shape, the peaks that correspond with the peaks used for calculating the MALDI-FTICR-MS molecular weight distribution are used. Because the FTICR data predominantly contains  $\text{Li}^+$ -ionized species and the Synapt and SIMS data mainly  $\text{Na}^+$ -cationized species, the  $\text{Na}^+$  peak that corresponds with the  $\text{Li}^+$ -cationized peak is picked (e.i. the peak with a mass of 16 Da higher). This selection of distribution range inevitably leads to an overestimation of  $M_n$  and  $M_w$  and an underestimation of  $D$ , because it cuts off the spectra at the lower end of the distribution. The meta-SIMS and bare-polymer SIMS spectra do not show a

molecular mass distribution but only fragments (see figure 2.9) and are therefore disregarded. The results show a comparable, and low, polydispersity for all the samples.  $D$  is the lowest for the FTICR-MS measured sample, which is due to the lack of fragment-ions at lower mass.  $M_w$  and  $M_n$  are clearly lower for the spectra acquired with SIMS, with no major difference between MESIMS and meta-MESIMS. Also  $M_n$  and  $M_w$  for the o-TOF spectrum are significantly lower, however the value given in table 2.1 is still an overestimation due to the low-mass cut-off in the analysis.

### *2.10 Current status in imaging mass spectrometry*

Despite the fact that MS imaging is becoming a mature field, there still are some major hurdles to be taken before large-scale application, for instance in hospital pathology labs or in industry, is feasible.

Matrix effects are a major issue in MS imaging, irrespectively the ionization technique that is used. Matrix effects, also called ion suppression effects, are caused by the fact that different compounds have different ionization efficiencies. As a result, the easier ionizable compound will suppress the signal of a compound that is ionized much more difficultly. In an imaging experiment, this means that the concentration distribution of one compound can influence the signal intensity distribution of another compound that is evenly distributed<sup>1-3</sup>. Not only the molecular, but also the structural environment influences the intensity of the analyte signal. Several solutions have been proposed to this, including the application of a calibration standard on a blank sample to assess the ion suppression effect for that specific compound<sup>4</sup>. Running good calibration standards to circumvent ion suppression is absolutely necessary to give reliable distribution maps and inevitable when quantification is needed.

Characterization of compounds is another issue that requires close care. Quite often, an assessment of the molecular structure that belongs to a peak can be made based on correlating peaks or prior knowledge about the sample. In case of sufficiently high mass resolution, molecular formulas can be assigned to peaks based on their accurate mass measurement. These methods do however rely on indirect evidence. To be certain about a structure, MS/MS experiments are necessary. This is getting more focus in the imaging MS field nowadays. MALDI MS imaging instruments now often have MS/MS capabilities. In the SIMS field, traditionally a field in which people were looking at fragment ions and elements, the capability of detecting high-mass secondary ions now also requires MS/MS methodologies. Unfortunately, tandem SIMS instruments are still very experimental<sup>5, 6</sup> and not currently commercially available, but they certainly will be in the near future.

### 3 MASS SPECTROMETRIC IMAGING OF POLYMER SYSTEMS

---

Imaging mass spectrometry can be of great help in getting a better understanding of the spatial organization of polymers and polymer additives like colorants, fillers and lubricants. The two most common imaging mass spectrometry techniques, SIMS and MALDI, can both be used for this purpose. SIMS has an established position as an imaging technique. MALDI however has only been widely applied for bulk polymer analysis whereas MALDI imaging applications are limited to biological studies. The widespread application of MALDI as an imaging MS technique is challenged mainly by sample preparation. Good analyte solubility is a requirement for MALDI sample preparation using solution-based techniques. In contrast to biological samples, for which most MALDI imaging sample preparation protocols were developed, polymeric systems are relatively homogeneous. Consequently, a large fraction of the sample is dissolved when applying a matrix solution. Dissolving a large fraction of the sample leads to non-ideal matrix/analyte ratios and to a higher risk of lateral diffusion. Another challenge is that MALDI relies on the extraction and in-matrix incorporation of a representative fraction of the sample. Mixtures of co-polymers with different compositions and polymers with different chain lengths have different physical properties and are therefore prone to selective extraction. Another challenge lies in the analysis of polymer imaging datasets. Where MS images are typically created based on a selected ion peak, this leads to low intensities for a single polymer MS peak because of the large number of peaks for the molecular weight distribution that is typically seen for polymers. This collection of low intensity peaks can be correlated using statistical data analysis techniques, thus enhancing the contrast in the images and making the distribution mapping of low-abundant polymers possible. This chapter is an overview of different challenges in sample preparation and data analysis that are faced in polymer imaging mass spectrometry and offers both solutions and directions for further development.

---

### 3.1 Introduction

The main driving force behind the development of novel mass spectrometric (MS) imaging techniques and methodologies, especially those using matrix assisted laser desorption/ionization (MALDI) as an ionization method, has been the studying of biological samples. The application of a MALDI matrix and the accompanied sub-surface analyte extraction as well as on-surface analyte incorporation has opened new pathways for the exploration of biologically relevant samples. Although widely applied as a polymer analysis technique<sup>66, 152, 154, 158, 169, 171, 172</sup>, MALDI has however not made a breakthrough as a polymer imaging technique so far.

Imaging MS methods for polymer analysis have been mainly limited to secondary ion mass spectrometry (SIMS), typically using time of flight (TOF) analysis. TOF-SIMS imaging has long been a widely applied imaging technique for polymer analysis<sup>12, 168, 173-176</sup>. Applications using SIMS imaging range from the imaging of coatings<sup>177, 178</sup>, oil paintings<sup>179</sup>, polymer additives<sup>180</sup>, polymers for drug delivery<sup>165, 181-183</sup>, the screening of polymer derivatizations<sup>184</sup>, polymer inter-diffusion<sup>185</sup> and to resolve a polymer's surface organization<sup>166</sup>.

SIMS and MALDI each have their own advantages and disadvantages in polymer analysis. MALDI gives intact polymer signal, which makes determination of molecular weight and polydispersity possible. MALDI can be used for a wide range of polymers, but with the restriction that a suitable matrix is needed and the polymer can be incorporated into this matrix. This incorporation most often done by dissolving the analyte into a solution that contains the matrix, but for some polymers, solubility is an enormous challenge. This has been circumvented for bulk polymer analysis by dry matrix preparation methods<sup>82, 162</sup>, but because of the extensive contact that is needed between polymer and matrix, typically done by grinding, this method is not suitable for the imaging MALDI-MS of polymers.

Because SIMS requires little or no sample preparation, the nature of the polymer is not so much of an issue for SIMS. As long as sufficient charge compensation can be achieved for the typically insulating polymers, a SIMS analysis can be performed. Charge compensation is especially necessary for imaging SIMS, in which charge buildup at the sample surface will cause fluctuations in the extraction field and therefore blurring of the image. Where MALDI can result in intact polymer ions, SIMS typically gives structural polymer fragment ions. These ions are polymer-type specific, making SIMS an ideal tool for the imaging of distributions of different polymers. For this purpose, SIMS is a widely applied technique in materials analysis for which standard spectra are readily available<sup>168</sup>.



Imaging MS of polymers is therefore on the one side a mature field, but on the side where most of the recent developments in imaging MS have taken place, namely MALDI-MS imaging, polymer science has some arrears to catch up with. Several challenges, insights and recommendations, along with some examples regarding the use of imaging MS, and especially imaging MALDI MS, are discussed in this chapter.

## 3.2 Experimental challenges

Pretty much all experimental challenges that are faced when doing MS imaging in general have to be coped with when imaging polymeric systems. There are however some additional issues when measuring a polymeric system, especially if it involves some chemical complexity, polydispersity, crosslinking, solubility and polarity.

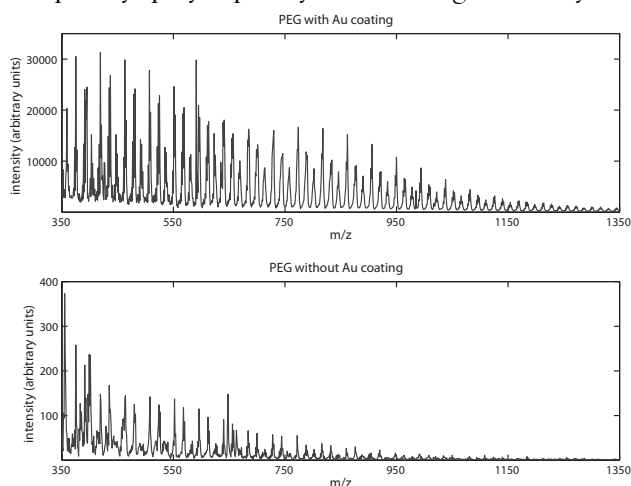


**Figure 3.1** Comparison between Au coated (top) and non-Au-coated (bottom) poly(ethylene glycol).

### 3.2.1 Sample preparation

Just like in general for imaging MS, successful sample preparation is the key step towards the successful analysis of a sample.

SIMS requires little or no sample preparation. The application of a gold coating can be beneficial as means of charge compensation and ionization enhancement for the high-mass polymer molecules<sup>116, 118, 145</sup>. The enhancement of molecular/high-mass fragment signal is shown in figure 3.1 for poly(ethylene glycol) (PEG). In some cases, matrix coating, as done in a matrix enhanced-SIMS (MESIMS) experiment, could be of benefit.

For MALDI-MS imaging, sample preparation is the key step toward successful analysis. Typically, sample pre-treatment and matrix coating are the most important

steps. There is not much known about possible pre-treatment methods for polymers, which is understandable as the development of matrix-coating methodologies is generally the first step in the development of a sample preparation protocol. The development of reliable matrix application strategies for polymer imaging is the key step towards its success. There are several issues that are less important to MALDI imaging MS of biological samples, but are a big issue in the imaging of polymers.

- *The solvent choice.* Normally, the matrix solvent is chosen such, that both matrix and analyte are well soluble. This can become a problem for polymers. In a polymer system, polymer typically also forms the structure of the sample. Therefore, the analyte is not extracted from a support matrix like in MALDI tissue analysis, but the support matrix is dissolved completely, taking away the mechanical structure of the sample. Dislocation of the polymer, not only by diffusion but also by a flowing polymer-solution is an obvious consequence.
- *Extraction of a representative analyte composition.* Although the analyte extracted in case of a biological sample is not necessarily representative for its composition, the typical molecules looked at are peptides, proteins and lipids, for which extraction is fairly predictable. When looking at a polymer system, there can be co-polymers involved. These could consist of different compositions of the various types of polymers, giving different physical and chemical properties per polymer, which makes their extraction efficiency different as well. Different extraction efficiencies result in a biased mass spectrum, which gives an unfair representation of the molecular composition of the sample. Also, the extraction of shorter, and therefore less entangled polymers, could be more efficient than that of the longer, more entangled, chains. This leads to a bias in the molecular weight distribution when determining this from the mass spectrum. Finally, in case of a co-polymer that is synthesized from short-chain precursor polymers, extraction of these short precursor molecules, which typically have a higher diffusion rate and solubility, will inevitably be more efficient than extraction of the longer co-polymers. When there is only a minute fraction of the precursor molecule present, its detection is favoured over the full-length polymer. This is for example the case for the chain-extended polymer shown in figure 3.2. The same issue holds for a degrading polymer. When imaging a degrading polymer using MALDI, degradation products will be extracted from the sample easiest and show up the strongest in the mass spectrum.

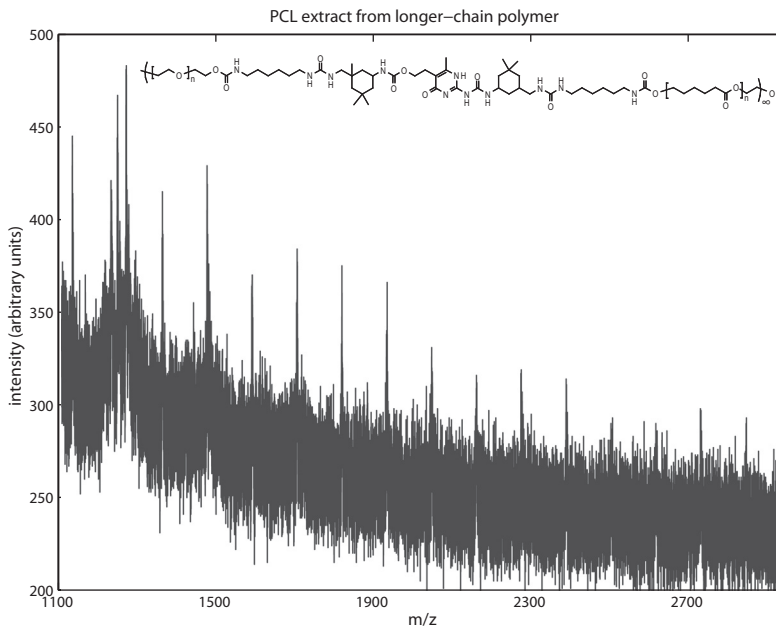


**Figure 3.2** A MALDI mass spectrum of a chain-extended polymer consisting of poly(ethylene glycol) ( $M_n = 6000$  g/mole) and polycaprolactone ( $M_n = 1250$  g/mole) precursor polymers in a 9:1 w/w% ratio chain-extended with a Ureidopyrimidinone-moiety (see structure in inset). The peak distribution shown has a 114 Da (PCL monomer unit) repeat pattern. It is obvious that this signal does not result from the chain-extended polymer, but from an extracted PCL fraction, being either the precursor polymer or a degradation product.

- Getting a proper analyte/matrix ratio is crucial in getting good MALDI signal. Whereas in case of biological samples, this ratio is quite easily obtained because only a small part of the sample is extracted into the matrix, this is far from trivial for a polymer sample. The application of a matrix solution may result in several dissolving mechanisms, depending on the polymer properties including solubility and penetrability for the solvent. In certain cases it first makes the polymer swell, in other cases, only the top few molecular layers are dissolved. After applying matrix solution, a certain matrix/analyte solution is reached. The ratio between matrix and polymer is however nowhere near ideal for MALDI analysis. Because so much polymer material is present at the surface, the ideal matrix/analyte ratio will probably never be reached unless only part of the polymer is dissolved, or no dissolution of the polymer is necessary. This would involve novel strategies in dry matrix preparation. An additional problem with reaching a proper polymer/matrix ratio, is the solvent-rich environment that is needed

for proper mixing of the large quantities of both matrix and polymer. This leads to large crystals (also see figure 3.3), which is detrimental to the image quality when high image resolution is needed.

- *Solvent compatibility of matrix spraying/deposition devices can restrict the choice of matrix application method.* Automated matrix deposition machines often contain glues and tubing that are not resistant to the solvents needed for dissolving certain types of polymers. There is always the option of manual spraying from a glass TLC-sprayer, but microdroplet deposition, which could be the perfect way of circumventing issues like diffusion and bad analyte/matrix ratio is not currently possible with solvents like dichloromethane and tetrahydrofurane.

### 3.2.2 Data acquisition techniques

Data acquisition is nowadays not the hardest step in MS imaging. This is not different for polymer imaging. A few comments on the most common imaging MS acquisition techniques, SIMS and MALDI, are given below.

In case of SIMS, charge compensation is usually necessary because of the insulating nature of polymers. This is often done naturally by the gold coating that is applied for high-mass sensitivity enhancement. The use of an electron flood gun is a good choice too, but care should be taken about the possible electron-induced degradation of the polymer. Another aspect to take into account is the reliability of a molecular weight (or fragment) distribution. SIMS is not a molecular desorption technique. This implies that the molecules at the surface are fragmented as the measurement progresses. Therefore the ions measured are often fragments of the molecules at the surface. Because of this known fragmentation, it is not possible to reliably determine a molecular weight distribution of a polymer using SIMS. However, because the energetic properties of the primary ions may be assumed constant for each ion, fragmentation will happen based on the same mechanisms upon every ion impact. This means that there will be a fragment molecular weight distribution rather than a molecular weight distribution visible in the resulting spectrum. Longer polymers will typically give longer fragments. When both acquisition parameters and the chemical environment are the same for two samples, their polymer chain lengths can be compared based on their fragment distribution.

MALDI analysis works pretty much the same for polymer imaging as for the imaging of biological samples. MALDI MS imaging is however a technique that has not been used a lot for polymer analysis so far, partially owing to sample preparation issues mentioned above. It is therefore hard to assess what issues have to be tackled when doing MALDI MS imaging of polymers. MALDI would however be the technique of

choice when values like molecular weight distribution and polydispersity need to be calculated.

An example of MALDI MS imaging is given in figure 3.4, the MALDI MS imaging result of figure 3.3. A sample carrying poly(ethylene glycol) ( $M_n = 1500$ ), Rhodamine 6G, poly(tetrahydrofuran) ( $M_n = 2000$ ) and poly(propylene glycol) monobutyl ether ( $M_n = 2500$ ) was spray-coated with 2,5-dihydroxybenzoic acid (DHB), sprayed from a 1% solution in 2:1 ethanol/water using a manual pneumatic sprayer. NaI was added to the spray-solution as an ionizing agent in a ratio of 1:100 relative to the matrix. After matrix-deposition, the sample was covered with a 2 nm thick gold-layer to reduce localized charges. The sample was then analyzed using a customized TRIFT mass spectrometer. After data acquisition, the different chemical components were extracted using PCA with VARIMAX optimization. The MWD of PEG corresponds fairly well with its expected profile. For PPG, only a low-region distribution is seen, a higher mass distribution has too low intensity to see from the spectrum, but still largely compensates the low-mass bias of the other distribution to give a total  $M_n$  near 2500. Poly(THF) however, is only seen at very low mass. One of the reasons for this may be bad solubility in the matrix solution of choice (2:1 ethanol/water). This is also supported by the low overall intensity given by poly(THF), a reason why it only shows up as the 12<sup>th</sup> principal component.

### 3.3 *Data analysis matters*

#### 3.3.1 **Manual analysis**

When doing MS on polymers, they are generally very easy to distinguish. Their characteristic molecular weight distribution profile, shows up readily in the mass spectrum. It is however much harder to determine the exact structure of the polymer. For homo-polymers, polymers that contain only a single type of monomer, this is fairly straightforward, but for polymers that are built up from different types of monomers things get complex very quickly. Still, the distribution of peaks in the spectrum clearly shows the presence of a polymer. The recognition of this distribution can often be done manually. This distribution can then be used for determining the various important measures for polymer analysis, including monomer identity, number average molecular weight ( $M_n$ ), weight average molecular weight ( $M_w$ ), polydispersity ( $D$ ), types of endgroups and the cation that carried the charge for ionization.

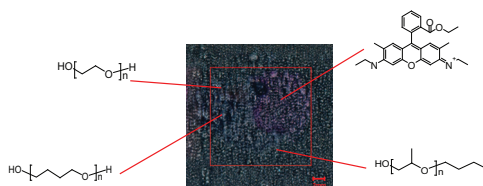


**Figure 3.3** A test sample for MALDI MS imaging of polymers, including poly(ethylene glycol) ( $M_n = 1500$ ), Rhodamine 6G, poly(tetrahydrofuran) ( $M_n = 2000$ ) and poly(propylene glycol) monobutyl ether ( $M_n = 2500$ ). The optical image was taken after matrix deposition.

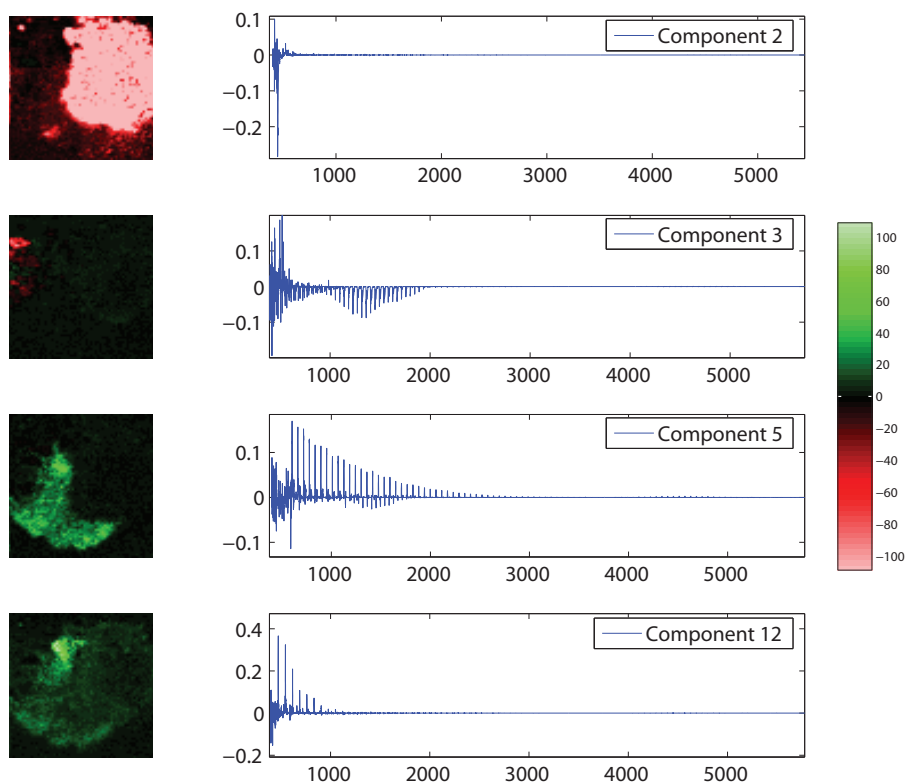


**Figure 3.4** PCA with additional VARIMAX optimization, done on the MALDI microprobe imaging results. The various compounds were very-well resolved: Component 2: Rodamine 6G, Component 3: PEG, Component 5: PPG, Component 12: poly (THF). The fact that poly(THF) shows up at higher-numbered principal component indicates that this polymer is present in lower amount, or it is measured less-efficiently. The higher-numbered components that are not shown mainly contain Rhodamine 6G, which gave the predominant throughout the dataset.

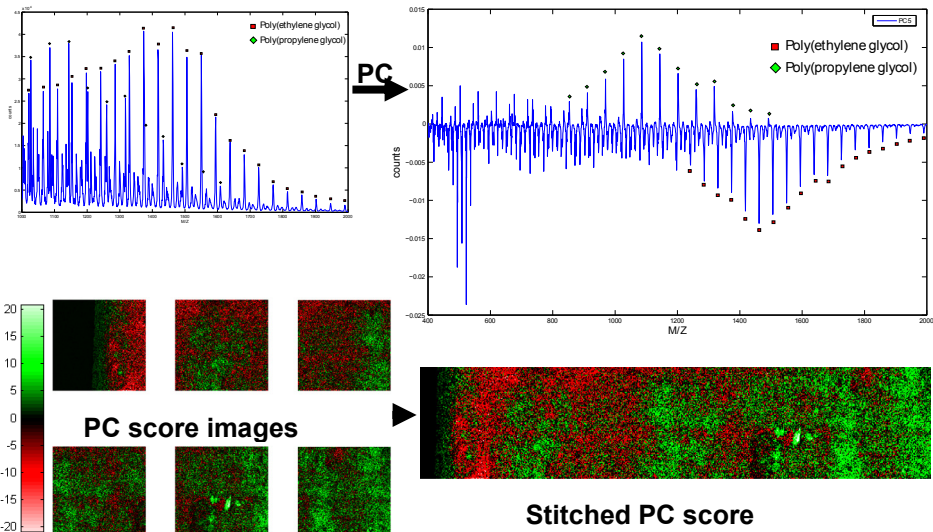


**Figure 3.5** An example in which PCA splits out two different polymer components that show largely overlapping distribution profiles. The PCA results are used fully benefit from the intensity in all peaks in the polymer distributions when plotting their localization. These images were recorded using TOF-SIMS in the positive ion mode with  $\text{In}^+$  primary ions.

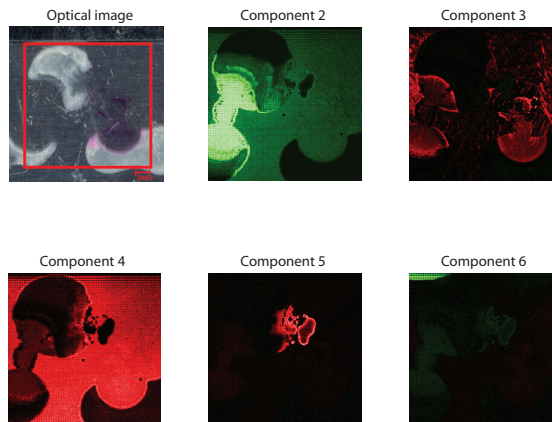


**Figure 3.6** TOF-SIMS results of a sample containing several polymers. The images show an optical representation of the sample (top left) and PCA with VARIMAX optimization results for the several polymers. Component 2: Rhodamine 6G, Component 3: PEG, Component 4: ITO substrate, Component 5: PPG, Component 6: silicone (contamination), Component 1 is not shown, as it is non-specific (it contains a representation of the full dataset).

When doing MS imaging, other aspects have to be accounted with. A single peak is usually selected to plot the distribution of a certain compound. It would however not be wise to do so in case of a polymer. The selection of a single peak gives a much lower image contrast than the selection of all peaks belonging to the polymer. This is not very convenient and can actually be very time-consuming when it needs to be done for a very polydisperse polymer, therefore automated routines are extremely helpful.

Another issue in MS imaging, is the presence of other components. Especially when a large area is imaged, and the polymer is present only in a small part of the sample, its distribution of peaks can easily disappear in the background noise of the total-image spectrum. This disappearance in background noise is an issue in general for the MS imaging of trace components, but it is even more critical in the case of polymers because polymers do not show up as a single peak in the spectrum and therefore have a much lower single-peak S/N.

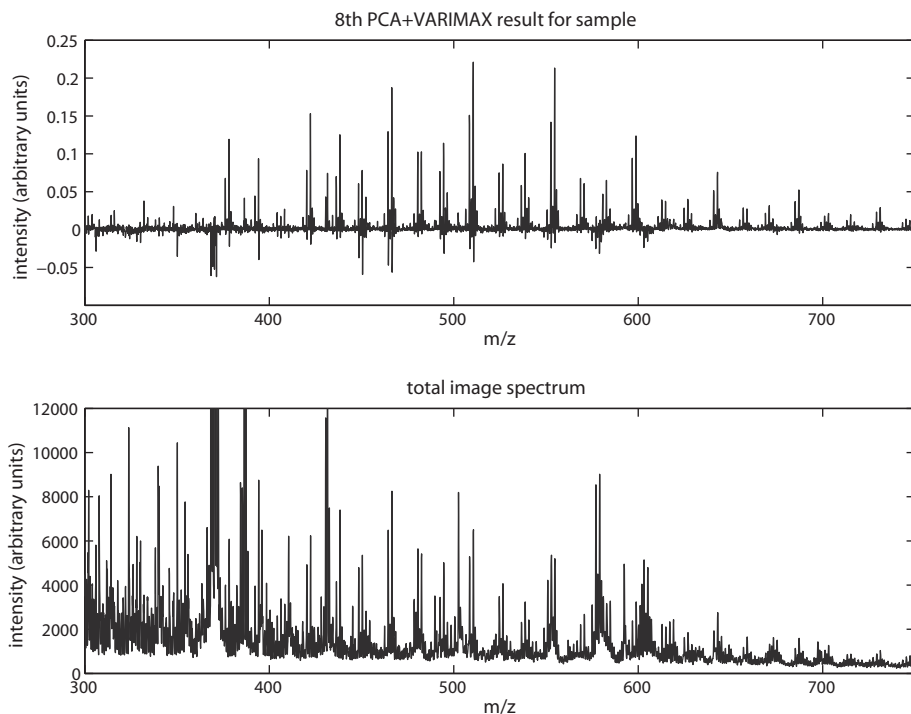


**Figure 3.7** Comparison between a total-image spectrum (bottom) and a selected component spectrum after PCA with VARIMAX optimization. This example shows how hardly visible the polymer distribution is in the total image spectrum (note that this is a zoomed-in spectrum already, the highest peak is  $3 \times 10^5$  counts), but easily resolved after statistical data analysis.



### 3.3.2 Automated analysis

The two issues mentioned above can be largely circumvented by the use of (partially) automated analysis techniques. Some techniques for semi-automated polymer analysis exist<sup>186</sup>, but are based on a considerable amount of prior knowledge. The use of statistical data analysis strategies like PCA can for instance pick out correlated profiles that are otherwise easily overseen.

The first issue is the fact that the complete polymer distribution is quite hard to select for plotting a localization image. Usually it overlaps with other peaks and the selection of each single peak is very time-consuming. Figure 3.5 shows how two overlapping distribution can be separated by using PCA as a data analysis technique. The poly(ethylene glycol) and poly(propylene glycol), each of which is the a component of a separate type of Liquitex acrylic paint, are distinguished into two separate layers. The polymer distributions are largely overlapping. Only selection of each peak from each polymer distribution would give the same type of contrast. PCA resolves both distributions as anti-correlated combinations of peaks and makes plotting in a single image easy.

The second issue is the bad visibility of a polymer distribution in the total image spectrum. Often, manual MS imaging analysis is done based on the peaks that are seen in the summed spectrum of the total image. When compounds give very weak peaks or are simply very low abundant, they are not seen in the total image spectrum. Figure 3.4 is an example of this. The polymer distribution is not seen in the spectrum summed over all image pixels, but is easily resolved after PCA. A polymer is not easily observed in the total-image spectrum. Statistical data analysis can circumvent this by finding the highly correlated peak distribution of a polymer compound.

## 3.4 Conclusions and recommendations

SIMS has proven a very powerful technique in polymer imaging. The great advantage of SIMS is the little sample preparation that is needed. As a result, polymers with different physical and chemical properties can be analyzed in the same imaging experiment. Also samples that include both polymer and biological structures can be analyzed, giving both biochemical and polymer-related information. The latter is also shown in chapter 7 of this thesis. The developments within the SIMS field that focus on detecting higher-mass molecules and molecular fragments through softer ionization mechanisms will only increase the value of this technique in the polymer field by making molecular (fragment) measurements more feasible.

MALDI MS imaging of polymers struggles with some constraints, that need to be tackled before it will be widely applicable. The issues that arise in the sample preparation process are the major hurdle to take. Conventional sample preparation techniques like matrix solution spraying may even never deliver reliable results. The solution should probably be sought in the use of different types of matrixes, like ionic matrixes or nanoparticles, or in completely novel, dry matrix preparation techniques. Avoiding solvents would already tackle many of the issues in sample preparation, including the bad matrix/analyte ratio, diffusion and MWD bias through extraction differences between low- and high-molecular weight species.

## 4 FAST AND AUTOMATED LARGE-AREA IMAGING MALDI MASS SPECTROMETRY IN MICROPROBE AND MICROSCOPE MODE.

This chapter is based on:

Klerk, L. A.; Altelaar, A. F. M.; Froesch, M.; McDonnell, L. A.; Heeren, R. M. A. *International Journal of Mass Spectrometry* **2009**, *285*, 19-26.

---

Since the introduction of matrix-assisted laser desorption/ionization (MALDI) imaging mass spectrometry (imaging MS), numerous instrumental developments have been presented. The introduction of microscope MALDI imaging MS was a major breakthrough, making micron-range resolution MALDI imaging of kiloDalton mass species possible. We discuss new developments that makes large (cm range) field of view, high resolution ( $\mu\text{m}$  range) microscope mode imaging mass spectrometry (imaging MS) possible in a single experiment, using three different data acquisition approaches simultaneously. We demonstrate how a combination of these acquisition approaches is used to correlate mass spectral and high resolution imaging data.

---

## 4.1 Introduction

Since its introduction by Hillenkamp et al.<sup>50, 187</sup>, the development of matrix-assisted laser desorption/ionization (MALDI) mass spectrometry has made a major impact in many different disciplines, such as plant sciences<sup>188</sup>, polymer research<sup>66, 189</sup>, biomedical sciences, biomaterials engineering<sup>190</sup> and proteomics<sup>191</sup>. The introduction of MALDI imaging mass spectrometry (imaging MS) opened another range of applications by making it possible to visualize distributions of molecules at surfaces<sup>192, 193</sup>. This broad applicability is the driving force behind the numerous instrumental developments, including MALDI mass spectrometers that are customized to imaging mass spectrometry. As a result of these developments, imaging MS can now be performed on samples that vary in size from a rat whole-body section<sup>4, 194</sup> to samples that contain individual cells<sup>43, 103, 195</sup>.

Imaging MS is most commonly performed in the microprobe mode (see section 2.4 and figure 2.5, and figure 2.6 in this thesis). A disadvantage of microprobe mode MALDI imaging MS is the limited spatial resolution that can be achieved. In a conventional microprobe experiment, the spatial resolution is restricted by the spot-size of the laser. The spatial resolution can be improved by using an oversampling approach<sup>103</sup>. Although the focusing capabilities of modern optics allow submicron laser spot sizes<sup>196</sup>, the spot size of the laser should be sufficiently large to obtain good MALDI signal<sup>58</sup>, especially when measuring high-mass peptides and proteins. This limits the smallest useful spot size. In addition, the time a measurement takes increases quadratically with a decrease of the spot size.

Microscope mode imaging MS (see section 2.4, and figure 2.5 and figure 2.6 in this thesis) offers a solution to this issue. The ion optics of the TRIFT (triple focusing time-of-flight) mass spectrometer as was described by Luxembourg et al.<sup>107</sup> offer this feature. With this method, a large diameter (typically 200  $\mu\text{m}$ ) laser beam is used as a desorption and ionization medium. The resulting ion cloud is then transferred by the TOF system in which the ion optics have been designed to retain the original position of the ions orthogonal to the time of flight axis as the ions travel through the mass spectrometer. An image resolving power of less than 4  $\mu\text{m}$  can be reached by using this methodology. For a MALDI imaging MS experiment, this implies that the resolving power of an imaging experiment is typically limited by the size of the matrix crystals that are formed with the application of matrix at the sample surface. Obviously, microscope mode imaging MS can be combined with microprobe mode imaging MS by rastering the sample and still recording a microscope image at each position (figure 2.4).

The possibility to visualize distributions within the laser spot makes the use of larger laser spots possible and therefore cuts down the measurement time dramatically. The duration of an experiment is determined by the time required for mass analysis (following each laser shot), for transferring each of the mass spectra to memory, the number of laser shots at each position, the time taken to move the sample stage between pixels positions, and the number of sample stage positions in the experiment. The ability to record a 200  $\mu\text{m}$  diameter image with 4  $\mu\text{m}$  resolution with each laser shot using microscope imaging mass spectrometry, means that high resolution images of large samples (composed of a mosaic of high resolution images) can be obtained with a much smaller number of sample stage positions and laser shots than needed for a similar experiment in microprobe mode. Another advantage is that the lower number of laser shots leads to a longer lifetime of the laser. Moreover, the use of a large spot size makes low laser fluence possible, this results in less fragmentation of analytes, higher mass resolution and higher signal/noise ratio<sup>58, 197</sup>.

Until recently, these microscope-mode MALDI experiments were composed of a combination of multiple semi-continuous linescans<sup>71, 125, 198</sup>. Although this method has been proven to give high-resolution images at reasonable measurement time, the linescan methodology is a fairly laborious one because every linescan has to be started manually. Moreover, the number of laser shots that can be added per position is limited to one. Because of the continuous movement of the stage, the position is slightly different for each laser shot. This means that a new dataset (spectrum plus image) is generated for each laser shot. It would be more efficient to add up several datasets that are recorded at the same position. An unsupervised, automated approach that rasters the surface is therefore preferred. This would be similar to imaging as it is performed in most commercial MALDI-TOF microprobe instruments, in which the surface is rastered by moving the stage. Since the introduction of a new version of instrument control software (version 4.3 of WinCadence), rastering of the sample surface is also possible with a TRIFT instrument. In this paper, we show that this offers the opportunity to do fully automated MALDI-TOF microscopy experiments of large sample areas with high spatial resolution. The instrument can acquire microprobe and microscope mode MALDI datasets simultaneously. In this paper we show a new methodology in which both microprobe and high spatial resolution microscope mode imaging are combined. This leads to automated measurements and shorter acquisition times in both microprobe mode and microscope mode imaging.

## 4.2 *Experimental details*

### 4.2.1 **Instrumentation**

The MALDI-MS experiments were performed using a TRIFT II mass spectrometer (Physical Electronics, Eden Prairie, MN). The setup that was used is based on the system that was described previously by Luxembourg et al.<sup>107</sup> and in section 2.5.1 of this thesis. In this paper, we focus on new measurement methodologies that have been implemented since this first MALDI mass microscope was presented. Although we will mention all the fundamentals, we refer to Luxembourg et al.<sup>107</sup> for additional technical details as they were described earlier.

A schematic overview of the instrumental setup is given in figure 4.1. All main experimental features are controlled through the TRIFT electronics and WinCadence (Physical Electronics, Eden Prairie, MN) software. Mosaic-mode imaging is used as it is implemented in WinCadence version 4.3 and higher. This allows for automated large-area scans up to 256x256 positions. Each position is measured for typically 0.8 second (although this may be varied upon experimental needs), after which the stage is moved to the next position. The stage movement takes at most 0.3 seconds. Two different microprobe and one microscope signals can be acquired simultaneously, delivering three intrinsically aligned datasets. These methods are described below.

### 4.2.2 **Spectral detection system**

The detector of the TRIFT has two electronic outputs that are both suited to measure mass spectra: the backside of the dual microchannel plate (DMCP) and the electronic signal from the phosphor screen.

The DMCP signal is connected to the TRIFT's constant fraction discriminator (CFD) and Time to Digital Converter (TDC). This data is recorded through the TRIFT electronics and can be viewed directly in the WinCadence software that is the default acquisition control software for the TRIFT system. This is employed for quick assess of the data and to tune the various ion blankers. These blankers are used to define an  $m/z$  window of ions transmitted in order to measure microscope images of selected ions and to omit ions with a mass outside the mass range of interest. The disadvantage of using the CFD-TDC detection system is that all ions arriving in a certain time window (CFD dead time, typically about 10 ns) are counted as one. This results in a low overall dynamic range for high-intensity signals and is inherent to any ion counting method (figure 4.2). In a secondary ion mass spectrometry (SIMS)<sup>9</sup> experiment this is not an issue due to the low secondary ion count rate combined with the high repetition rate at which is measured. In a MALDI

experiment however the number of shots per position is much lower, the ion current much higher and the signal rapidly diminishes due to sample ablation. For MALDI it is common to record the complete output of the detector using an analogue-to-digital-conversion (ADC) system. In this case the phosphor screen electronic signal output is recorded with a digital oscilloscope computer board (Acqiris DP214 or Acqiris AP240 with Averager). The oscilloscope with averager is the preferred tool to use and constitutes a major improvement compared to the DP214: the direct averaging of all shots per position gives a considerable decrease in total data load, which makes experiments faster and the overall signal-to-noise ratio per position higher.

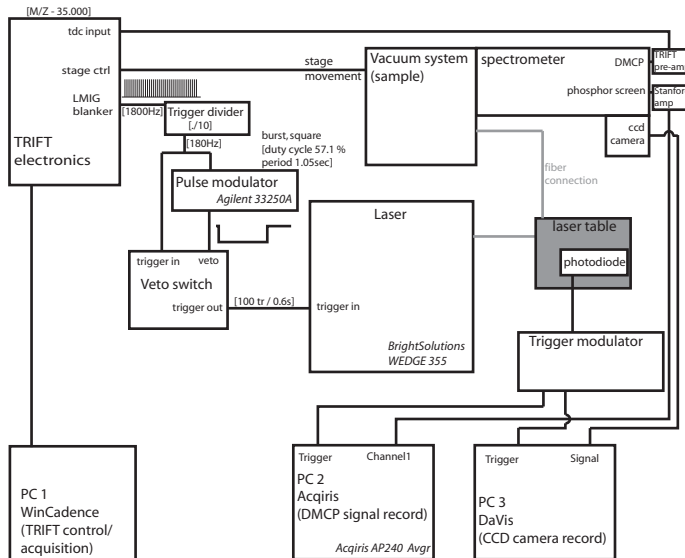


**Figure 4.1** Schematic of the MALDI TRIFT setup. Timing values are a mere indication and are subject to change according to experimental preference.

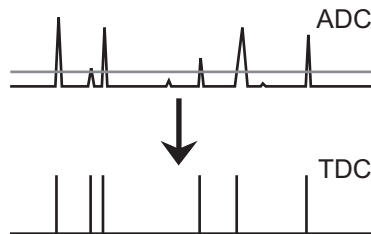


**Figure 4.2** A comparison between the use of an Analog-to-Digital Converter (ADC, top) and a Time-to-Digital Converter (TDC, bottom). The use of a TDC system leads to loss in dynamic range and loss of low (below cutoff threshold) signals. The use of a TDC does reduce the data size considerably.

The analog signal that is recorded from the phosphor screen is proportional to the number of electrons that hit the phosphor screen. Although the number of electrons that are generated in a DMCP setup depends on the DMCP settings, the velocity and nature of the detected ion<sup>199</sup>, the number of electrons that hit the phosphor screen is a value that is correlated with the number of ions that hit the DMCP and therefore a good measure for the signal intensity.

To accommodate the relatively high signals from the phosphor screen electronic output, we use an external amplifier (two channels in series of a Stanford Research Systems SR445A four channel DC to 350MHz amplifier) with an amplification factor of 25 for the recording of the analog signal. This external amplifier tops off the signals that exceed the saturation level. The topping-off of the signal could result in misleading signal strength but is minimized by choosing the proper laser power in order to keep the signal below the clipping threshold as much as possible. The lowest possible laser power would be just above the MALDI threshold, i.e. just high enough to obtain signal from the analyte<sup>53</sup>. Also the DMCP could suffer from saturation due to high ion loads. To reduce both DMCP and amplifier saturation, only the mass range of interest is measured. The TRIFT's blanking system is used to remove the less-interesting, high-velocity and highly abundant low-mass ions.

The measurement of the spectra from the phosphor screen with the ADC computer board is initiated by a trigger pulse that results from a photodiode that picks up stray light of the laser beam. This trigger source is used to minimize any possible jitter in the timing of the laser shot compared to the TRIFT's master trigger, which would lead to poor spectral resolution in case multiple spectra are summed.

### 4.2.3 Microscope image recording

To fully benefit from the high spatial resolution imaging capabilities of the TRIFT, even for large samples, a mosaic of microscope mode images can be recorded as the sample is rastered. The principles of ion-optical microscope image recording is explained by Luxembourg et al.<sup>107</sup>. These microscope mode images are recorded from the light output of a phosphor screen detector assembly (APD 30 25 12/10/12 PS I EDR 60:1 P-20 MgO-coated, Burle Industries GmbH, Baesweiler, Germany) using a fast CCD camera with 9.9- $\mu\text{m}$  pixel size (Imager 3, La Vision, Goettingen, Germany). A zoom lens (Thales Optem, Fairport, NY) is used to adjust the phosphor screen image size to fit the CCD chip.

When certain parts of the mass spectrum are selected, and all other ions are blanked, the microscope images give a very high resolution MALDI-TOF MS selected ion image in which spatial biomolecular details can be seen that cannot be resolved



otherwise<sup>107</sup>. After acquisition, the microscope images are combined into one overall image using in-house developed software<sup>198</sup>.

Total ion current (TIC) microscope images provide a more detailed view on the morphology of the sample. TIC microscope images and microprobe spectral data, that are intrinsically aligned with each other, are combined for a more thorough understanding of the sample, correlating morphological details with mass spectral data<sup>125</sup>.

#### 4.2.4 Laser system

MALDI is performed using the third harmonic of a BrightSolutions WEDGE, diode-pumped solid-state Nd-YAG laser source, at 355 nm wavelength and 5 ns pulse duration (Bright Solutions Soluzioni Laser Innovative srl, Cura Carpignano (PV), Italy). Lower-mode light is filtered out using an optical table with wavelength-specific mirrors. The 355nm light is then led to the TRIFT system through a fiber optic connection and fed into the vacuum chamber using a telescope-objective outside the vacuum and a high vacuum resistant objective inside the vacuum. The final effective laser spot at the surface has a diameter between 200  $\mu\text{m}$  and 80  $\mu\text{m}$  and a top-hat shape<sup>107</sup> (dependant on the exact configuration used).

#### 4.2.5 Materials

$\alpha$ -Cyano-4-hydroxycinnamic acid (HCCA) (>99% by HPLC) and Trifluoroacetic acid (TFA) (99.9%) were obtained from Sigma-Aldrich, Zwijndrecht, The Netherlands and used without further purification. Ethanol and acetonitrile (Analytical grade) were obtained from Biosolve and water was purified using Millipore Q-Gard 1 with Millipak 40 filter.

#### 4.2.6 Sample preparation

One sample is a part of a whole-body-section of a rat. The cross-section was kindly provided by Markus Stoeckli, Novartis, Basel, Switzerland. It was coated with  $\alpha$ -Cyano-4-hydroxycinnamic acid (HCCA) using a pneumatic spraying device ('SprayStation'<sup>112</sup>). This gave full matrix coverage in 65 spray-cycles, using a 5 mg/mL HCCA solution in 50% ethanol + 0.1% TFA. After this, the sample was gold coated (5nm), using a Quorum Technologies SC7640 sputter coater.

Two samples with 5x5 arrays of different peptides or lipids were prepared as a check for microprobe sensitivity and image resolving power.

The peptide mixture contained Bradykinin(1-5) (MW 572.7 Da, 2.0 pmol/ $\mu\text{L}$ ), Angiotensin II (MW 1046.2 Da, 1.2 pmol/ $\mu\text{L}$ ), Neurotensin (MW 1672.9 Da, 0.8 pmol/ $\mu\text{L}$ ) and bovine Insulin chain B (MW 3495.9 Da, 5.0 pmol/ $\mu\text{L}$ ) in a solution

of 5 g/L 2,5-dihydroxybenzoic acid (2,5-DHB) in Acetonitrile/water (30:70 v/v) and 0.1% TFA.

The lipid mixture contained cholesterol (MW 386.3 Da) and 1-hexadecanoyl-2-(9Z-octadecenoyl)-sn-glycero-3-phosphocholine 1-palmitic-2-oleic-phosphatidylcholine (PC34:1, MW 760.1 Da) at a concentration of 1 mg/ml in 5 g/L 2,5-DHB in methanol. All commercial samples were purchased from Sigma-Aldrich. The mixtures were spotted on a stainless steel plate using a Shimadzu CHIP-1000 (Shimadzu corporation, Kyoto, Japan) chemical inkjet printer. Droplet-to-droplet distance was 300  $\mu\text{m}$  for the peptide mix and 400  $\mu\text{m}$  for the lipid mix. The droplets were spotted in multiple cycles, with a total of 20 nL solution per position.

A transverse rat brain section (10  $\mu\text{m}$  thick on indium tin oxide coated glass) was kindly provided by Roger Adan, Utrecht University, The Netherlands. The section was prepared to test combined microprobe and microscope mode imaging. The section was stored at -80 °C and washed directly from the -80 °C storage, using 2 washing steps in 70% ice-cold ethanol for 1 minute each. After each washing step, the samples were dried under nitrogen flow. Matrix was applied from a solution of 4 mg/mL HCCA in 50% acetonitrile with 0.1% TFA, using a pneumatic spraying device (SprayStation<sup>112</sup>). A 2.5 nm gold layer was deposited for charge compensation<sup>43</sup>.

## 4.3 Results

### 4.3.1 Whole rat section

The whole-rat section was measured exclusively with TDC. The TRIFT's master trigger was used to trigger the laser and the data was recorded using the TDC that is default for the TRIFT system as it is in a SIMS configuration. The advantage of this method is that the system is easy to set up, the whole experiment can be controlled from one software package and data analysis is relatively straightforward. Inherent to TDC data acquisition is the resulting relatively small data size. The use of a very high laser rep-rate (1667 Hz), allows for operation at the MALDI threshold (at the risk of some "useless" shots<sup>53</sup>) and it yields sufficient spectral intensity at reasonable measurement time. The overall signal for low-mass compounds is intense enough to resolve localized features. This is shown in figure 4.3. Only the low  $m/z$  range was measured. Localization of phosphocholine ( $m/z$  184) between the organs and the pharmaceutical related localization at  $m/z$  224 in the kidney are seen. This method is less useful for the measurement of, typically low-abundant, high-mass ions.

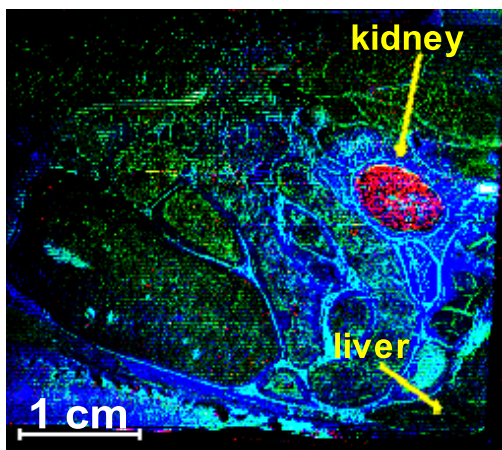


**Figure 4.3** Part of a whole-rat cross-section (head right, tail left). Various distributions are found in the low-molecular weight region. Blue: free choline ( $m/z$  104), green: phosphocholine (184  $m/z$ ), red: a pharmaceutical metabolite (224  $m/z$ ). Phosphocholine is localized between the organs, the pharmaceutical metabolite is concentrated in the kidney region. Note the difference in phosphocholine and free choline distribution. This shows how imaging MS can be used to trace pharmaceutical metabolites after in-vivo testing.

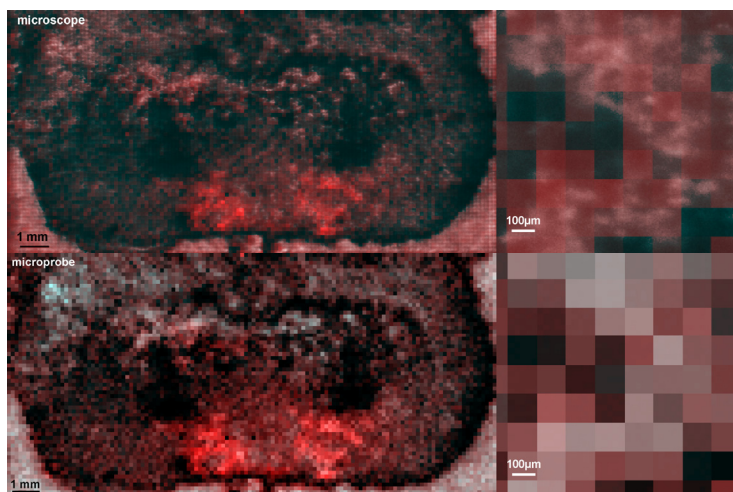


**Figure 4.4** Microscope and microprobe total ion images with a selected ion image ( $m/z=1120$  Da) overlay in red. The right images show part of the sample at full resolution. The microprobe selected ion image is naturally aligned with, and can be correlated with microscopic structures in the microscope total ion image.

However, the high rep-rate laser operation allows for quick imaging of (high-abundant) low-mass molecules like cholesterol, lipid headgroups and pharmaceutical compounds or metabolites. Conclusively, the main reason to do TDC measurements is for quick exploration of the data in order to set the instrumental parameters like the blanking of selected  $m/z$  values. ADC data is stored to perform post-acquisition analysis of high-quality data, whereas TDC is used for quick, on-the-fly access.

### 4.3.2 Droplet standards

The droplet standards were measured in microprobe mode using a 16x16 sample mosaic with 100  $\mu\text{m}$  step size and 87 summed shots per position at 100 Hz. Analog to digital conversion (ADC) of the phosphor screen signal was done with the Acqiris AP240 with Averager digitizer board. With this number of laser shots per position, TDC acquisition offers a too low dynamic range to be useful for data analysis. The use of a laser spot with a diameter of  $\sim 170 \mu\text{m}$  with a 100  $\mu\text{m}$  step size leads to a small overlap between positions. As signal yield has dramatically decreased after the 87 shots, this does not give a significant overlap effect, but creates a resolving power that is higher than the actual laser spot size<sup>103</sup>. This methodology gives very clear spectral details with a signal/noise of about 175. Despite the relatively low image resolution at which the samples were measured, after bicubic interpolation the images are in good accordance with the crystals that are seen in the optical images (figure 4.5, figure 4.6). This shows that interpolation can be beneficial for the visualization of data. Although this method is commonly used, it should always be noted that the resolution of the experiment is lower than the image suggests. This experiment thus shows that good results can be obtained in microprobe mode using ADC based data acquisition techniques. The spectral data is of high quality and the spatial data is accurate, yet restricted by the acquisition spot-to-spot distance. This offers the possibility to combine microscope and microprobe imaging MS in a single acquisition, as shown below.

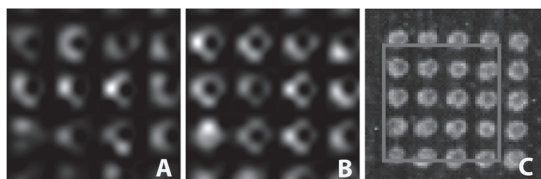


**Figure 4.5** Microprobe MALDI-TOF images of standards in DHB. Images are from specific peaks: Cholesterol (A,  $m/z$  386.3) and Phosphatidylcholine (B,  $m/z$  761.8). The samples were measured in a 16x16 mosaic. The localizations after simple interpolation correspond perfectly with the optical (scanned) image (C).

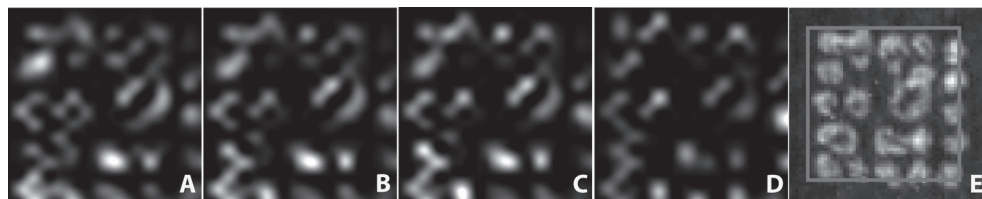


**Figure 4.6** MALDI-TOF images of standards in DHB. are from specific peaks: Bradykinin [1-5] (A,  $m/z$  573.3), Angiotensin II (B,  $m/z$  1046.6), Neuropeptide Y (C,  $m/z$  1673.0), Bovine Insulin chain B (D,  $m/z$  3497.1), The imaging MS images were measured in a 16x16 mosaic. The localizations after simple interpolation correspond very well with the optical (scanned) image (E).

### 4.3.3 Rat brain sample: microprobe and microscope imaging MS

A transverse rat brain section was measured in a combined microscope and microprobe mode experiment. The Acqiris DP214 board was used for the mass spectral detection. Microscope mode total ion images were recorded from the phosphor screen, using a CCD camera.

The whole brain sample was measured in 8 squares of each 32x32 positions. At each position, 9 spectra and 9 microscope total ion images were recorded and summed. The number of measured spectra at each position and the number of positions per experiment could not be further increased due to memory limitations of the data acquisition card. After acquisition, the spectra were summed to give one single spectrum per position and each position was inserted into one large microprobe hyperspectral datacube using in-house developed software. Additionally, the microscope mode total ion images were summed and one total ion image was constructed using custom-made software<sup>198</sup>. An overlay of a selected ion microprobe image ( $m/z=1124$  Da) is made with both microscope and microprobe total ion images (figure 4.4). It shows the advantage of the microscope imaging when it comes down to structural details in the image. Structural details in the microscope total ion image can be correlated with a microprobe selected ion intensity map.

## 4.4 Conclusions

The TRIFT instrument is demonstrated to be capable of doing  $\mu\text{m}$ -resolution microscope mode MALDI-TOF experiments of large areas in an automated way. In which the measured area could range up to several centimeters.

We also demonstrated that the TRIFT instrument is capable of doing large-area MALDI-TOF experiments at high ( $>1000$  Hz) laser repetition rates. Three different acquisition modes each have their own advantages. The microscope images give a high-spatial resolution image. The signal that is recorded with an ADC gives the

corresponding mass spectrum. And the data that is recorded with the TRIFT electronics, using a TDC, can be directly viewed in WinCadence during the acquisition and be used for quick access to tune blankers as well as other system parameters.

A TDC acquisition system was also shown to be useful for low-mass MALDI experiments at high laser rep-rate. For MALDI experiments of lower concentration compounds and compounds with higher mass, the use of an ADC as means of detection is clearly preferred. When using an ADC, the peak intensity is best preserved and therefore the high ion loads that are typical for MALDI-MS can be fully used for analysis. Because of limitations inherent to ion counting techniques, this is not possible with a TDC. We showed that an ADC with averaging capabilities is necessary for high-speed large area acquisitions as it gives a large reduction in both data writing time and data file size.

The possibility to combine microprobe and microscope mode imaging offers possibilities to recognize spatial details that cannot otherwise be resolved.

## 5 $C_{60}^+$ SECONDARY ION MICROSCOPY USING A DELAY LINE DETECTOR

This chapter is based on:

Klerk, L.A.; Lockyer, N.P.; Kharchenko, A, MacAleese, L.; Dankers, P.Y.W., Vickerman, J.C.; Heeren, R.M.A., *Analytical Chemistry*, Submitted.

---

Buckminsterfullerene ( $C_{60}$ ) as a primary ion for secondary ion mass spectrometry (SIMS) has shown many benefits over classical SIMS sources in the analysis of large organic molecules including many of biological significance. One constraint has been the limited focusing capabilities of the  $C_{60}^+$  beam. Although this could be circumvented by using beam size limiting apertures at the cost of beam current, high resolution imaging using conventional time-of-flight (TOF) instruments has been challenging and time-consuming. We present a method in which we combine the use of an unfocussed  $C_{60}^+$  beam with an ion optical microscope. A delay line detector is used to obtain fully resolved hyperspectral datasets that contain both the full mass spectral and the localization information. The obtained image resolving power is 4  $\mu\text{m}$  at a pixel size of 250 nm. Microscope mode  $C_{60}^+$  imaging was shown to resolve micrometer-scale features in a combined polymer/tissue sample. Our new approach demonstrates high quality SIMS imaging using the full  $C_{60}^+$  beam current. This results in equal or better resolving power at reduced acquisition speed.

---

## 5.1 Introduction

Time-of-flight secondary ion mass spectrometry (TOF-SIMS) is a powerful tool for the chemical analysis of surfaces. It offers high-resolution imaging and mass spectral information about the molecular composition of biological and synthetic samples<sup>9</sup>. In SIMS, secondary ions are generated under the impact of high-energy primary ions ( $\text{Ga}^+$ ,  $\text{Au}_n^+$ ,  $\text{Bi}_n^+$ ,  $\text{C}_{60}^+$ , *etc*) in a process known as sputtering. The sputter yield is the number of sputtered molecules, atoms or ions per primary ion impact. In order to solve biological questions at the cellular length-scale using SIMS imaging, there is a tendency towards higher spatial resolution. Although matrix assisted laser desorption and ionization (MALDI) MS can be used for mass spectral imaging analysis<sup>192, 193</sup>, SIMS is the favoured technique in certain cases, especially when studying lipids and small molecules (< 2000 Da) at the cellular length scale (<20  $\mu\text{m}$ ). Besides vacuum compatibility, SIMS does not require any sample treatment before analysis and therefore has no related spatial resolution constraints *e.g.* the crystal size for matrix coating in case of MALDI. Furthermore, SIMS has a negligible sample consumption due to its high surface-sensitivity<sup>40, 44, 200</sup>. Therefore samples can be re-measured using complementary imaging techniques like MALDI MS imaging<sup>201</sup>.

One of the challenges that have to be met in (bio)molecular SIMS imaging is the sensitivity issue. The number of diagnostic sputtered molecular ions that can be generated from a certain surface area typically limits image quality. The introduction of cluster primary ions has been a big step towards increasing sensitivity in SIMS. Cluster ion sputtering was first introduced by Anderson and Bay<sup>202</sup> and later, by Appelhans and Delmore for SIMS<sup>13</sup>. An important property of cluster ion sputtering is the non-linear increase in sputter yield with cluster nuclearity ( $n$ )<sup>203</sup>. The most popular currently used cluster primary ions are  $\text{Au}_3^{+204}$ ,  $\text{Bi}_3^{+205}$  and  $\text{C}_{60}^{+20, 206}$ .

A major reason that cluster ions show increased sputter yield lies in their fragmentation at the surface. Due to this fragmentation, the total energy of the primary particle is divided over the fragments and deposited at a shallower depth compared to atomic ions of the same velocity. The greater energy density in the surface region results in increased sputtering, particularly for larger molecular species due to co-operative uplifting effects<sup>15</sup>. For example, secondary ion yield is increased by up to three orders of magnitude for  $\text{C}_{60}^+$  compared to  $\text{Ga}^+$  primary ions, especially for the mass range  $m/z$  200-2000<sup>23, 24, 204, 207-209</sup>. This increase in secondary ion yield means that the detection limit is improved accordingly. In addition to sputtering events the impact of the primary ion initiates chemical damage *e.g.* bond



breaking in the vicinity of the impact zone. For ‘polyatomic’ clusters *e.g.*  $C_{60}^+$  the kinetic energy is effectively confined to the surface layers (<10 nm) of the sample, from which sputtering occurs. Smaller clusters *e.g.*  $Au_3$ ,  $Bi_3$ , penetrate more deeply, generating chemical damage in the bulk material<sup>210, 211</sup>. A key parameter in describing the properties of a particular primary ion is the so-called ‘efficiency’. Efficiency is the ratio of sputter yield to disappearance cross-section, which itself includes a measure of the chemical damage in the impact crater<sup>212</sup>.

The efficiency gain from cluster projectiles is particularly important when doing high spatial resolution imaging, because of the low amount of material that is probed when imaging small regions. Together with the increased mass range afforded by cluster projectiles, this offers new possibilities for the SIMS imaging at high resolution of complex molecular systems including biological tissue samples. The extremely low residual sub-surface chemical damage under polyatomic sputtering means that the generation of diagnostic secondary ions is sustained under prolonged bombardment. Specifically, chemical analysis is possible beyond the traditional ‘static limit’ (1% of the surface impacted), the point at which increased fluence of atomic or small cluster projectiles produce mass spectra characteristic of the chemical damage<sup>211, 213</sup>. In contrast, the higher efficiency of polyatomic primary ions leads to the important capability of molecular depth profiling and 3D imaging. An in-depth discussion on this subject is given in a recent review by Fletcher et al<sup>214</sup>.

Despite polyatomic projectiles such as  $C_{60}$  having the highest efficiency, the current state-of-the-art in terms of spatial resolution for ToF-SIMS is of the order 100 nm, using clusters such as  $Au_3^+$  or  $Bi_3^+$ <sup>209, 215</sup>. This is because these ions are rather easily produced with high flux density in liquid metal ion guns (LMIGs).

Where the analytes are present as minor components or have low secondary ion yield, the application of especially high efficiency polyatomic ions *e.g.*  $C_{60}$  becomes particularly attractive. This situation is likely to be the case in increasing numbers of applications, for example the localisation of drugs and metabolites at (sub)cellular dimensions in tissue and cell cultures. Therefore the remainder of this manuscript is concerned with the development of methodologies for  $C_{60}$  SIMS imaging, leading to improved performance against a number of criteria including quality of data and speed of acquisition.

The major challenge in using a  $C_{60}$ -source for SIMS imaging is the limited source brightness. The electron-impact method of creating the primary ions, inherently results in a space-charge limited primary ion beam with a large diameter and relatively low ion flux density compared to liquid metal ion sources. To obtain small-diameter beam spots, apertures can be used to collimate the beam. A focal diameter, and hence pixel size, of less than 200 nm is possible with this method using

40 keV beam energy<sup>216</sup> but at the expense of the ion current, which is typically less than 0.05 pA. This low current, which is over 4 orders of magnitude lower than the 2 nA surface current that can be obtained using no apertures<sup>23</sup>, illustrates the major disadvantage of beam collimation: the tremendous loss of beam current. This dramatic decrease in ion current inevitably leads to an increase in measurement time. High-spatial resolution SIMS using a collimated  $C_{60}^+$  beam and conventional pulsed TOF acquisition is therefore very time-consuming and impractical for large areas ( $mm^2$ ). This is particularly true if the low-damage properties of  $C_{60}$  bombardment are to be exploited using a primary ion fluence beyond the static limit ( $>10^{13}$  ions  $cm^{-2}$ ).

One approach, which is currently being pioneered to obtain high spatial resolution SIMS imaging at reasonable measurement timescales, is to decouple the bombardment process from the time-of-flight measurement, allowing a nearly continuous ion beam to be used for TOF-SIMS measurements<sup>5,6</sup>. Another approach is to circumvent the limitations that are connected with the limited focussing capabilities of  $C_{60}$  primary ion sources. To get around these limitations, the imaging resolution needs to be independent of the  $C_{60}$  probe size. This independence can be achieved using stigmatic ion microscopy<sup>71, 105-107</sup>. In this technique, the localization of the ions generated at the sample surface is retained through the spectrometer and detected using a position sensitive detector. Until very recently, this technique was limited to two modes of operation. Either a full image of one (or a few) selected ions was recorded, in which the other ions that are generated at the surface are blanked by electrostatic deflectors. Alternatively the full mass spectrum was recorded in combination with a total ion current (TIC) image. Although this has proven to be a powerful tool in unravelling small spatial features<sup>71</sup>, full spectral and spatial detail could never be recorded simultaneously.

The introduction of a delay line detector for SIMS has circumvented this issue<sup>217</sup>. A delay line detector, which was first developed for photoemission electron microscopy<sup>218</sup>, can detect both temporal and spatial information at the same time. Consequently, a full hyperspectral datacube, that contains both time-of-flight and spatial information for each ion, can be measured at once. In this paper we show that high resolution  $C_{60}^+$  SIMS imaging is possible at much faster rates by combining the microscope approach with a delay line detector. Because the image quality is completely independent of the source design, it is expected that a similar image quality as that shown here for  $C_{60}$  will be achievable with any other pulsed ionization source, e.g.  $Au_{400}$ <sup>28</sup> or MALDI<sup>107</sup>.

## 5.2 *Experimental*

### 5.2.1 **Mass microscopy**

The SIMS experiments were carried out using a TRIFT II (triple focusing time-of-flight) mass spectrometer (Physical Electronics, Eden Prairie, MN). The ion optical design of this instrument is such, that the spatial origin of the measured ions is retained through the spectrometer flight path<sup>105, 106</sup>. The ions that hit the detector are therefore a direct (magnified) projection of the sample. The spectrometer and the triggering of the primary ion source and the delay line detector acquisition system were controlled using WinCadence version 4.4 (Physical Electronics, Eden Prairie, MN) and TRIFT electronics. A sample potential of 3 kV and a post-acceleration voltage of 6 kV were used, resulting in a total secondary ion energy of 9 keV. A 9 keV secondary ion energy provides ~70% detection efficiency of ions of 2 kDa<sup>219</sup>, and has been shown sufficient for detecting quasi-molecular ions of phospholipids in the 500-1000 Da range.

### 5.2.2 **Mass spectrometric imaging in microprobe mode**

For a proper assessment of the mass spectrometric microscope mode imaging data, comparative measurements were performed on a microprobe mode operated SIMS instrument. These experiments were done on a custom-built BioTOF-SIMS instrument (designed in a joint project between The University of Manchester, Penn State University and Kore Technology, Cambridge, UK) equipped with the C<sub>60</sub> source described below. Mass analysis is performed in reflectron mode using delayed ion extraction to improve mass resolution. Secondary ions are detected using a dual microchannel plate assembly (Photonis USA Inc., MA) operating with ~20 kV post-acceleration voltage, interfaced to 1 ns TDC (Fast Comtec GmbH). The use of a 20 kV post-acceleration voltage implies that ~100% secondary ion detection should be expected for this instrument over the mass range of interest<sup>219</sup>.

### 5.2.3 **C<sub>60</sub> primary ion gun**

SIMS was performed using a 20 kV C<sub>60</sub> ion source (IOG-C60-20, Ionoptika Ltd, UK). This ion source was mounted on the TRIFT in place of the Cs<sup>+</sup> source at an angle of 42° with respect to the sample normal. On the BioTOF-SIMS instrument the C<sub>60</sub> source is mounted 40° with respect to the sample normal. Therefore, primary ion beam shadowing effects are comparable. Beam shadowing effects on the determined resolving power value are further eliminated by using the grid, which lays on top, and therefore does not suffer from shadowing effects. C<sub>60</sub><sup>+</sup> ion selection is performed using a Wien filter. All experiments described in this paper were performed using

$C_{60}^+$  primary ions. The DC current at the sample surface was typically 100 pA at a beam spot diameter at the surface of  $\sim 250 \mu\text{m}$  for microscope mode experiments and 15 pA with a beam spot diameter at the surface of  $\sim 8 \mu\text{m}$  for microprobe mode experiments. A  $100 \mu\text{m}$  aperture was used for beam collimation in microprobe mode only, as this is not necessary in microscope mode when position sensitive detection is possible. The primary ion beam diameter at the sample surface was set at  $250 \mu\text{m}$  for microscope mode experiments by defocusing the beam, using the single electrostatic lens in the  $C_{60}$  ion column.

### 5.2.4 Delay line detector

A chevron-stacked dual microchannel plate (DMCP) with  $12.5 \mu\text{m}$  pore size was used in combination with a hexanode 2 dimensional delay line detector (Roentdek GmbH, Frankfurt, Germany) for position sensitive detection<sup>218, 220</sup>. The advantage of using three delay lines (hexanode) instead of two (x-y configuration) is the measurement redundancy. This redundancy minimizes the dead area of the detector after each ion hit<sup>221</sup>, which is a result of the detection system's dead time. Signal from this detector is measured from each end of each of the three delay lines and from the backside of the DMCP, giving seven individual signals. The signals are amplified and converted into NIM (Nuclear Instrumentation Module) standard pulses using an ATR19-8 amplifier/constant fraction discriminator (CFD) (Roentdek GmbH, Frankfurt, Germany). A TDC8HP time to digital converter (TDC) PCI-card (Roentdek GmbH, Frankfurt, Germany) is used to feed the signal into a computer with a time resolution of 25 ps. The TRIFT instrument's main trigger is used to start the TDC acquisition. The TDC signal is acquired using Cobold software version 2002 or 2008 (Roentdek GmbH, Frankfurt, Germany). The DMCP signal is used as a time reference signal for each ion hit. The location at which the ion hits the detector is derived from the pulse that is detected at each end of each of the delay lines. Based on the difference between the arrival times of the pulses on each end of a line, the location of the ion hit can be determined. Three delay lines and the DMCP signal are used to redundantly determine two spatial dimensions and the secondary ion arrival time relative to the pulsing moment of the primary ion beam. Because seven signals can be measured per ion and each ion has only three parameters (position X, Y and arrival time), overlap of signals within the electronics dead time in the detection channels can be compensated for by a reconstruction algorithm.

In-house built software was used for further analysis and visualization of the data. Data read-in routines were made using Roentdek library functions. A home-built program tailored to mass spectrometric data was made for data processing, analysis and visualization. The dataset of time-resolved hits is resolved in space and further

processed as a 2D grayscale image. The software helps to fix TDC-related errors ("cross-talks") by re-ordering the measured hits, based on the known arrival time-sums<sup>221</sup>. After this basic reconstruction, resulting images suffer from 3 types of artifacts: (1) CFD-related artifacts (so called "ringing"), (2) ion optics related distortions observable as dimensional anisotropy and (3) blur related to inevitable deflection in electron showers leaving the MCP. The first artifact is hardware-related so the best solution to this would be improvement of the hardware. Also optimization of the reconstruction algorithm that is part of the manufacturer's software is expected to improve this. The blurring and partially ion optical distortion can be further addressed with 2-dimensional image reconstruction methods, which is beyond the scope of this paper.

### 5.2.5 Colored TEM grids

A nickel hexagonal thin bar grid (700 mesh) (Agar scientific, G2760N) for transmission electron microscopy (TEM) was coloured green using a permanent marker pen (Staedtler Lumocolor 318-5). This organic dye gives strong signals at  $m/z$  97 and  $m/z$  500-501 in the negative SIMS mode and at  $m/z$  358 in the positive SIMS mode. The grid was overlain on an indium tin oxide (ITO) coated glass slide with a sputter coated 1 nm layer of gold (using a Quorum Technologies SC7640 sputter coater). Silver paint (Agar G302 quick drying silver paint, Agar Scientific Ltd., Essex, U.K.) was used to stick the grid to the surface.

### 5.2.6 Imaging of a hybrid polymer-tissue sample

Polymer-tissue samples of hydrogels implanted under the capsule of a rat kidney were kindly provided by Eliane R. Popa (UMCG, Groningen, The Netherlands). The hydrogels were composed of supramolecular ureido-pyrimidinone (UPy)<sup>222</sup> modified polymers in 0.9% NaCl. These supramolecular polymers were synthesized in a similar manner as described before for thermoplastic elastomers<sup>223</sup>. They consist of poly(ethylene glycol) ( $M_n = 6000$  g/mole) and polycaprolactone ( $M_n = 1250$  g/mole) precursor polymers in a 9:1 w/w% ratio chain-extended with a UPy-moiety. These UPy-groups form cross-links between polymer chains through quadruple hydrogen bonding and allow supramolecular binding of functional additives<sup>224</sup>. 10  $\mu\text{m}$  cryo-sections of the polymer-tissue samples were made using a Leica CM1900 cryo-microtome at  $-20^\circ\text{C}$  and thaw-mounted on indium tin oxide (ITO) coated glass slides (Delta technologies Ltd, Stillwater, Mn, USA). Sections were stored at  $-80^\circ\text{C}$  until analysis. The sample was brought to room temperature under dry conditions in a vacuum desiccator and introduced into the TRIFT instrument without further treatment.

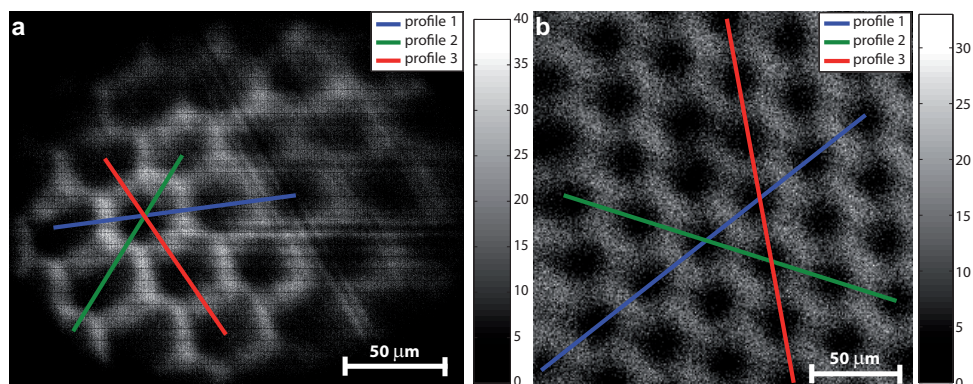


**Figure 5.1** Selected ion count images of a hexagonal TEM grid covered with an organic dye. The images represent the intensity distribution of the peak at  $m/z$  97 resulting from the dye molecule. Image a shows the result from microscope mode imaging, image b shows the result from microprobe mode imaging. The blue, green and red lines indicate the line profiles that were made through the image for determining the resolving power (see figure 5.2, table 5.1 and table 5.3).

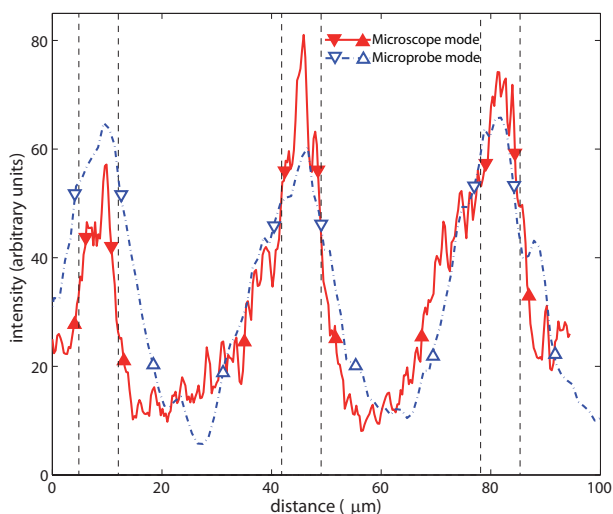


**Figure 5.2** Line-profiles along profile 2 of the microscope mode measured dataset (indicated as green line in figure 5.1a; red, solid line in this figure) and line-profile along profile 1 of the microprobe mode measured dataset (indicated in as blue line in figure 5.1b; blue, dot-dashed line in this figure). The profiles are based on a 3 point sum orthogonal to the line. Image resolving power was determined using the 20%/80% method. This indicates a resolving power of  $4 \mu\text{m}$  for microscope mode and  $7 \mu\text{m}$  for the microprobe mode. 80% of maximum points are indicated with a  $\blacktriangledown / \blacktriangledown$ , 20% of maximum value is indicated with  $\blacktriangle / \blacktriangle$ , for microscope/microprobe mode. The dashed vertical lines show the theoretical width of the grid bars. The grid bars are positioned based on the center between the two 80% of maximum points of the microscope mode dataset. Line plots are scaled to equal integral for both profiles.

## 5.3 Results

### 5.3.1 Comparison of image quality between microscope and microprobe modes

The image quality was determined using the TEM grid sample. Two methods were used. Both the sharpness of the edge of a feature and the size of the grid-bar were assessed. The sharpness of the edge determines the resolving power. In addition, the feature size of a grid bar in the MS image was compared with its actual size, specified by the supplier. These values were determined for both the microscope mode delay line detector data and the microprobe mode data. The green colored grid was measured using similar acquisition times for both experiments ( $\sim 20$  minutes). The primary ion current for a DC beam was  $\sim 100$  pA in microscope mode and  $\sim 15$  pA in microprobe mode. A selected ion count (SIC) image was created at  $m/z$  97. From a standard, it was confirmed that this peak results from the green dye, and hence localized on the grid. The resolving power was measured using custom built routines in MatLab (version 7.0.4, R14, SP2, The MathWorks, Natick, MA). The pixel size in the image used was 250 nm for the delay line detector (figure 5.1 a) and 1  $\mu\text{m}$  of the microprobe mode measured data (figure 5.1 b). We explicitly chose to determine the resolving power as a benchmark value rather than assessing the image resolution based on the pixel size. In the case of a microscope mode experiment, the pixel size depends on the data processing techniques and deconvolution mechanisms that are used to convert the delay line time-resolved data into an image. This is not the limiting step, and moreover of little value when image analysis is concerned. In the case of a microprobe mode experiment, the pixel size depends on the step-size of the ion beam rastering, which can be much smaller than the focus of the primary ion beam and is therefore not a good parameter to determine image quality.

To measure the resolving power, we made line profiles through the image, adding up 3 neighbouring pixels in the direction orthogonal to the profile. These curves were smoothed using nearest-neighbour averaging over 3 points. The resulting line profiles were plotted (figure 5.2) and the image resolving power was determined using the criteria of an 80% to 20% drop in intensity at the feature edge (table 5.1). Percentages were based on the difference between the maximum and the minimum of the intensities at the assessed edge. Because the sharpness of the edge does not only depend on the MS experiment but also on the quality of the sample, which is influenced by sample preparation issues, the worst value was disregarded for each line profile. This resulted in a resolving power of 7.0  $\mu\text{m}$  for the microprobe experiment with a pixel size of 1.25  $\mu\text{m}$  and 4.3  $\mu\text{m}$  with a pixel size of 0.25  $\mu\text{m}$  for the microscope experiment.

The improvement of image quality in microscope mode SIMS was further confirmed by comparing the actual size of a feature with the apparent size from the MS image. This was measured by comparing the actual thickness of a grid bar (8  $\mu\text{m}$ , according to data given by supplier) with the full width at half maximum (FWHM) thickness determined from the MS images. This gave an overestimation of 111% (9.66  $\mu\text{m}$ ) for the microprobe experiment and 48% (4.65  $\mu\text{m}$ ) for the microscope experiment (table 5.2).

**Table 5.1** Average values and errors assessing the sharpness of the edges for a microprobe (BioTOF) and microscope (TRIFT-DLD) SIMS imaging experiment. The highest value for each line was discarded.

direction	BioTOF		TRIFT with Delay Line	
	Average ( $\mu\text{m}$ )	standard deviation ( $\mu\text{m}$ )	Average ( $\mu\text{m}$ )	standard deviation ( $\mu\text{m}$ )
1	6.92	1.63	4.61	1.23
2	8.20	2.02	3.50	2.20
3	5.86	2.21	4.79	0.42
all directions	7.03	2.36	4.30	1.56

**Table 5.2** Deviation of full width at half maximum of the grid bar-width on the MS images compared with the real value.

direction	BioTOF		TRIFT with Delay Line	
	Average ( $\mu\text{m}$ )	standard deviation ( $\mu\text{m}$ )	Average ( $\mu\text{m}$ )	standard deviation ( $\mu\text{m}$ )
1	8.18	0.90	4.69	0.28
2	11.27	2.34	1.89	3.20
3	9.52	0.94	7.36	0.54
all directions	9.66	3.47	4.65	2.62
relative overestimation	111%	48%	48%	36%

### 5.3.2 Comparison of spectral quality between microscope and microprobe modes

To give a complete indication of the data acquisition quality, in addition to image quality, spectral quality needs to be assessed. Total image spectra were made to show the type of spectra that result from both methods (figure 5.3). Both spectra are recorded from the DMCP of the respective instrument. It is clear that similar



spectral quality is obtained, which supports the validity of comparison that is made between the two different systems.

To make a fair and quantitative comparison, apart from the image quality assessment, the spectral signal/noise ratios (S/N) was determined for equal acquisition times. The S/N values were determined for the total image area spectrum, an equally sized region of interest spectrum, and a single-pixel spectrum (table 5.3). The spectra used were binned to 0.1  $m/z$  units. This leads to a certain background value, which would in theory be close to zero for time-count data, as can be seen from the single-pixel spectrum background (see caption of table 5.3). For the same primary ion pulse width (100 ns) the delay line detector shows a higher S/N in all cases.

To assess spectral quality, a comparison is made between the two techniques, based on their respective mass resolution ( $M/\Delta M$  at full width at half of the maximum value (FWHM) of the peak). The inset in figure 5.3 shows a slightly higher mass resolution power for the BioTOF. This is confirmed by the values calculated for the three different areas (table 5.3). For a single-pixel spectrum, the mass resolution is however higher for the microscope imaging mode but it has to be noted that under the low-count conditions typical for single-pixel spectra, it is difficult to reliably determine the spectral quality.

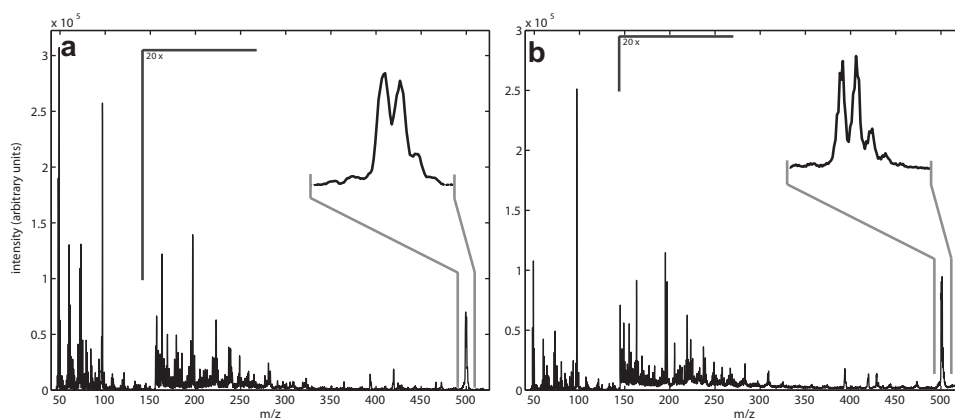


**Figure 5.3** Summed TOF-SIMS spectra from the imaging datasets. Panel a shows the spectrum from the microscope experiment (image in figure 5.1 a), panel b shows the spectrum from the microprobe experiment (image in figure 5.1 b). The part of the mass spectrum above  $m/z$  150 Da is shown with a magnification of 20x, the insert shows the peaks at  $m/z$  500-502, with slightly higher resolving power for the microprobe experiment.

**Table 5.3** Evaluative data on the spectral quality. All values were determined in the  $m/z$  90-110 range of the same negative ion mode SIMS dataset that was used for determining the image resolving power, using the highest peak ( $m/z$  97). Three separate assessments were made, using the summed spectrum of the total image, the summed spectrum of a region of interest (ROI) encompassing one grid unit including its edges, and the spectrum of one single pixel (the highest total ion count pixel in the image). Baseline value was determined as the lowest value in the  $m/z$  90-110 range. \*Lowest values in range for the single pixels spectra were zero because of the low total number of counts, they were set at 1 because random noise counts did occur in the assessed mass range.

Determined value	Detection	max	baseline	FWHM	S/N	Resolution (M/ $\Delta$ M at FWHM)
Total image spectrum	Delay Line					
	Detector	2.55E+05	232	0.4	1099	243
ROI of one grid unit	BioTOF	2.51E+05	483	0.21	520	462
	Delay Line					
Single pixel spectrum	Detector	2.81E+04	22	0.4	1276	243
	BioTOF	1.83E+04	27	0.19	680	511
Single pixel spectrum	Delay Line					
	Detector	19	1*	0.21	19	463
	BioTOF	14	1*	0.3	14	323

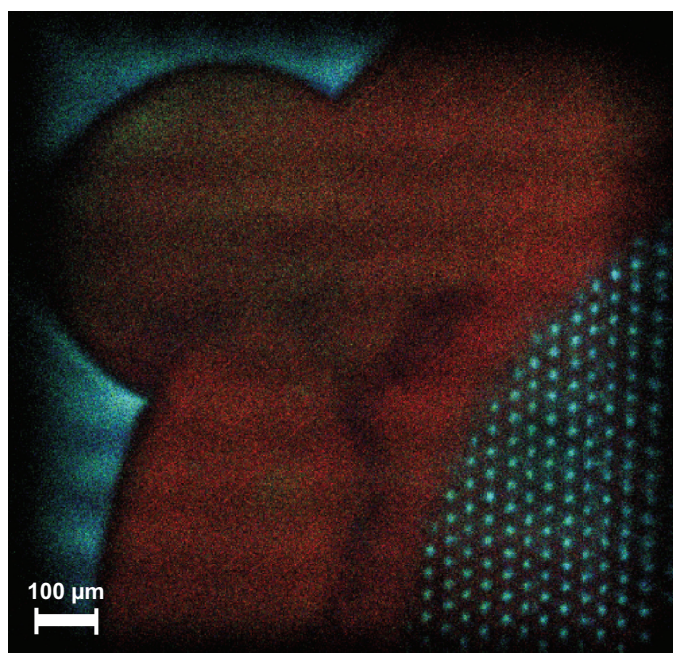


**Figure 5.4** Large area image of the edge of a TEM grid covered with green dye. The image was acquired in the positive ion SIMS microscope mode using stage rastering. It is built up from 8 images in X-direction and 8 images in Y-direction. Each tile was measured for 60 seconds, giving a total acquisition time of 64 minutes. The green dye is shown in red (peak at  $m/z$  481), green indicates  $\text{Na}^+$ , blue indicates  $\text{K}^+$ .  $\text{Na}^+$  and  $\text{K}^+$  concentrate at the substrate so they are seen through the grid. Because of the low number of counts per

pixel at this high resolution, the intensity range was kept such that intensities with a presence of less than 1/1000 of the surface were given the maximum intensity scale value, thus topping off the dynamic range. This results in intensity values of 8 counts/pixel (for the green dye, maximum intensity was 15), 6 (for  $\text{Na}^+$ , maximum intensity was 17) and 6 (for  $\text{K}^+$ , maximum intensity was 16).

### 5.3.3 Large area imaging

Obviously, high resolution imaging is favoured but should not compromise the field of view of the experiment. Therefore, data acquisition automation is important to make high-resolution imaging possible even for large areas. For this purpose, stage rastering was performed using the mosaic mode in WinCadence<sup>225</sup>. This makes the imaging of large areas at high spatial resolution possible by generating a mosaic of microscope experiments. Figure 5.4 shows the overlay of three selected peaks in a dataset measured using mosaic mode. An 8x8 mosaic was made using 60 seconds exposure per position. The mosaic step size was 120  $\mu\text{m}$  and the field of view at each position a circular area of about 200  $\mu\text{m}$  diameter. Large area imaging in high resolution is shown to be possible at a relatively short measurement time. Technically, the resolving power is the same as in a single-tile experiment, but in practice it is limited by the contrast in the image due to the limited number of counts.

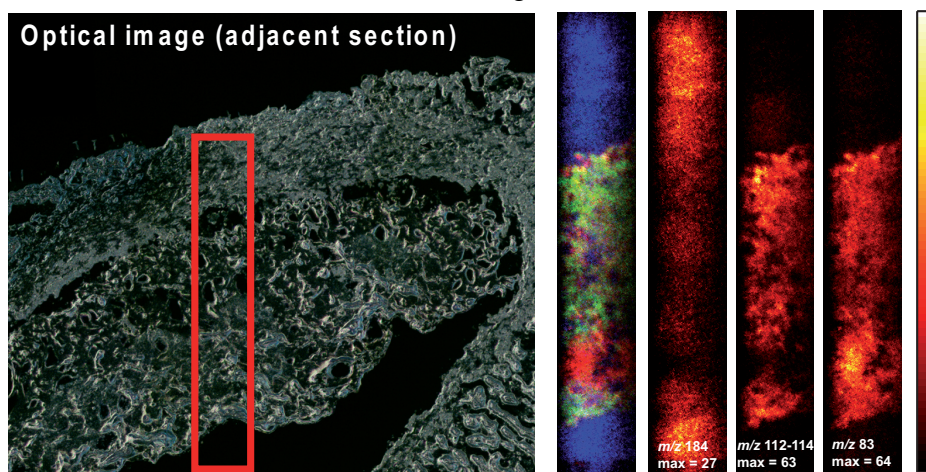


**Figure 5.5** Selected ion count images of polymer hydrogel implanted under the renal capsule. The images are built up of 16 overlapping datasets. MS images are 150  $\mu\text{m}$  wide. Left image is an optical image of an adjacent section with the area of measurement marked with a red square. The three rightmost images show (left to right): phosphocholine ( $m/z$  184), which shows high abundance in the surrounding tissue as well as enhanced signal at the substrate (arguably due to ionization enhancement) and two different distributions from the polymer region. A contrast enhanced RGB overlay is given in the middle of the figure, showing red ( $m/z$  83, max value set to 12), green ( $m/z$  112-114, max value set at 35) and blue ( $m/z$  83, max. value set at 35).

### 5.3.4 On-tissue imaging

The applicability of the technique in the biomedical field was evaluated on a tissue section of a rat kidney containing a polymer hydrogel under the renal capsule. Series

of 17 single measurements were performed using 120  $\mu\text{m}$  intervals with an acquisition of 5 minutes per position. Single position datasets were composed manually using custom written MatLab routines. This resulted in an 800x150  $\mu\text{m}$  total image (figure 5.5). This 70-minute measurement shows high-resolution localization of several organic components.

#### 5.4 *Discussion and conclusions*

For the first time, we showed full exploitation of the delay line detector (DLD) for imaging mass spectrometry. Full-mass range stigmatic ion microscopy was shown to be possible for secondary ion mass spectrometry (SIMS) using a buckminsterfullerene ( $\text{C}_{60}$ ) primary ion source. The advantage of using ion microscope mode mass spectrometric imaging rather than the commonly used microprobe technique is the independence of the primary beam focus. We showed an average resolving power of 4  $\mu\text{m}$ , which, at this acquisition speed, is high compared to microprobe  $\text{C}_{60}$  SIMS experiments. The current limitation of the resolving power is a convolution of ion optical tuning, sample-related aberrations (like ion-beam shadowing effects), detector hardware optimization and reconstruction efficiency of the delay line data. Although this type of resolving power is possible by using apertures and focussing the primary beam to an equally sized probe size, this range of resolution would lead to impractical acquisition times due to limited focussing possibilities of the primary beam. Our comparative experiment, using equal measurement times and the same  $\text{C}_{60}$ -source on a microprobe mode instrument, showed that the image resolving power in microscope mode is two times better than in microprobe mode. This offers great opportunities in the field of biological tissue analysis at the cellular length scale, as is shown in a measured tissue example.

One should note that both in the ion source design and in the delay line design, developments are still on-going to improve image resolution and acquisition speed. The use of a higher energy (40 keV), two lens-system can improve the focussing and ion-flux of a primary  $\text{C}_{60}$  beam<sup>216</sup>. As alluded to above, mass spectrometer design can be modified to use dc ion beams in the microprobe mode that enable fast data acquisition even for low-current primary beams<sup>5,6</sup>.

Improved ion optics, further DLD hardware optimization and improved data acquisition and reconstruction can still improve the resolving power obtained with a DLD. The great advantage of position sensitive detection is the total independence of the ion source focus, which means that any other pulsed ion source can be used for high-resolution imaging without requirements with respect to their focus.

## 6 DATA ANALYSIS STRATEGIES IN IMAGING MASS SPECTROMETRY

This chapter is based on:

Klerk, L. A.; Broersen, A.; Fletcher, I.W.; van Liere, R.; Heeren, R. M. A. *International Journal of Mass Spectrometry* **2007**, *260*, 222-236.

---

The large size of the hyperspectral datasets that are produced with modern mass spectrometric imaging techniques makes it difficult to analyze the results. Unsupervised statistical techniques are needed to extract relevant information from these datasets and reduce the data into a surveyable overview. Multivariate statistics are commonly used for this purpose. Computational power and computer memory limit the resolution at which the datasets can be analyzed with these techniques. We introduce the use of a data format capable of efficiently storing sparse datasets for multivariate analysis. This format is more memory-efficient and therefore it increases the possible resolution together with a decrease of computation time. Three multivariate techniques are compared for both sparse-type data and non-sparse data acquired in two different imaging TOF-SIMS experiments and one LDI-TOF imaging experiment. There is no significant qualitative difference in the use of different data formats for the same multivariate algorithms. All evaluated multivariate techniques could be applied on both SIMS and the LDI imaging datasets. Principal component analysis is shown to be the fastest choice; however a small increase of computation time using a VARIMAX optimization increases the decomposition quality significantly. PARAFAC analysis is shown to be very effective in separating different chemical components but the calculations take a significant amount of time, limiting its use as a routine technique. An effective visualization of the results of the multivariate analysis is as important for the analyst as the computational issues. For this reason, a new technique for visualization is presented, combining both spectral loadings and spatial scores into one three-dimensional view on the complete datacube.

---

## 6.1 Introduction

With the recording of large amounts of data, data analysis gets increasingly complicated. This is a general trend that goes hand in hand with the development of spectroscopic imaging techniques. More sophisticated analytical imaging techniques offer many novel possibilities for the analysis of complex systems in chemistry, biology, physics, engineering and geology. Applications range from airborne or satellite analysis of features in large land zones for agriculture<sup>226</sup>, climate research<sup>227</sup> and military<sup>228</sup>, to various microspectroscopic techniques, including imaging Fourier transformed infrared spectroscopy (FTIR)<sup>128, 131, 229</sup>, RAMAN spectroscopy imaging<sup>230</sup> and mass spectrometric imaging (MS imaging)<sup>195, 231, 232</sup>. All these techniques face similar data processing and interpretation challenges.

These techniques result in hyperspectral imaging datasets that typically contain anywhere between a few tens and a few millions of spectral variables for each image pixel. As technological developments proceed, spectroscopic imaging gets possible at higher spatial resolution, shorter acquisition times, larger surfaces and higher spectral resolution. Further sophistication of the measurement techniques and instrumental design has made various imaging techniques more accessible for the routine user.

Because of the large amount of data that is produced with microspectroscopic techniques, data analysis can get very complicated and automated data mining techniques are required. In many cases, the measurement is not the most time-consuming part, but post-acquisition analysis becomes more elaborate due to the large amount of data obtained. Nevertheless, one would like to be able to efficiently analyze all acquired data and both get a complete overview of the data and find trace features. Moreover, when a comparison between different samples needs to be made, computational routines would speed up the search for corresponding spectral and spatial patterns. In order to match material-specific spectral or spatial patterns between different datasets, they need to be decomposed into profiles that are specific for the various chemical components. Multivariate analysis techniques can be used for this purpose. Once the data is decomposed into components that each represent one specific combination of properties (e.g. a compound-specific spectrum), also database-matching is possible.

Multivariate statistical methods, and especially principal component analysis (PCA), are established ways to efficiently extract information from large multidimensional datasets<sup>233</sup> (also see section 2.8 of this thesis). Combined with different preprocessing and visualization methods, they form a powerful analytical tool for the analysis of hyperspectral datasets. Using these techniques, chemically relevant

spectral features can be extracted from large datasets. Most of the current multivariate analysis methods however still require a considerable amount of operator input<sup>145</sup>.

One of the fields of science, in which data complexity is becoming an increasing problem, is MS imaging. MS imaging is becoming an indispensable analytical tool in many different disciplines, such as organic geochemistry, plant sciences, polymer research, biology, biomedical sciences and proteomics. This broad applicability is the driving force behind the numerous instrumental developments that are underlying the current data-explosion. A typical MS imaging measurement results in a three-dimensional datacube, containing a position on the sample and a mass spectrum. Different cross-sections of this cube give either mass specific images or location-specific mass spectra. To make these cross-sections, either spectral or spatial features need to be known in advance, or extracted from the datacube. However, when one relies on pre-existing knowledge, it is very probable that certain features are not remarked. This is what multivariate statistics could be helpful with. Various multivariate statistical methods are currently being used to computationally extract features from imaging time-of-flight secondary ion mass spectrometry (TOF-SIMS) datasets<sup>143, 147, 234</sup> and matrix assisted laser desorption/ionization time-of-flight (MALDI-TOF) imaging<sup>235</sup>. TOF-SIMS measurements result in a microscopic image of a sample surface of which every single pixel comprises a full mass spectrum. Thus, an image can be created for each mass-number. The resulting intensity-map is usually visualized using a pseudo-color map. The number of measured points in a full datacube makes it impossible to be processed at the highest possible resolution with the computers that are currently readily available. A full data-matrix using 2 000 000 channel numbers (a common measurement unit for flight-time in TOF measurements) and a 256×256 pixels image would result in a matrix containing over 131 billion datapoints, mainly containing zeros. Storing these datasets in such a way that zero values are left out is possible when a matrix format is used that only stores the nonzero values. For highly sparse data, this sparse-type matrix storage reduces the amount of memory needed when the data is processed and thus yields a much more efficient memory use. The same holds for MALDI-TOF imaging data, which can be processed in a similar way.

Due to the computational constraints that are encountered when MS imaging datasets are analyzed, multivariate decomposition methods have only been reported to be executed on either peak-selected datasets (using nominal masses) or on highly binned datasets (typical bin-sizes of not less than  $m/z= 0.5$ ). Only selected parts of the datasets were analyzed using full available resolution<sup>108, 234</sup>, which did indeed result in increased chemical resolving power.

The increase of computer power, as well as the availability of eigenvalue-analysis methods suited for large datasets that are stored using a sparse-type matrix, expands the possibilities to perform multivariate statistics at much higher (spectral) resolution. In this paper we evaluate different current multivariate analysis methods applied on TOF-SIMS and laser desorption/ionization time-of-flight (LDI –TOF) imaging datasets. Standard PCA as carried out on full matrices, as well as a MatLab™ implementation for PCA on sparse matrixes are evaluated. These two PCA methods were combined with an optimization method using VARIMAX (Variance Maximization) rotation. A comparison was made with PARAFAC (Parallel Factors analysis)-analyzed data, which is a completely different multivariate analysis method. Eventually, the usefulness of these different multivariate methods is evaluated by a quantitative comparison of computation time using different datacube-sizes. This comparison will give an indication on the applicability of these multivariate techniques as a routine data-processing method in analytical laboratories. A well-chosen, fast, yet accurate method could eventually find its way as a widely used technique in proteomics, medicine, polymer analysis, various industries and science, opening many possibilities in molecular microscopy.

## **6.2 Experimental**

Evaluation of the different multivariate techniques was performed on two TOF-SIMS imaging datasets and one LDI-TOF imaging dataset. All samples were analyzed in the microprobe mode. The acquired data was subsequently imported and processed using MatLab-routines.

### **6.2.1 Sample preparation**

Two samples were studied for this paper using TOF-SIMS imaging: a purely synthetic sample containing well-defined chemical components and an embedded hair cross-section. One sample was measured using LDI-TOF imaging: a cross-section of paint layers.

A droplet-array of a 1% polyvinylpyrrolidone (PVP-40.000, Sigma-Aldrich) solution in water/methanol (1/1) was spotted on a polyvinylidene difluoride (PVDF) membrane (Bio-Rad Sequi-Blot PVDF Membrane for Protein sequencing, 0.2  $\mu\text{m}$ ). The spotted array was created using a CHIP-1000 Chemical Inkjet Printer (Shimadzu Biotech) at 100pL droplet volume, depositing 20 runs of 5 droplets at a time, resulting in a total droplet volume of 10 nL solution per spot. The incremental time between the 20 runs was chosen such that the droplets did not completely dry during the process. The pitch between the space-filling array of droplets was set at 250  $\mu\text{m}$ , resulting in a minimum distance between the centers of the droplets of 176  $\mu\text{m}$ . The



choice of these two well-characterized polymers offers a good reference in the comparison between different techniques.

The embedded hair cross-section was created by embedding brown Caucasian human hair in Technovit 2000LC embedding resin and light-cured for 40 minutes. The hair was embedded in as-received condition. Cross-sections were made using a glass-knife microtome cutting off 10  $\mu\text{m}$  slices until an almost longitudinal cross-section surface was obtained. The bulk block was then gold sputter-coated (1 nm) to enhance the SIMS signal<sup>117,118</sup>.

A sample of stacked paint layers was cross-sectioned with a surgical blade and subsequently gold sputter-coated (5 nm) for LDI imaging charge compensation. The sample consisted of alternating layers of two different Liquitex acrylic paints (Lefranc & Bourgeois, Le Mans, France), containing phtalocyanine blue ( $\text{C}_{32}\text{H}_{16}\text{N}_8\text{Cu}$ ) and phtalocyanine green ( $\text{C}_{32}\text{Cl}_{16}\text{N}_8\text{Cu}$ ) pigments. The alternating layers of paint had an approximate thickness of 100  $\mu\text{m}$ .

### 6.2.2 Data acquisition

The droplet-array sample was analyzed using an IonToF 'TOFSIMS IV' time-of-flight secondary ion mass spectrometer (IonToF GmbH, Germany) with a Bismuth primary ion gun, using the  $\text{Bi}_3^{2+}$  clusters. The Bi source was run in "high current bunched" mode. The primary ion energy was set at 20 keV. The primary ion current was 0.095 pA, with a pulse-width of 0.8 ns at 200 ns cycle time. The total ion dose was kept well below the static limit<sup>9</sup> (maximum dose was no more than  $10^{12}$  ions/ $\text{cm}^2$ ). The beam diameter was between 3 and 4  $\mu\text{m}$  on a sampled area of  $500 \times 500 \mu\text{m}^2$  measured at  $256 \times 256$  pixels. The analysis was done in positive ion mode. An electron flood gun was used for charge-compensation.

TOF-SIMS analysis of the cross-sectioned hair was done using a Physical Electronics (Eden Prairie, MN) TRIFT-II (triple focusing time-of-flight) TOF-SIMS, using an  $^{115}\text{In}^+$  primary ion source at 15 keV. The primary ion dose was kept well below the static limit. The sampled area was  $150 \times 150 \mu\text{m}^2$  at  $256 \times 256$  pixels. The analysis was done in positive ion mode.

LDI-TOF MS imaging was performed on an extensively modified Physical Electronics (Eden Prairie, MN) TRIFT-II (triple focusing time-of-flight) mass spectrometer equipped with a phosphor screen/CCD camera optical detection combination as described in detail by Luxembourg et al.<sup>107</sup>. This setup, which was originally designed for MALDI-imaging purposes, offers the possibility of both microscope and microprobe MS imaging. The time-of-flight data is recorded using a digital oscilloscope as described by Luxembourg et al.<sup>107</sup>. LDI microprobe imaging was performed on the paint-layer cross-section using a diode pumped solid-state Nd-

YAG laser source, at 355 nm wavelength and 2 ns pulse duration (BrightSolutions, Italy). Seven linescans were made in the direction perpendicular to the layer alternation with an interval of 80  $\mu\text{m}$ /linescan. The scan speed was 50  $\mu\text{m}$ /second at 10 Hz laser frequency. With a laser spot-diameter of approximately 200  $\mu\text{m}$ , this resulted in a microprobe scanned image of 240x7 laser shots, representing an area of approximately 1300x680  $\mu\text{m}^2$ . Each microprobe pixel represents an area of the spot-size of the laser, therefore there is an overlap between the data recorded at neighboring sample points.

### 6.2.3 Data preprocessing

The data was read from .GRD-files (Generic Raw Data) or .RAW-files for IonTof data and TRIFT data respectively, using MatLab (version 7.0.4, R14, SP2, The MathWorks, Natick, MA). Reading in the full data files ensures inclusion of all information recorded during the analysis. It also reduces operator time as no peak-picking is necessary. From the data read-in, a list is created containing the position as a 1-dimensional representation, the channel number,  $c$  (which is linearly related to the flight time), and the number of counts ( $n$ ) for that respective occurrence. This dataset, which represents a datacube, can subsequently be converted into an  $x \times y$  by  $c$  unfolded datacube containing the number of counts for each spectral and spatial combination.

The LDI-TOF spectra were imported into a MatLab environment for further analysis. This resulted in an  $x \times y$  by  $t$  unfolded datacube in which  $t$  represents the time-of-flight. After time-of-flight calibration a mass-spectrum is obtained for every shot and every position. No smoothing or background thresholding/compensation was applied for further analysis.

Several matching spectral and spatial components can be extracted using the different techniques for multivariate analysis on the same unfolded matrices. Commonly, the resolution that can be used during the analysis is limited by the amount of memory that is available to store a partial solution, for instance the covariance matrix in a PCA. Therefore it is necessary to use a matrix that stores the information as memory-efficient as possible, yet with a resolution high enough to obtain accurate results. MS imaging data is generally very sparse (it has large spectral areas with zero counts), the use of a sparse matrix format is therefore an obvious choice when using MatLab. This data type uses a Harwell-Boeing format which leaves out the storage of zero-counts in the mass spectrometry data without loss of information. Therefore it saves memory space for datasets containing a large number of zeros and thus increases the size of the dataset that can be processed.

Although the sparse matrix format allows much larger datasets to be processed, the matrix size has to be reduced due to memory limitations. This data-reduction was done by binning. Binning also reduces computation time. Moreover, binning increases the contrast in datasets<sup>236</sup>.

Binning of the TOF-SIMS data in the TOF dimension was done on channel numbers instead of the mass scale most commonly used. This binning was done by summing the counts of a certain consecutive number of channels. All further analysis was performed on the (binned) channel numbers. Using the 32-bit integer channel numbers instead of mass-numbers, avoids roundoff-errors that are made when these would be converted into floating-point  $m/z$  values. Using the channel integers also ensures that the spectral resolution of the decomposed data is the highest at positions where the original measurement had its highest resolution. Channel-wise binned data therefore gives a higher resolving power at lower masses, which is advantageous for height-mapping purposes<sup>108</sup> and when compounds with the same nominal mass need to be resolved<sup>234</sup>. The mass resolution at higher masses is lower, but the resolution can still easily be kept high enough to resolve nominal mass around  $m/z$  500.

Spatial binning is used to enhance the imaging signal-to-noise ratio for lower abundant species and to increase image contrast<sup>134</sup>. This also reduces the amount of memory needed and decreases computation time during analysis. The spatial binning is done with a factor of 2 in each direction, so that neighboring pixels are added and no fitting between pixels is necessary. Although binning results in a decrease in spatial detail, it has turned out to be very effective in increasing image contrast, especially for images with highly sparse features<sup>143</sup>.

The LDI-ToF imaging data was spectrally binned with a factor of 50. No spatial binning was necessary as the full dataset only contained 2030 mass-spectra.

Apart from spectral and spatial binning, other preprocessing techniques are not evaluated in this article. The effectiveness of most of the common techniques like mean centering, spectral averaging and various denoising techniques is either questionable, or not very useful for SIMS imaging at all. Some of them also take too much computational power or operator interaction to be routinely used<sup>139, 140, 143, 237, 238</sup>. It is beyond the scope of this article to involve in a discussion on these methods. It is very well possible to combine various preprocessing techniques with the techniques presented here. We would only like to mention that mean centering would be not appropriate in our case, as data-processing is performed on full datasets and not only on peaks. The use of spectral mean-centering would then result in negative values for mass-numbers that actually give zero counts and therefore the interpretation of the spectral profiles that result from PCA would be much more complicated. The advantage of the sparse format would be lost as every spectral

parameter would give a certain number of mean-centered spectral counts, resulting in almost no zeros in the matrix.

### 6.3 *Methods for multivariate analysis*

Data decomposition can be performed, using various different multivariate techniques. Most of these techniques use implicit statistics to compress, de-noise or decompose data by extracting statistical features. A well-known method is PCA which can be applied to compress an image, but more generally to discover patterns in high dimensional data. PCA is therefore well-suited to be applied on hyperspectral datacubes<sup>239</sup>, because they have both a spatial as well as a large spectral dimension. The need for a method that can automatically extract features from spectral data increases with the increasing resolution of the datacubes resulting from ToF SIMS.

A balance has to be found between the accuracy and the time it takes to produce the results for different methods. We compare some common methods for multivariate analysis with their performance on MS imaging data of different resolution and acquired with different acquisition methods. Performance depends on many variables such as available memory, data complexity and the implementation of the algorithm. An indication of this performance is given by relative comparisons of the time it takes to do the calculations. The qualitative performance will be judged based on the contrast in the spectral profiles and the feature-contrast in the image planes.

#### 6.3.1 PCA

One way to find the principal components in an unfolded datacube  $X$  is by eigenvector decomposition. Both the spectral and the spatial dimension are decomposed into uncorrelated spectral and spatial components. Equation 6.1 describes the PCA decomposition which can be solved by finding the eigenvectors of the covariance matrix of  $X$ .

$$X = Y \cdot P^T \tag{6.1}$$

The first dimension of  $X$  contains the locations in of the unfolded datacube and the second dimension describes the channels. The columns of  $P$  contain the orthonormal loading vectors and columns in  $Y$  the score vectors or spectral profiles in this case. Together these components describe the original datacube in principal components and can be used to compress the datacube or extract correlated spectral and spatial features.

The resulting component images contain the spatial distribution of the corresponding spectral profiles. The components are sorted according to their variance expressed

by the eigenvalues from the eigenvector decomposition. The first components contain the largest contribution to the original datacube and the last components mostly contain the remaining noise. Each spectral and spatial component can contain both positive and negative values which make interpretation not very intuitive. One way to deal with these negative values in  $Y$  is by splitting them in a positive and a negative counterpart. Each of these parts will create loading vectors that result in positive-only score images when they are multiplied with the transposed original matrix  $X$ .

Using the sparse matrix format within MatLab saves memory space, computation time and allows larger datasets to be analyzed. MatLab also provides a sparse implementation to find the eigenvectors and eigenvalues of a sparse matrix. It uses the FORTRAN library ARPACK<sup>240</sup> which uses an implicitly restarted Arnoldi iteration to solve the eigenvector problem for a sparse matrix<sup>241</sup>. One input parameter is the number of eigenvectors that have to be found. Other parameters control the convergence, number of iterations or model specific solutions.

Using this function, the two most important limitations in eigenvalue analysis of large datasets can be largely circumvented. Firstly, the amount of memory needed is considerably smaller than the memory needed to store the same data in a full matrix. Secondly, the calculation time can be decreased as the implicitly restarted Arnoldi method only makes an estimation of the first (user defined) number of eigenvectors. The fact that only a few eigenvectors are calculated, implies that the resulting set of eigenvectors does not form a complete orthonormal basis for the original dataset. This means that if this method is used for PCA, the resulting principal components form only the most important part of the original dataset (whereas the PCA results obtained with the use of traditional eigenvalue determination methods give a complete basis and can therefore be back-transformed into a dataset that is exactly the same as the original data). In practice this does not give any problems as hyperspectral datasets generally contain only a few predominant principal components. Therefore, within the first 20 (or even less) principal components, almost all original data can be described. From a data-compressing point of view, this is sufficiently accurate as well, as usually only a limited number of principal components are stored, still containing more than 99% of the information from the original dataset.

### 6.3.2 PCA and VARIMAX

Additional optimizations can be done after a PCA. One method is an additional fitting of the principal components to maximize the variance expressed in each component. There are a number of maximization criteria but the VARIance

MAXimization (VARIMAX) from Kaiser <sup>242</sup> is the most common. It can be used as a post-processing step after a PCA, By rotation of the orthogonal axis, more simple structures and components with a higher contrast are created. The expression in equation 6.2 can explain the relation with PCA.

$$X = Y \cdot R \cdot R^{-1} \cdot P^T \quad 6.2$$

$X$  is again the original unfolded datacube with  $Y$  the scores and  $P$  the loading vectors. The VARIMAX algorithm tries to find an orthonormal rotation matrix  $R$  so that the variance of the squared spectral components is maximized. The value of minimum relative increase of the objective function to keep on iterating is kept on the default of  $10^{-5}$ . The spectra belonging to the different principal components are then plotted as  $R^{-1} \cdot P^T$ . Related images are scores of this rotated vector.

### 6.3.3 PARAFAC

A more generalized decomposition method in this study is using the PARAllel FACtors (PARAFAC) model of Harshman <sup>243</sup>. Its exact model was independently proposed by Carroll and Chang <sup>244</sup> as CANonical DECOMPosition (CANDECOMP). This model uses fewer degrees of freedom to fit the data on a simple model for decomposition. It gives a unique solution for the decomposition and makes it possible to put constraints and weights on the resulting components. These constraints can be orthogonality, non-negativity or unimodality with implicit non-negativity. Equation 6.3 gives a representation of PARAFAC that can be compared with the model used in PCA.

$$X_k = Y \cdot D_k \cdot P^T \quad 6.3$$

$X_k$  is again the unfolded datacube that is decomposed in loading vectors in  $P$  and score vectors in  $Y$ .  $D_k$  is a diagonal matrix giving a unique weight to each component. The user has to set the number of components in which  $X_k$  has to be decomposed. We used the fast and optimized iterative implementation described by Bro <sup>245</sup> to decompose the datacube with only the non-negativity constraint on matrices  $Y$  and  $P$ . An orthogonality constraint could not be applied together with the non-negativity constraint. The convergence criterion was the default value of a relative change in fit of less than  $10^{-6}$ . The MatLab implementation that was used is able to handle sparse matrices using the same computational algorithm. This enables us to compare the components from a common and sparse PCA with the extracted components from the PARAFAC model.

### 6.3.4 3D visualization of extracted features

Broersen and van Liere<sup>246</sup> describe a technique to visualize correlated spectral and spatial features in a three dimensional volume using PCA. The main characteristics of the scores and loadings of an extracted principal component are highlighted in the original hyperspectral datacube using opacity maps. This enables a user to select a principal component and interactively view the spectral and spatial contribution within the three-dimensional representation of the datacube. Instead of looking at a solid cube filled with ion-counts, an opacity map gives more ‘insight’ to the data by hiding specific regions using PCA. The opacity map of each component can be adjusted by changing a threshold which controls the amount of data points that is shown. The resulting principal components after the VARIMAX post-processing and the extracted components of PARAFAC have similar properties as those of the PCA. These components can also be used to create three-dimensional opacity maps to automatically create highlights within a datacube and reveal correlated features.

## 6.4 Results

PARAFAC and PCA, along with VARIMAX post-processing were applied on the two datasets described earlier. PARAFAC gave the best separation of chemical components. Therefore the assignment of different chemical components in the samples will be done using the PARAFAC results. After that, a comparison is made between PCA with and without post-processing, along with a comparison with PARAFAC. It is very difficult to exactly quantify the quality of a multivariate analysis unless done on a synthetic dataset, which was not done here as it is ambiguous how a synthetic dataset representative for a real sample would look like. We therefore qualitatively assigned the methods and compared the different implementations (for sparse and non-sparse matrix formats) of the various methods within the same dataset. As a quantitative comparison, the computation time of different methods was compared to give an indication on the usefulness in routine analysis.

### 6.4.1 PARAFAC

A PARAFAC analysis was done on the full acquired dataset of the PVP-droplet sample, with a spectral binning factor of 1024 and a spatial binning as a factor of 2 (resulting in 128x128 pixel images). The dataset was cutoff at the 1250<sup>th</sup> binned channel (which corresponds to  $m/z$  345). This reduction of the dataset was necessary to prevent out-of-memory errors during this computationally demanding method. In this case, the restriction of the dataset to a maximum of  $m/z$  345 does not influence the results of the statistical analysis. In some cases it may be necessary to either perform an additional analysis within the higher  $m/z$  region or to increase the

binning factor. PARAFAC was then done using 7, 14 and 21 decomposition variables (factors). This number of factors was chosen arbitrarily, based on the convenience of the 7-color plotting scheme in MatLab whilst assuring a wide enough range to cover all components. A non-negativity constraint was put on the components, so that only positive scores on the channel numbers were allowed for each variable. The numbered order of the different decomposed components is arbitrary. Therefore, based on the order of the resulting component-spectra, no conclusions can be drawn on the abundance of the corresponding factors. That means that factor 11 could be more abundant than factor 2, which is an important property to recon with when the analysis is done. The random order of the factors is a result of the random initialization that was chosen. Therefore, the order of the factors could vary between different PARAFAC runs on the same dataset.

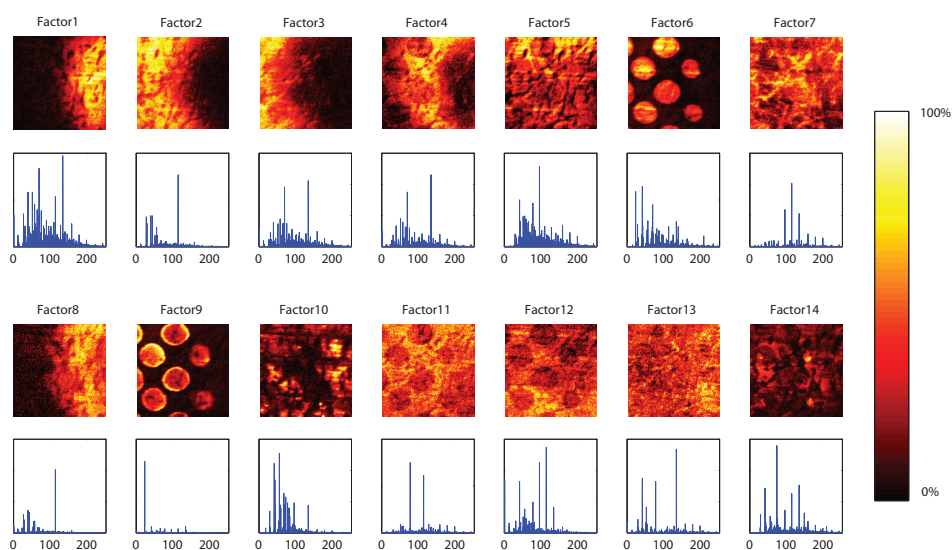


**Figure 6.1** Score plots and loading vectors for 14-component PARAFAC analysis of +SIMS analyzed PVP spots on PVDF membrane. Only positive scores are possible due to the non-negativity constraint that was used in the analysis. Each image is scaled to its maximum (absolute) intensity.



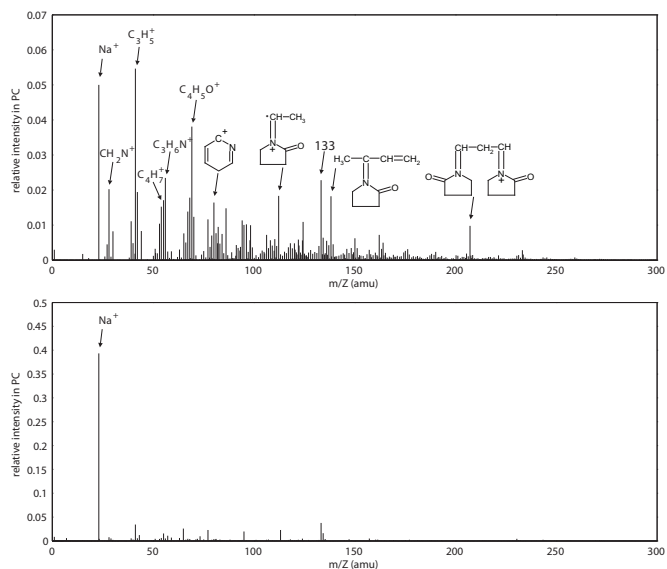


**Figure 6.2** The loading vectors of PC 6 (top) and PC 9 (bottom) as obtained from 14-component PARAFAC analysis of +SIMS analyzed PVP droplets spotted on PVDF membrane.

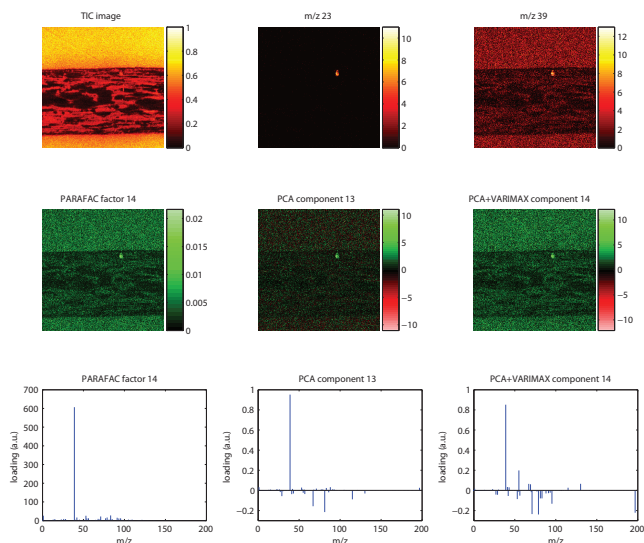


**Figure 6.3** SIMS images of the cross-section of hair embedded in a methacrylate embedding medium. The total ion image (top left) does not give any indication for the salt crystal as shown with the images at  $m/z$  23 and  $m/z$  39 (top middle and right respectively). The bottom images show the score images of the major resulting factors from the three investigated methods. The different colormaps are chosen for visibility reasons: a “hot” colormap as used in the top images would not be appropriate in the PCA score images because of negative values.

A few chemical components gave one specific factor in PARAFAC, irrespective of the number of chosen factors to be resolved. These included the “salt rim”, which is the result of transportation of salts to the edge of a drying droplet, and the PVP droplet itself (factor 9 and factor 6 respectively in the 14-factor PARAFAC analysis, Figure 6.) This can also be clearly seen from the corresponding spectra (figure 6.1): factor 9 gives a very high score at  $m/z$  23 ( $\text{Na}^+$ ), a low but distinct peak for  $\text{Li}^+$  (7) and only minor scores for other species.  $\text{Na}^+$  is highly abundant in factor 6 as well; in any other factors its presence can be neglected, showing that the  $\text{Na}^+$  indeed comes from the solution used during the spotting procedure. Factor 6 shows peaks at positions that are specific for PVP<sup>168</sup>, along with the peak at  $m/z$  133, which seems to be present in almost all factors (closer examination of the unbinned spectrum shows that this nominal mass indeed contains multiple peaks with different exact masses). Assignment of the various peaks in the spectra belonging to factors 6 and 9 is indicated in figure 6.2. Factor 10 and, to a lesser extent factor 14, show distinct structures. These localized components represent a contamination on the PVDF membrane that was introduced when the membrane was attached to the substrate. The inner side of a polyethylene bag was used to tighten the membrane onto the substrate and factor 10 results from erucamide ( $\text{CH}_3(\text{CH}_2)_7\text{CH}=\text{CH}(\text{CH}_2)_{11}\text{CONH}_2$ ), which is commonly used as a slip agent for polyethylene. A distinct  $[\text{M}+\text{H}]^+$  peak for erucamide was seen at  $m/z$  338. It is striking how well this low-abundant surface component is resolved.

Special attention needs to be paid to the different ways the signal from the PVDF membrane is decomposed into various factors. These factors can be identified by the typical 20 or 38 amu separated peaks due to respectively HF and 2F mass difference between the fragments. This PVDF-related chemical component is divided into various factors for PARAFAC using 14 or 21 factors, all containing a different combination of PVDF-specific peaks. However for the 7-component analysis, the substrate membrane was only divided into a few components (most of which seemingly represented different height zones, as can be concluded from a comparison with the PCA analyses where similar images have height-specific spectra). The division of this single chemical component into multiple factors is a result of the orderless factorization which seeks for a fixed number of components that have no specific order of importance.

Also the cross-sectioned hair was analyzed with PARAFAC. Decomposition into 7 factors gives one factor that is specific for the embedding medium. All other factors seem to be non-specific, suggesting that there are no other chemical components present in the analyzed dataset. However, when 14 factors are allowed, a specific spot is resolved, spectrally corresponding to a peak at  $m/z$  39, which results from  $\text{K}^+$ .

More close analysis of the factors showed that also the very low-abundant  $\text{Na}^+$  ( $m/z$  23) is specifically localized at this position and only present in this certain factor (Figure 6.). This once more shows the power of computational analysis as this feature would not be resolved without the use of statistical data analysis.

LDI-ToF microprobe imaging data was analyzed with PARAFAC. The two known components (phtalocyanine blue and phtalocyanine green) were clearly resolved by PARAFAC, irrespectively the number of chosen factors (figure 6.4). Phtalocyanine blue is seen as  $\text{M}^{++}$  ion at  $m/z$  575 and as  $\text{M}_2^+$  at  $m/z$  1150. Phtalocyanine green shows a  $m/z$  35 spaced profile from  $m/z$  1127 ( $\text{M}^{++}$ ) down to 915 ( $[\text{M} - 6\text{Cl}]^+$ ). Each spacing of approximately  $m/z$  35 represents a chlorine loss. Overestimation of the number of factors results in the splitting of single chemical components into different factors, as can be seen from the 14-factor analysis of the LDI-analyzed paint-sample. Factors 3 and 13 (phtalocyanine blue), as well as 4 and 14 (phtalocyanine green) show very similar localization but are nevertheless represented as different factors. This is not necessarily an artifact from the high number of factors, and could as well result from correlation between various measured ions within one layer.

### 6.4.2 PCA on sparse datasets

PCA was done using an in-house developed toolbox based on standard library functions in MatLab. PCA was done on the PVP array spotted on PVDF membrane. All decompositions were restricted to the first 20 principal components, unless mentioned otherwise. This number of PCs was chosen after analysis of higher PCs, which only yielded non-specific spectra and features. The preferred spectral and spatial binning factor should be chosen dependant of the character of the dataset (which in turn depends on the measurement circumstances), the type of compounds of interest and the intensity of the signal. A tradeoff has to be made between these parameters and the amount of memory that is available for the analysis.

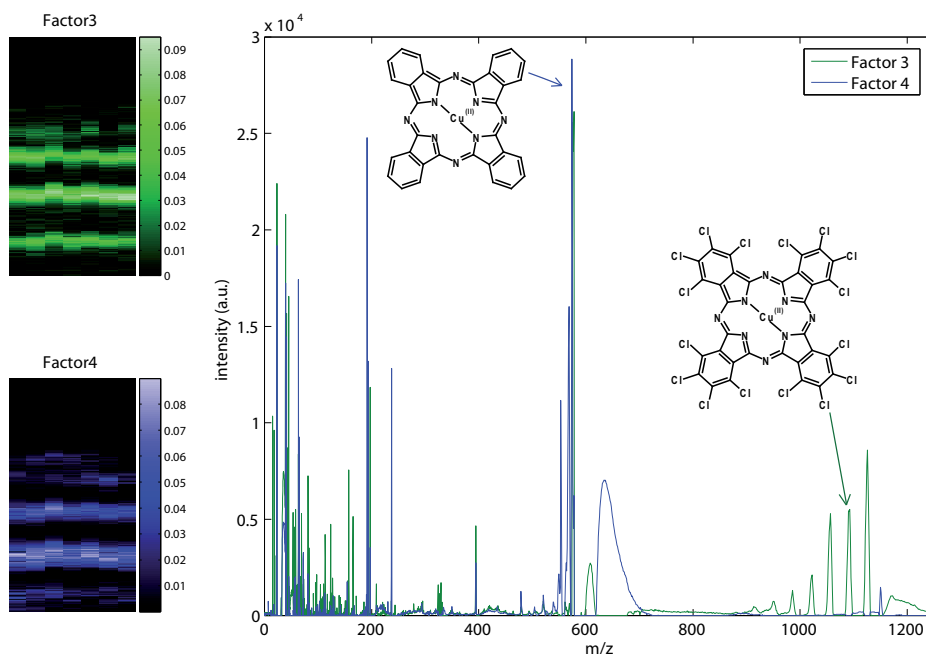


**Figure 6.4** Score images (left) and loading vectors represented as mass spectrum (right) of the PARAFAC analysis of a LDI-microprobe imaged stack of Liquitex paint layers.

Conclusively, PARAFAC was able to extract chemical features into single components. However pre-knowledge is favorable as it will factorize the data into a certain, user defined, number of factors. In essence this number can be made high enough to surely exceed the number of actual chemical components, however this will lead to the factorization of one actual component into a number of factors, as can be seen from the 14-factor analysis. This over-factorization cannot always be avoided as was shown for the extraction of the salt-crystal in the hair cross-section.

A complicating factor of the comparison with PARAFAC is that no model information can be used during PCA. Therefore a non-negativity constraint can not be used, which implies that one PC can actually contain two chemical components, if they are anti-correlated. This means that in a two-phase system, all chemical information could be contained in a single PC. In the case of the PVP droplet array on PVDF, this was seen as a combination of a PVP-specific loading vector, together with an anti-correlated PVDF spectrum because the PVP partially covers the PVDF membrane and therefore absence of PVDF comes together with presence of PVP. For the cross-sectioned hair, just like with PARAFAC, the only chemical components that were resolved was the salt crystal (seen in one of the higher PCs) and the embedding medium. This implies that PCA is a suitable technique to resolve small features as long as the chosen number of components is high enough.

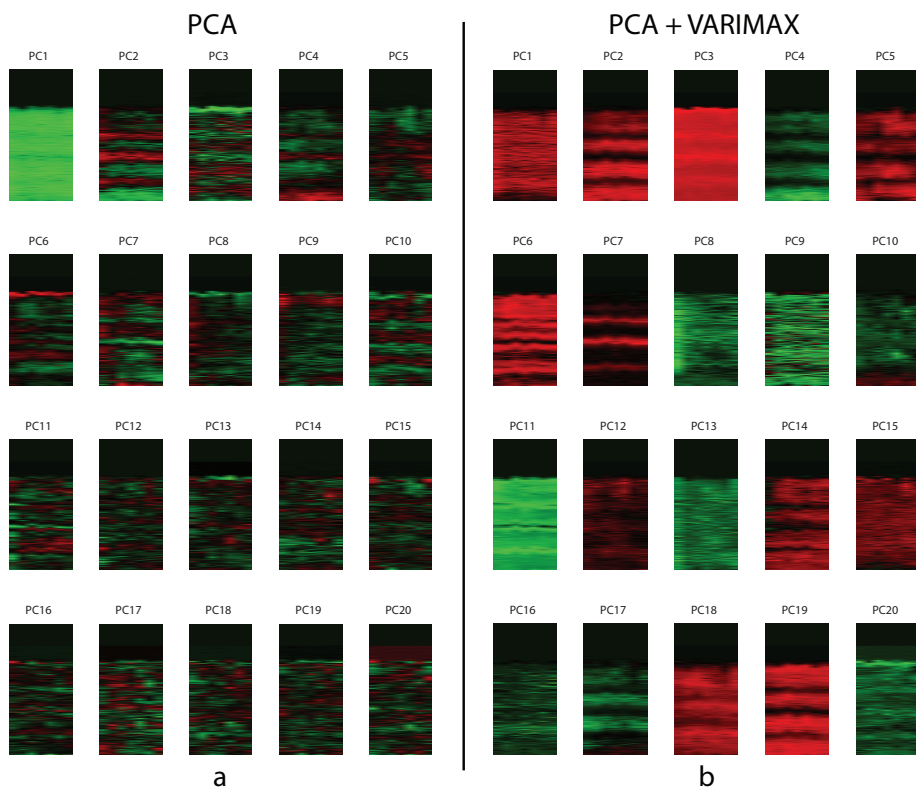


**Figure 6.5** Score images resulting from 20-component PCA (a) and PCA+VARIMAX (b) analysis of a layered structure of Liquitex paint. The size of the area represented by the images is approximately  $1300 \times 680 \mu\text{m}^2$ , the paint layers are overlapping and show up thicker than  $100 \mu\text{m}$  due to the laser spot size of  $200 \mu\text{m}$ .

The spectral features specific for the Liquitex stacked-paint sample that was measured using LDI, were decomposed into more than 2 principal components by PCA. When 20 PCs were chosen, both the phtalocyanine blue and phtalocyanine green are found in various PCs, often as anti-correlated features. This results in PC score-images that give very little localization (figure 6.5 a).

The results obtained with PCA using the implementation for sparse matrixes were compared with PCA as done on full matrixes for the PVP droplet-sample. A comparison was made by calculating the average of  $q_{in} = p_{in}^F / p_{in}^S$  in which  $p_{in}^S$  is the  $n$ -th sparse-type PC result and  $p_{in}^F$  the  $n$ -th standard (full-matrix) result in the  $i$ -th spectral dimension. For identical datasets this would give  $q_{in} = 1$  for any  $i, n$ . For datasets that are not correlated, the variation in values for  $q_{in}$  would be very high. The average values as well as the standard deviation for the first 100 PCs are plotted

in figure 6.6, together with the first 10 maximum values of  $|q_{in}|$  for each  $n$  and their average. This plot shows the high correspondence of the results of the two PCA methods as can be concluded from the few high values for  $q_{in}$ . This is confirmed by the average of all  $q_{in}$  values, which is close to 1 (only a little bit smaller due to a few  $q_{in}$  values that are equal to zero due to a  $p_{in}^F=0$ ;  $p_{in}^S \neq 0$  for all  $i$ ,  $1 \leq n \leq 100$ ). Larger standard deviations are more common at higher PC numbers. This is explained by the fact that higher PCs represent less chemical information. This can result in a different PC order for different computational methods as well as a less exact definition of the PCs by themselves (actually noise is compared with noise). Ill defined PCs result in high values for  $q_{in}$  in some cases. Figure 6.6 indeed shows that up to PC12 the two methods give identical results, with increasing PC number, this error also increases, as well as the variance in the highest 10 values for  $q_{in}$ .

### 6.4.3 VARIMAX post-processing

VARIMAX rotation was used to enhance the spectral contrast of the PCs. This axis-rotation results, as expected in higher contrast not only in the spectra, but also in the images. The resulting PCs do not necessarily correspond with the original PCs. This is shown for the PVP droplet-array, where the loadings vector of PC3 looks completely different after VARIMAX rotation. The rotation did indeed increase both spectral and image contrast, as can be seen from figure 6.7 (before optimization) and figure 6.8 (after optimization). Especially the predominant chemical features that were mentioned earlier in the PARAFAC analysis were represented by single components. After VARIMAX, PC2 contains only the PVP-specific spectral features (as negative peaks) with a few anti-correlated components (as positive peaks) whereas many other peaks were observed before optimization. The optimized PC6 shows hardly any peaks apart from the  $\text{Na}^+$  signal at  $m/z$  23 whereas it was hardly resolved before VARIMAX.

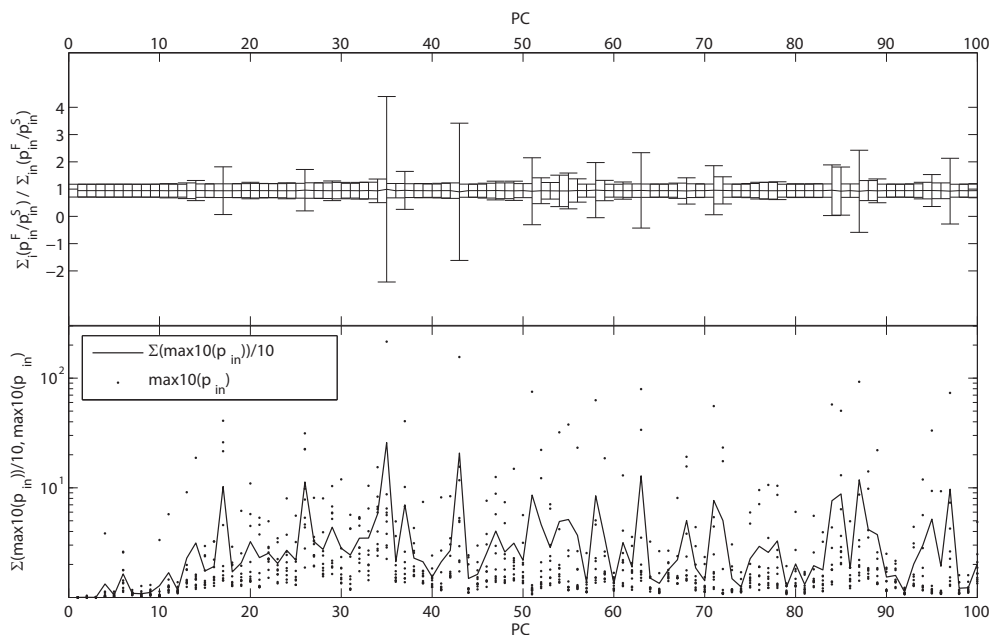


**Figure 6.6** The average  $q_{in}$  values with their corresponding errors (top), and the 10 maximum values for  $q_{in}$  as well as their average (bottom).

The representation of height differences, which is typically observed in the PC-spectrum as the combination of both a positive and a negative peak within the same nominal mass-number is concentrated into two PCs (1 and 7) that only contain this type of peak. The rough PC result showed these peaks in a mixture with other peaks (PCs 3 and 7).

VARIMAX done on the cross-sectioned hair did not improve the chemical contrast. Although image contrast improved, the specificity for the observed salt crystal decreased (figure 6.9). Chemical features were resolved in a comparable way as those found with PCA. The image contrast was improved and used to identify the sharp boundaries of various spatial features.

The LDI-ToF PCA results optimized with VARIMAX show a tremendous increase in contrast as compared to the PCA results without VARIMAX optimization (Figure 6. b). Although the two different paints are found in various PCs, VARIMAX proves to be a very powerful tool in the optimization of PCA-aided analysis of this microprobe LDI dataset, giving phtalocyanine blue (combined PCs 2, 4, 5 and 19) and phtalocyanine green (PC 7) specific spectral profiles.

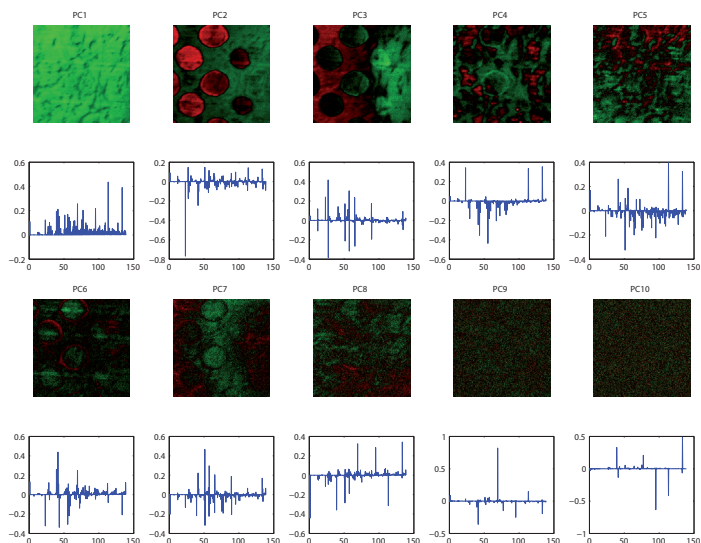


**Figure 6.7** The first 10 principal components as obtained with sparse-type PCA on a droplet array spotted with PVP on a PVDF membrane. The pseudo-colors represent positive (green) and negative scores (red) on the principal components. For clarity reasons, only the low-mass part of the mass spectrum is shown. Each image is scaled to its maximum (absolute) intensity.

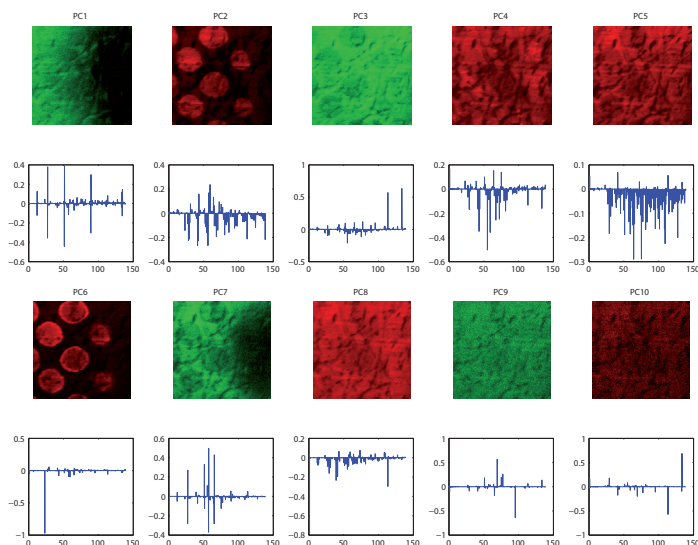


**Figure 6.8** The first 10 principal components as obtained with sparse-type PCA followed by VARIMAX rotational optimization on a droplet array spotted with PVP on a PVDF membrane. The pseudo-colors represent positive (green) and negative scores (red) on the principal components. For clarity reasons, only the low-mass part of the mass spectrum is shown. Each image is scaled to its maximum (absolute) intensity.



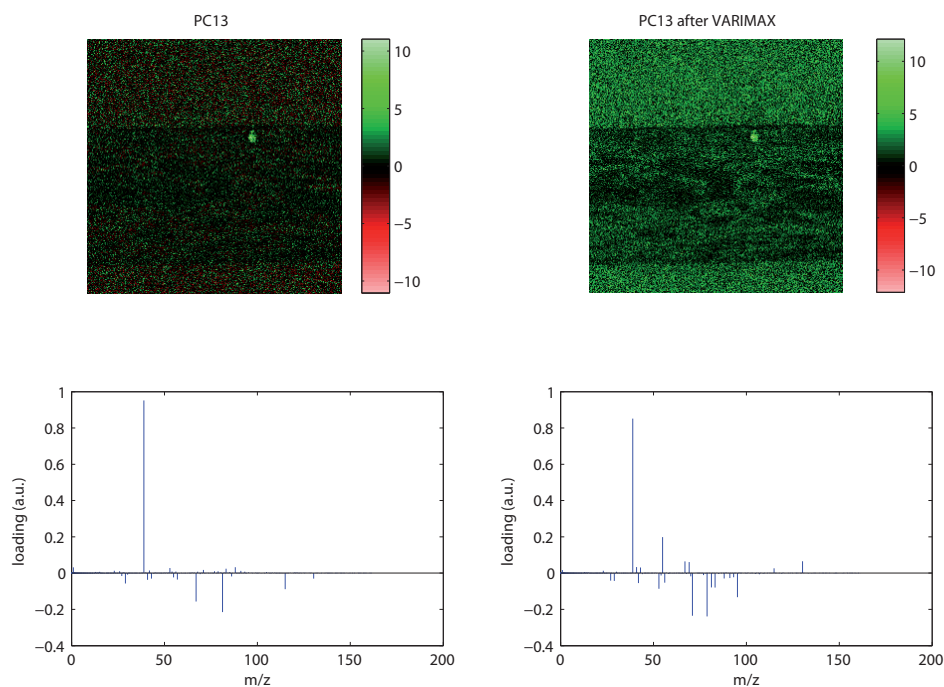


**Figure 6.9** Score images (top) and loading vectors (bottom) after analysis of the cross-sectioned hair with PCA (left) and PCA+VARIMAX (right). Each image is scaled to its maximum (absolute) intensity.

#### 6.4.4 Computation time vs. results

As mentioned in the introduction, computational power is one of the main aspects for multivariate data analysis. An estimate of computation time was made for the studied methods. All time-measurements were done on the same computer (single processor 32bit AMD Athlon, 2.2GHZ, 1GB of memory), using MatLab 7.1 with the N-way toolbox 2.11<sup>245</sup> and VARIMAX implementation. Calculations were done in a 32-bit environment. This limits memory allocation (and therefore the maximum size of the analyzed dataset) to 4 GB. The use of a 64-bit environment would circumvent this memory problem and therefore make the use of larger datasets possible. However, this would also increase calculation time. The size of the quantitatively analyzed datasets was chosen such that the total calculation could be done without the need of virtual memory. Using virtual memory would dramatically increase the total calculation time because hard disk access is much slower than RAM access. This would not give a representative measure when the algorithms are compared.

Computation time was evaluated all three datasets mentioned earlier (table 6.1). Two different datacubes were used for the ToF-SIMS datasets: one with a large spectral dimension and one with a large spatial dimension (datacubes were unfolded into  $x \times y$  by  $c$ ). The number of components was varied from 7 to 14 to 21. The LDI-ToF imaging datacube was analyzed at full spatial resolution ( $7 \times 290$ ) and with 1850 spectral variables.

The standard PCA method first calculates the full and exact PC decomposition and then restricts the resulting dataset to the requested number of components. PCA performed on sparse matrixes produces an approximation by itself, not giving a full representation of the original datacube, but only resulting in the requested number of PCs. This difference in methodology, contributes to the time-reduction that is involved in the use of sparse-matrixes. The continuous nature of the LDI data, with a non-zero entry at almost each sampling point resulted in an increased computation time when the sparse matrix format was used. This can be explained from the fact that the in-memory size is larger for the sparse-type matrix than for the full matrix, which inevitably leads to larger processing times.

*Table 6.1 Table with an indication of computation time in seconds using various methods on various samples. The VARIMAX processing time is given as the time added to PCA.*

<b>set</b>	<b>compo</b>	<b>dataset size</b>	<b>PCA</b>	<b>PCA</b>	<b>PCA+</b>	<b>PARAFAC</b>	<b>PARAFAC</b>
	<b>-nents</b>			<b>sparse</b>	<b>VARIMAX</b>		<b>(sparse)</b>
hair	7	300x256x256	3	3	+ 0.15	3.5x10 <sup>3</sup>	2x10 <sup>3</sup>
droplet	7	300x256x256	3	3	+ 0.15	12x10 <sup>3</sup>	6.5x10 <sup>3</sup>
hair	14	300x256x256	3	3	+ 0.25	6x10 <sup>3</sup>	5x10 <sup>3</sup>
droplet	14	300x256x256	3	3	+ 0.25	40x10 <sup>3</sup>	50x10 <sup>3</sup>
hair	21	300x256x256	3	5	+ 0.35	14x10 <sup>3</sup>	13x10 <sup>3</sup>
droplet	21	300x256x256	3	4	+ 0.35	160x10 <sup>3</sup>	85x10 <sup>3</sup>
hair	7	5053x64x64	5x10 <sup>2</sup>	25	+ 0.2	0.9x10 <sup>3</sup>	1x10 <sup>3</sup>
droplet	7	5053x64x64	5x10 <sup>2</sup>	20	+ 0.2	0.7x10 <sup>3</sup>	0.6x10 <sup>3</sup>
hair	14	5053x64x64	5x10 <sup>2</sup>	25	+ 0.3	3.5x10 <sup>3</sup>	3x10 <sup>3</sup>
droplet	14	5053x64x64	5x10 <sup>2</sup>	20	+ 0.3	9x10 <sup>3</sup>	8x10 <sup>3</sup>
hair	21	5053x64x64	5x10 <sup>2</sup>	30	+ 0.4	6x10 <sup>3</sup>	4x10 <sup>3</sup>
droplet	21	5053x64x64	5x10 <sup>2</sup>	20	+ 0.4	30x10 <sup>3</sup>	27x10 <sup>3</sup>
LDI	7	1850x290x7	30	35	+ 0.15	52x10 <sup>3</sup>	55x10 <sup>3</sup>
LDI	14	1850x290x7	30	35	+ 0.30		214x10 <sup>3</sup>
LDI	21	1850x290x7	30	35	+ 0.40		

VARIMAX as a post-processing optimization step after PCA results in only a small increase in calculation time. This justifies the use of VARIMAX after PCA in any case to increase chemical contrast in both PC images and spectra, as shown in previous sections.

PARAFAC is clearly a much more demanding technique. Although it turned out to be better at resolving certain features, it is not suitable for routine use with the current standings of on-desk computer facilities. It could be very helpful in very complex systems or in systems where trace amounts of a certain chemical components are expected. Prior knowledge, which is favorable to make a sensible choice for the number of components to be looked for, could be obtained using PCA. Like PCA, PARAFAC turned out to be faster on sparse matrixes. It should be mentioned that the random initialization as used in our PARAFAC calculations, results in a large variation in calculation time and the order of the factors. PARAFAC is a computationally much more demanding technique because it seeks an exact fit of the data using optional constraints, spread over the defined number of factors.

#### 6.4.5 3D visualizations

The components from the different methods for multivariate analysis yield a specific extracted spectral profile with a corresponding spatial view. It is hard to give an interpretation using only the individual spectral or spatial component. PCA was able to extract the location of a feature in the hair, but the spectral view revealed that it was caused by a salt-crystal. A combined view would directly reveal the connection between both views. Each pair of extracted scores and loadings can be combined in one three-dimensional overview to gain more insight in the correlations between spectral profile and the location. Each value in the cube is the intensity on a certain position in a spectral plane and is given a color using the 'hot'-colormap from MatLab. Because most values are zero within a MS dataset, the complete cube would result in an image of a black box. Large parts of this box can be discarded as they do not contain any interesting properties. An opacity map is introduced to hide uninteresting features within the datacube which, in this case, is created with the extracted components from the multivariate analysis. Instead of a continuous switch between spectral and spatial view, a complete view of the cube can directly reveal this connection. A user is able to interactively rotate the cube and instantly get an overview of all the data in three dimensions.

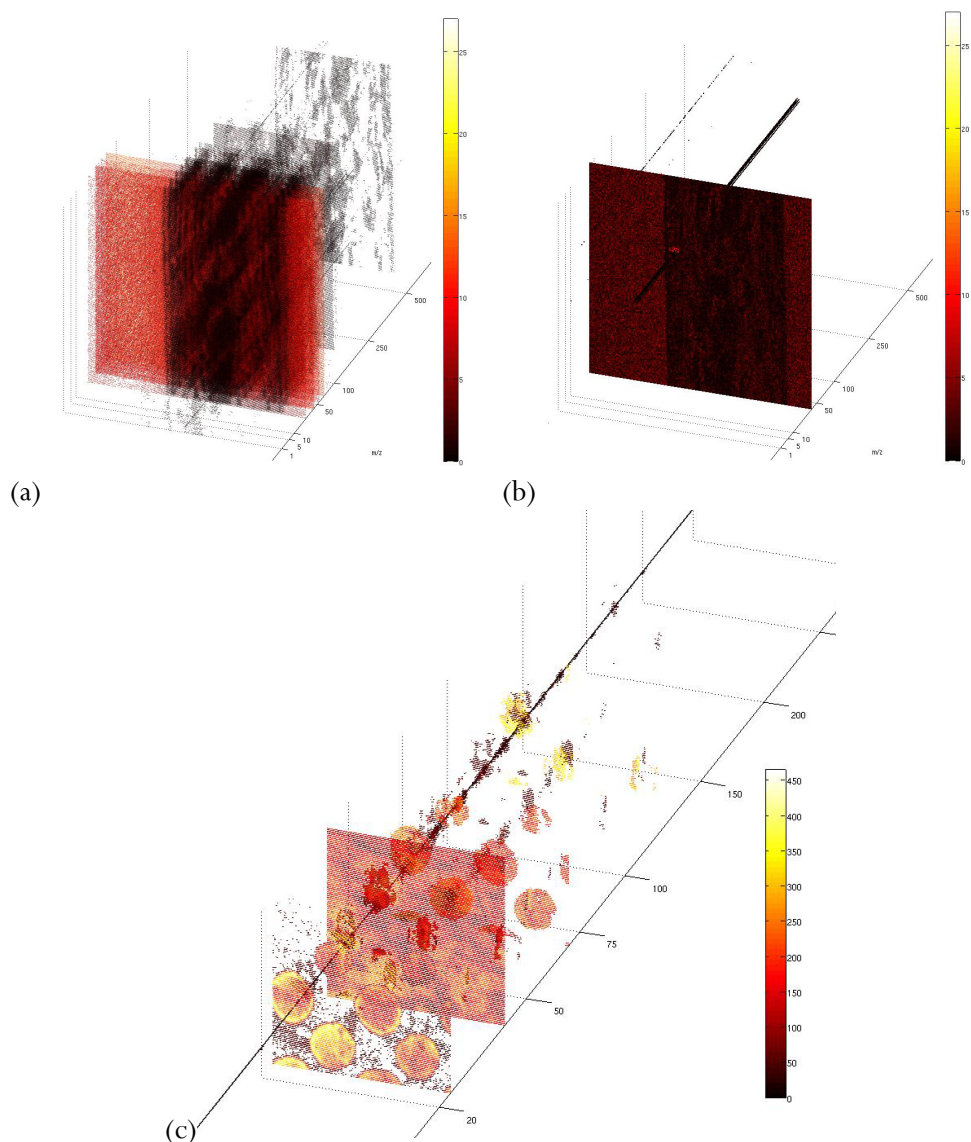


**Figure 6.10** An alternative representation of the complete hyperspectral datacube of the embedded hair with an overlay using PC1 (a) and PC13 (b) and the PVP droplet series with the 6th PARAFAC factor (c).

The complete hyperspectral datacube of the hair is shown in figure 6.10 a and b. Only the high values in the spectral profile and image component of PC1 are made opaque by the opacity map. In this way PC1 is highlighted in the original datacube

which contains mostly the areas and peaks from the hair itself. The component with the extracted features from the crystal is shown in figure 6.10 b. It clearly shows the relation between the highlighted image plane on  $m/z$  39 and the small group of pixels on the location of the crystal while other areas of the cube remain hidden. The significant peak on  $m/z$  39 in the spectral component highlights the complete image plane at this spectral position. Similarly, the high intensity of the pixels in the spatial component results in the appearance of a ‘rod’ spanning the whole spectral dimension of the cube. The number of points of this feature that are shown can be adjusted by changing the threshold in the opacity map.

This representation provides better overall insight in the data by visualizing the direct correlation between spectral peaks and spatial occurrences. Figure 6.10 c shows several isolated drops in the spectral datacube using the sixth PARAFAC factor. The different components or factors can be highlighted together or separately in the same cube by combining their opacity maps. The resulting three-dimensional view becomes more accurate and discriminating when the resulting components from the multivariate analysis contain more contrast. This advantage makes it easier to compare the quality of results from the different multivariate analyses.

## 6.5 *Conclusions and discussion*

A comparison was made between various multivariate statistical methods for the analysis of hyperspectral datasets as acquired with ToF-SIMS and LDI-ToF MS imaging. Obviously, the same methods used for LDI-imaging can be used in MALDI-imaging experiments.

The use of the sparse matrix format allows larger datasets to be handled and drastically decreases computation time. Memory problems are circumvented because zero values are disregarded, which is a more efficient way of data storage when most values in the datacube are zero. The sparse matrix format makes the analysis of larger datasets possible and allows them to be analyzed at higher resolution. No significant difference was found between the resulting extracted information of the different implementations for normal and sparse matrixes in specific multivariate analytical techniques.

Of the methods compared in this report, PCA turns out to offer the best trade-off between results and computation time. Although PARAFAC gave a better overall performance, the high amount of computational power needed restricts this technique to the use in specific cases. A sensible choice of the number of components to be calculated is needed in PARAFAC as an excess number of components, dramatically increases computation time. To make an estimation of the number of

components to be calculated in PARAFAC, pre-knowledge is needed. This makes the technique less suitable for routine analysis. The application of VARIMAX rotation as a post-processing technique increases both chemical and imaging contrast when used after PCA. The almost negligible amount of computation time needed for this, suggest that it should be used in any case when PCA is used. However, the original results from the PCA should still be considered because in some cases, especially for small features, the chemical specificity may decrease when VARIMAX is used. In most cases however a pseudo-color plot together with manual analysis of the spectra is sufficient to resolve the various chemical components. A 3D representation of the complete datacube or selected components, was shown to be a useful tool for quick insight into a hyperspectral datacube. Although a scientific expert is still needed to analyze the resulting components, these multivariate statistical methods are an indispensable tool in the analysis of complex MS imaging datasets.

## 7 MASS SPECTROMETRIC IMAGING OF A POLYMERIC HYDROGEL IMPLANT

This chapter is based on:

Klerk, L.A.; Dankers, P.Y.W.; Van Luyn, M.J.A., Sanders, M.E., Reedquist, K.A., Heeren, R.M.A., *in preparation*.

---

Supramolecular polymeric biomaterials are of increasing interest for the use as drug delivery carriers. A thorough understanding of the biocompatibility and the degradation of these materials *in vivo* are of fundamental importance to further development and application in pharmaceutical practice. The understanding can be supported by molecular imaging techniques, elucidating molecular distributions within and around the polymer implant *in vivo*.

Time of flight secondary ion mass spectrometry (TOF-SIMS) imaging is a surface sensitive molecular analysis technique that can help understand the distribution of different molecules in both synthetic and biological systems. In this study, a supramolecular polymeric hydrogel is implanted under the renal capsule and studied using TOF-SIMS. This provides a molecular cartography of the polymer implant as well as the cellular signature of the implantation environment in one single experiment. Cellular infiltration into the polymer is visualized based on cellular molecular signatures. Because it is known that macrophages play an important role in the foreign body response, the molecular signatures are compared with macrophage standards cultured in different polarization environments. Based on this comparison, information can be acquainted on the different macrophage differentiations that are connected to different stages in the foreign body response.

---

## 7.1 Introduction

Over the last half a century, there has been an increase in awareness about the importance of local drug delivery. Delivery at the place in the body where they have to act as well as the elongation of the effective dose level of the drug in the body are important issues in pharmacology<sup>247</sup>. In the development of drug delivery systems, a thorough understanding of the used drugs and carrier materials is crucial. The function of the carrier material is to provide a sustained, controlled release of the drug. At the same time, the influence of the material itself on the body should be kept at a minimum, or at least not cause any unwanted side-effects. It is therefore very important to thoroughly assess the reaction of the body under influence of the drug carrier. It is also very important to have a thorough knowledge of the possible changes of the carrier under influence of the physiological environment.

A novel approach to the controlled release of drugs is the use of supramolecular polymeric biomaterials. The use of supramolecular functionality has been shown to be a very promising as a carrier for drug delivery<sup>223, 248</sup> as well as for tissue engineering<sup>224</sup>. Supramolecular polymers are macromolecules in which the monomers are held together via directed non-covalent interactions or in which polymers are crosslinked through through supramolecular interactions. One way of achieving non-covalent binding is through multiple hydrogen bond interactions. The combination of multiple hydrogen bonds in one binding site is known to lead to cooperatively strong, yet dynamic, binding. The most obvious example of cooperative hydrogen bonding from nature is the interaction between the two strands of deoxyribonucleic acid (DNA). This approach has numerous advantages over classical approaches. Unlike diffusion driven release, the release from a non-covalently bound drug is controlled through the strength of the supramolecular interaction, which can be controlled by choosing different derivatization methods of the drug or the carrier. Covalent binding of the drug to the carrier, on the other hand, restricts the possibility of mixing multiple different drugs in one delivery carrier due to synthetic restrictions. This makes for instance the addition of proteins impossible. Supramolecular binding allows mixing of carrier material, drugs, peptides, proteins, labeling molecules and any other components after the synthesis, in solution<sup>224</sup>. This modular approach offers opportunities that allow the tuning of materials properties as well as pharmacological functionality.

Polymer hydrogels have long been a drug delivery carrier of great interest<sup>249</sup>. In this chapter, we show a hydrogel drug delivery carrier that is composed of elongated polymer chains crosslinked by the quadruple hydrogen bonding ureidopyrimidinone (UPy) group<sup>222</sup>. With classical pathological methods, which are typically based on



immunohistochemistry, the foreign body response can be visualized. However, this is restricted to the available methods and does not allow further investigation of biological activity at the molecular level. Another restriction of immunohistochemical methods is that the polymer cannot be studied simultaneously and therefore the analysis is limited to the biological part of the system. Here we explore the capabilities of imaging mass spectrometry (MS) to fill the gap in our understanding in the interaction between the polymer implant and the biology of the foreign body response using direct molecular imaging. Particularly we use time-of-flight secondary ion mass spectrometry (TOF-SIMS) to investigate the foreign body response based on mass spectrometrically pinpointed molecules.

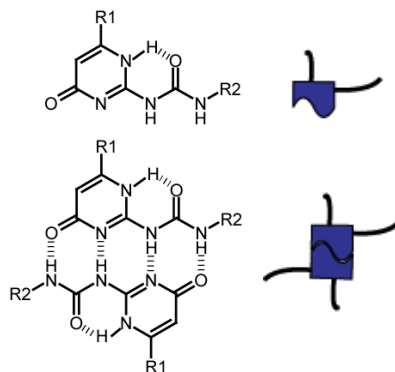


**Figure 7.1** Molecular structure (left) and schematic representation (right) of the quadruple hydrogen bonding ureido-pyrimidinone (UPy).

TOF-SIMS imaging is a technique that can reveal molecular distributions at the cellular length scale<sup>6, 43, 195, 250-252</sup>. It is also widely applied in the analysis of polymers and polymers in the biomedical field<sup>165-167, 253</sup>. Because sample preparation is kept to a minimum, TOF-SIMS is an ideal tool to analyze a combination of cellular structures, polymers and polymer additives, for instance drugs. Analytical techniques that need extensive sample-treatment inevitably introduce a bias towards certain components of the sample for which the sample preparation is ideal, where other components, for which the procedure is far from ideal, are not seen.

In this chapter, we show the results of a TOF-SIMS imaging analysis of a polymer hydrogel implanted under the renal capsule. Cellular distributions are visualized and the degradation of the polymer is studied simultaneously in a single experiment. Spatial information is obtained on the molecules that are involved in the foreign body reaction. Earlier studies have indicated that several stages of macrophage differentiation are actively involved in the foreign-body response on the implanted polymer. Macrophages can be classified in M1 and M2 macrophages<sup>254</sup>. M1

macrophages are typical for type 1 inflammation, which involves tissue destruction and the defense reaction against the foreign body, in this case the implant. M2 macrophages are typical for type 2 inflammation, which involves tissue remodeling/wound healing and angiogenesis as well as encapsulation of the foreign body. To get a full understanding of the foreign body response around the gel implant, it would be interesting to be able to discriminate between these two types of macrophages. Recently, an extended categorization in three types of macrophages was proposed, classifying classically activated macrophages (M1 type), wound-healing macrophages and regulatory macrophages<sup>255</sup>. Identification of the type of macrophage is however not possible with current immunohistochemical methods.

In order to get a better understanding of the expressed molecules in different types of macrophage differentiation, a pilot study was done in which various polarizations are simulated *in vitro* using controlled stimuli. The measured molecular signatures were then compared with the molecular distributions in the tissue sample.

The preliminary data presented in this chapter leaves many questions open. Further study using replicates, as well as validation of the preliminarily assigned peaks is needed before hard conclusions can be drawn on the biological aspects of the studied system. However, the data presented here shows some interesting phenomena that, to our knowledge, were not presented before. This demonstrates the potential of TOF-SIMS, and MS imaging in general, for studying the foreign body response *in vivo*. It provides a wealth of position-related molecular information on the interaction of the living system with a polymer implant.

## 7.2 *Experimental*

### 7.2.1 *Sample preparation*

Polymer hydrogels were implanted under the renal capsule of a rat in collaboration with E.R. Popa and P.Y.W. Dankers (University Medical Center Groningen). The hydrogels were produced in collaboration with A.W. Bosman (SupraPolix B.V.) and composed of supramolecular ureido-pyrimidinone (UPy)<sup>222</sup> modified polymers in 0.9% NaCl. These supramolecular polymers were synthesized in a similar manner as described before for thermoplastic elastomers<sup>223</sup>. They consist of poly(ethylene glycol) ( $M_n = 6000$  g/mole) (PEG) and polycaprolactone ( $M_n = 1250$  g/mole) (PCL) precursor polymers in a 9:1 w/w% ratio chain-extended with a UPy-moiety. These UPy-groups form cross-links between polymer chains through quadruple hydrogen bonding and allow supramolecular binding of functional additives through the same quadruple hydrogen bonding moieties<sup>224</sup>.

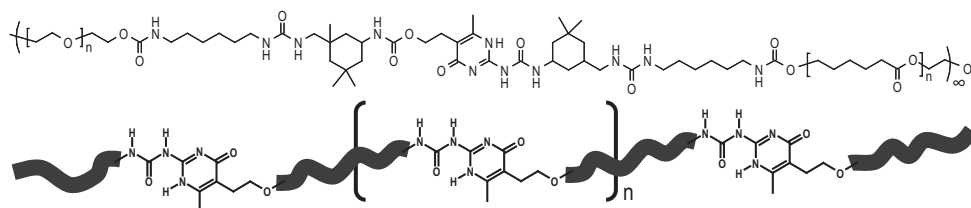


**Figure 7.2** Molecular structure (top) and schematic structure (bottom) of the used hydrogel polymer [(PEG<sub>6000</sub>/PCL<sub>1250</sub>)-UPy]<sub>∞</sub>.

All animal procedures were approved by the committee for care and use of laboratory animals of the University of Groningen and performed according to governmental and international NIH guidelines on animal experimentation. The hydrogels were implanted in Fischer rats (F344, Harlan) under the renal capsule by making a small incision. Through this incision, a pocket was created using a blunt needle in which the polymer hydrogel was implanted. The rats were sacrificed and the kidneys were harvested 15 days after implantation. Half of the kidney was used for pathological studies and embedded in paraffin. The other half was snap frozen in liquid nitrogen and stored at  $-80^{\circ}\text{C}$  for later analysis using imaging MS.

10  $\mu\text{m}$  cryo-sections of the polymer-tissue samples were made using a Leica CM1900 cryo-microtome at  $-20^{\circ}\text{C}$ . Sections were stored at  $-80^{\circ}\text{C}$  until analysis. The sample was brought to room temperature under dry conditions in a vacuum desiccator. One group of samples was coated with 1 nm gold using a Technologies SC7640 sputter coater and one group was left as it was. After preparation, the samples were introduced into the mass spectrometer.

## 7.2.2 Histological staining

Immunohistochemical staining of paraffin embedded sections was performed. These sections were not taken adjacent to the sections that were measured with MS imaging, but from the other half of the kidney or from a different animal with the exact same implant. They nevertheless give a good indication of the histology of the implantation site. ED1 staining was done to visualize the presence of macrophages, which indicates an inflammatory response. Collagen III staining was done to visualize collagen, which indicates the formation of a fibrous capsule around the implantation site. These methods offer an excellent view on the specific labeled components, but no information on the exact molecular composition and no view on the polymer.

The sections that were used for mass spectrometry were imaged using a Leica DM-RX microscope equipped with a Nikon DMX 1200 CCD camera or using a flatbed scanner without prior staining for making overlays with the MS images.

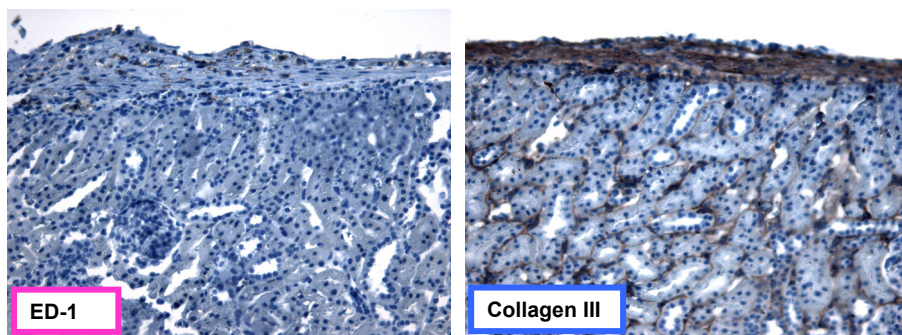


*Figure 7.3 ED-1 and collagen III staining of a rat kidney section with a polymer implant, 15 days after implantation. Staining was done on the paraffin embedded samples. These samples originate from the same kidney as the MS-analyzed samples.*

### 7.2.3 Comparison with in vitro polarized macrophages

To get a more fundamental understanding of the molecular signature of different phenotypes of macrophages, they were polarized in-vitro in close collaboration with K.A. Reedquist and M.E. Sanders (Academic Medical Center Amsterdam). Human macrophages were used and stimulated by six different polarization agents, given in table 7.1.

#### 7.2.3.1 Methods

Monocytes were isolated from human blood, donated by a healthy volunteer. These cells were cultured for 6 days with the addition of rh-GM-CSF 5ng/ml, rh-MCSF 25ng/ml, rh-IFN $\gamma$  20ng/ml, rh-IL-10 10ng/ml (R&D Systems, Abingdon, UK), LPS 1ug/ml from E.coli (Sigma, Zwijndrecht, Netherlands) or rh-TNF 10ng/ml (Biosource, Invitrogen, Breda, Netherlands).

After culturing, the cells were washed with sucrose (300 mmol/L) to remove salts. Cytospinning was performed at 550 rpm for 2 minute on indium tin oxide (ITO) coated glass slides using 40000 cells per sample. Sample slides were pre-wetted for 1 minutes at 550 rpm using sucrose solution.

#### 7.2.3.2 Data acquisition

The human macrophage samples were measured with and without 1 nm Au coating. Only the Au coated samples are considered for comparison with the implantation study to get the most reliable comparison with the Au-coated samples that were used for tissue implant analysis. In Au-coated samples however, some peaks appear that are related to the Au coating (e.g. Au adducts). Therefore, the non-Au-coated samples are used to exclude the possibility of Au-related compounds when doing

peak-assignment in the Au-coated sample. TOF-SIMS analysis was performed using a TRIFT II mass spectrometer (Physical Electronics, Eden Prairie, MN) equipped with a Au primary ion gun. 20 keV Au<sup>+</sup> primary ions were selected for analysis. SIMS spectra were measured both in the positive and the negative secondary ion mode.

*Table 7.1 Overview of the applied macrophage stimuli and their effects*

<b>Polarization stimulus</b>	<b>Effect</b>
Macrophage colony-stimulating factor (M-CSF)	Growth factor, promotes differentiation of monocytes into pro-inflammatory M1 macrophages
Granulocyte macrophage colony-stimulating factor (GM-CSF)	Growth factor, promotes differentiation of monocytes into pro-inflammatory M1 macrophages
Interferon-gamma (IFN- $\gamma$ )	Alarm signal, released when “foreign body” is detected, promotes M1 macrophage polarization
Interleukin-10 (IL-10)	Anti-inflammatory cytokine, promotes differentiation into anti-inflammatory, regulatory macrophages, inhibits pro-inflammatory cytokine production. Stimulates differentiation into regulatory macrophages (M2 type)
Lipopolysaccharides (LPS)	Toll-like receptor ligand, promotes secretion of pro-inflammatory cytokines, macrophage polarization dependent upon cofactors
Tumor necrosis factor- $\alpha$ (TNF- $\alpha$ )	A pro-inflammatory factor that stimulates phagocytosis. Stimulates macrophages into dendritic cells, M1 type of cells.

#### 7.2.4 Statistical data analysis

Statistical data analysis was used as an exploratory tool for the analysis of the imaged implantation samples to cope with the unknown complexity of the samples. Principal component analysis (PCA) and PCA with VARIMAX optimization (see chapter 6 of this thesis) were both used for this purpose. Statistical analysis was also used to explore the data, for this purpose an in-house built “ChemomeTricks”-package<sup>151</sup> was used.

Another reason to use methods to find correlations in the dataset is related to the fact that polymers do not typically show up as a single or a combination of a few peaks but rather as a peak distribution (see chapters 2 and 3). Therefore it is very hard to reveal polymer distributions by simply plotting the distribution of one polymer-specific peak. Although the polymer material can be spectrally identified

from its typical molecular weight distribution peak pattern in many cases, a combination of peaks is needed to give a MS image with sufficient contrast. This is also the case for correlated biologically relevant peaks. Score plots that are a result of PCA are therefore used for visualization as they reflect the combination of relevant spectral features.

## 7.3 Results

### 7.3.1 Hydrogel implantation

Samples were analyzed both at large field of view and low image resolution, and at a small field of view at high image resolution. The large-area image yields an overview of the implantation site. PCA with VARIMAX optimization was done on this dataset, using the mass range between 200 Da and 1000 Da. This gives an overview of correlated peaks in the molecular and large-fragment ion region (figure 7.4). This mass range was chosen because it contains mainly large molecular fragment ions and (quasi-)molecular ions, and therefore gives the most distinctive spectrum. The distributions based on the PCA results give a clear image of the different areas that can be characterized. Several conclusions can be drawn from this image (figure 7.5). Cholesterol, with peaks at  $m/z$  369  $[M-OH]^+$  and  $m/z$  383  $[M-H]^+$  is a highly abundant cell membrane component that localizes in the tissue region. The polymer is seen in the sub-capsular pocket and identified by its characteristic distribution of peaks with a 44 Da interval, the mass of a PEG monomer unit, as well as its 16 Da (O) and 14 Da ( $CH_2$ ) loss pattern (see figure 7.6). A co-localization of various lipids is seen within the polymer area as well as just outside the pocket. The presence of lipids in the polymer region indicates cellular infiltration, or at least biological activity within the polymer. The presence outside the kidney capsid is attributed to adipose tissue. The signal in this region is very high because the lipids form a thin film on the ITO substrate, which enhances the ionization efficiency. Some silicone (most probably polydimethylsiloxane, PDMS) was localized on one side of the implantation pocket. We attribute this to the tools that were used during the surgical implantation procedure, most probably the needle used for making a sub-capsular pocket. Silicones are a common lubricant and biocompatible, and therefore often used as a lubricant.

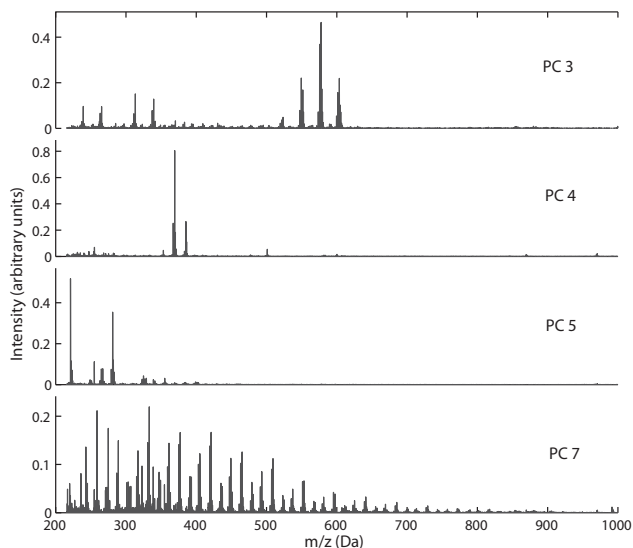


**Figure 7.4** Spectral results of the most indicative PCA results after VARIMAX optimization. The first and second PCs gave non-informative distributions. PC 3 shows signal for various lipids, including diacyl glycerols ( $m/z$  550-610), PC 4 shows cholesterol ( $(M-OH)^+$  at  $m/z$  369.4 and  $M^+$  at  $m/z$  385.4), PC 5 shows silicone contamination ( $C_7H_{21}O_2Si_3^+$  at  $m/z$  221.1, further identified from low-mass peaks in corresponding region), PC 7 shows the polymer distribution, readily recognized from the  $m/z$  44 spacing between the peaks, which exactly corresponds to the mass of one PEG unit.

To get a clearer view on cell infiltration into the polymer material, SIMS imaging was performed at high resolution, using a 360  $\mu m$  field of view. To see enough image detail at this resolution, also the higher intensity low-mass fragment peaks are considered because (quasi-)molecular and large fragment ions often give too low intensity when very small areas are measured. In the positive SIMS mode, this high resolution view (left panel in figure 7.7) shows a choline-predominant region ( $m/z$  104 for the choline headgroup  $[CH_3)_3NCH_2CH_2OH]^+$ ), a polymer-related distribution (indicated by  $m/z$  45 for the PEG monomer  $[C_2H_5O]^+$ ) and a localization for cholesterol-derived compounds ( $m/z$  369, which corresponds to  $[M-OH]^+$ , which is a quasi-molecular ion of cholesterol but could also be related to one of its derivatives). Cholesterol-related signals are high in the fibrous tissue on the exterior side of the kidney and sparsely distributed within the polymer region. Interestingly, the cholesterol signal partially coincides with the PEG signal. The PEG also does not seem to take up the major part of the implant, but rather be distributed within newly formed tissue. When assessing the negative ion SIMS images (right panel in figure 7.7), a remarkable distribution is seen for  $m/z$  465.32. It shows up as a granularly distributed signal within the implantation site and complements a distribution at  $m/z$

124.01 (a peak which could not be identified). The compound that the  $m/z$  465.32 signal results from, is most probably cholesterol sulfate, which has a theoretical mass of 465.304 Da for  $[M-H]^+$ . This is confirmed by the co-localization of the signal at  $m/z$  96.97 and  $m/z$  95.98, which both are due to sulfate-related ions ( $\text{HSO}_4^-$  and  $\text{SO}_4^-$  respectively) but could, at the obtained resolving power, also be due to phosphate ions ( $\text{H}_2\text{PO}_4^-$  and  $\text{HPO}_4^-$  respectively). The fact that the distribution at  $m/z$  78.96, which is due to phosphate ( $\text{PO}_3^-$ ) and cannot be related to sulfate, anti-correlates with the distribution of cholesterol sulfate, shows that the compound at 465.32 is indeed a sulfate. Based on this, a confident assignment of this peak can be made. Furthermore, cholesterol sulphate is known to be abundant in healthy kidney tissue (also seen in the investigated control kidney in this study, see section 7.3.2)<sup>256, 257</sup>. Its function is not fully understood, but suggestions are made about regulating enzyme activity and playing a role in cell adhesion and differentiation as well as signal transduction<sup>258</sup>. In earlier studies cholesterol sulfate was detected in kidney and skin of patients with Fabry disease using TOF-SIMS<sup>259</sup>.

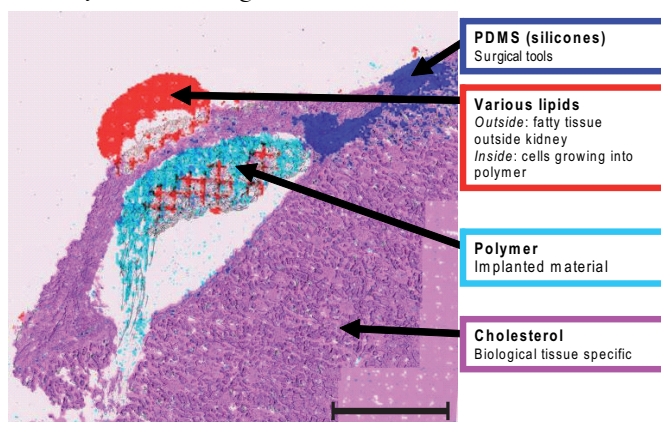


**Figure 7.5** Large area image of the hydrogel implant under the renal capsule of a rat, 15 days after implantation. Various localizations are indicated, based on PCA+VARIMAX results (figure 7.4). The presence of lipids inside the polymer area shows cellular infiltration in the drug delivery carrier. Some smearing artifact is visible at the bottom region of the polymer. The grid-like structure is a measurement artifact, due to decreased sensitivity in the center of the field of view for each mosaic tile. Scale bar = 1 mm.



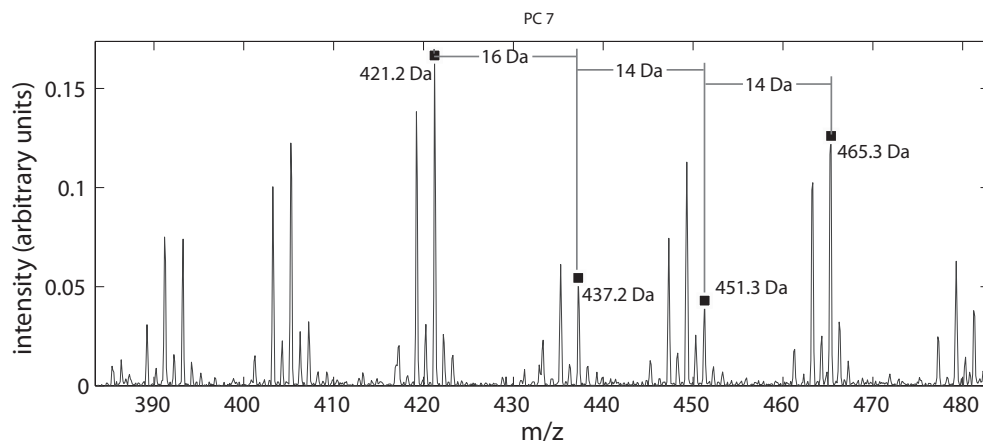


**Figure 7.6** PEG distribution in detail. Because the cationization agent is not known, endgroup analysis is not possible for these fragments. The 16 Da interval can be due to a difference in  $K^+$  and  $Na^+$  cationization or due to O loss. The 14 Da intervals correspond  $CH_2$  loss. Adding up the O and two  $CH_2$  intervals gives 44 Da, the mass of one PEG monomer unit ( $CH_2CH_2O$ ). There is also a 4 Da or 2 Da deviation from the predominant peaks visible, which could be due to unsaturation, for instance in one of the endgroups. The change from .2 to .3 values is due to binning down and thus rounding to 0.1 Da.

When considering the localization of the several components in the positive and negative secondary ion images, several interesting observations can be made. First of all, the PEG signal co-localizes with the cholesterol sulfate signal to a large extent. This implies that a polymer-related signal coincides with a tissue-related signal which means that either these components interchange at a dimension that cannot be seen at this resolution (a few  $\mu m$ ) or there is PEG-related material present inside the cholesterol sulfate containing cells. Furthermore, the cholesterol derived signal (at  $m/z$  369) coincides with the cholesterol sulfate signal as expected, but at a different intensity profile. This is due to the fact that  $m/z$  369 results from a number of cholesterol derivatives, including cholesterol and cholesterol sulfate. Also the abundance of choline, largely anti-correlated with cholesterol-related signal is quite striking as choline is an abundant compound in any biological tissue. Therefore, further analysis, including MS/MS based determination of the assigned compounds is necessary for firm conclusions on the foreign body response mechanism.

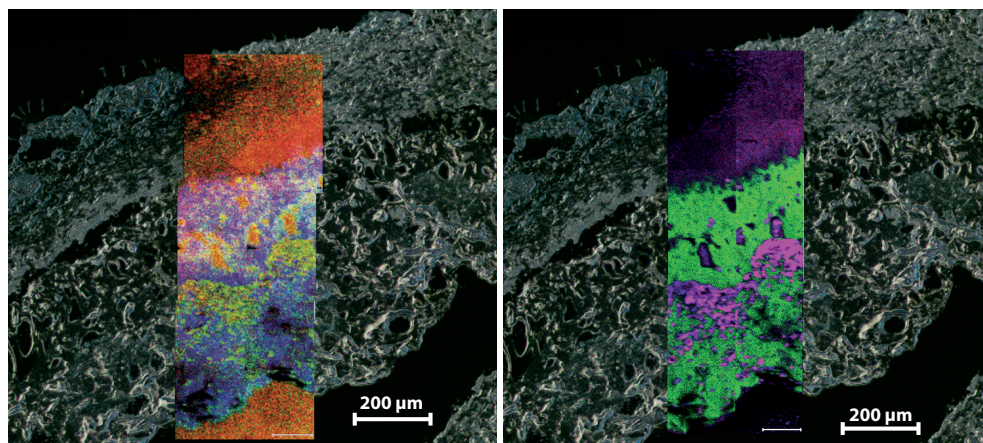


**Figure 7.7** High resolution image of the hydrogel implant under the renal capsule. MS images are shown in overlay with an image taken with an optical microscope. The **left** image, recorded in positive ion mode SIMS, shows distribution for the main cholesterol-derived fragment (red,  $m/z$  369.35,  $[M-OH]^+$ ), PEG (green, seen as the monomer-derived fragment at  $m/z$  45.03  $[C_2H_5O]^+$ , also seen at  $m/z$  133,  $[C_6H_{13}O_3]^+$ ) and choline (blue,  $m/z$  104.11,  $[(CH_3)_3NCH_2CH_2OH]$ ). The high cholesterol signal from the substrate is due to ionization enhancement by ITO, which is a conductor with high primary ion stopping power. The **right** image, recorded in negative ion mode SIMS shows sulfate (blue, 96.97 Da,  $HSO_4^-$ ), which exactly coincides with a compound at 465.32 Da (blue), and an unassigned compound at 124.02 Da (green). The uncertain compound is probably cholesterol sulphate which has a theoretical mass of 465.304 for  $(M-H)^-$  and is confirmed by complementing information from phosphate and sulfate-selective images (see figure 7.8).

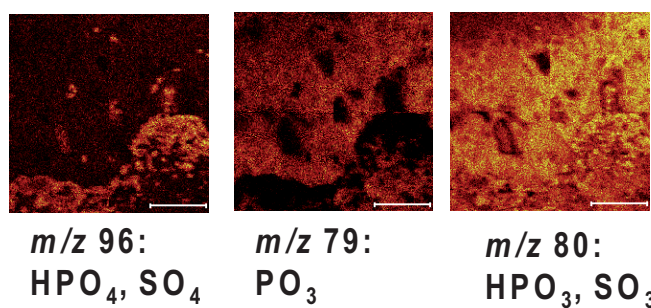


**Figure 7.8** Comparison between different phosphate and sulfate related peaks. The correspondence of  $m/z$  96 with  $m/z$  465.32 in figure 7.7 but not with  $m/z$  79, proves that the compound at  $m/z$  465.32 contains sulfate and not phosphate. Scale bar = 100  $\mu m$ .

### 7.3.2 Macrophage standards

Macrophage standards were imaged using TOF-SIMS. In these images, the cellular region was selected for a region of interest (ROI) analysis. The ROI was determined based on molecular signature (the presence of biological molecules and the absence of substrate-specific peaks) and morphology. The ROI spectra of these cell aggregates were then plotted and phenotype-specific peaks were extracted. Based on these specific peaks, a TOF-SIMS fingerprint of each of the macrophage types is obtained. Many peaks show increased intensity in multiple macrophage types, but some peaks were specific for only one or two types of macrophage polarizations. Based on these more unique peaks, an estimate can be made of the type of macrophages that are present in the tissue samples.

The most intense and specific peaks are listed in table 7.3 for the positive secondary ions and in and in table 7.2 for negative secondary ions. A comparison is also made with the rat kidney standard, to determine presence of the apparent compounds in bare rat kidney. This gives an indication of what peaks, and eventually what compounds, can be expected for the different macrophage polarization.

### 7.3.3 Combining knowledge from macrophage standards with the hydrogel implant

When assessing the peaks that were measured in the differently polarized macrophage standards, a few specific peaks can be picked out. First of all, a peak at  $m/z$  465.3 in negative ion mode is highly abundant in the M-CSF stimulated cells as well as in the control kidney and present at low concentration in the IFN- $\gamma$  and IL-10 stimulated cells. The highly specific  $m/z$  281.2 (oleic acid) in the implantation region, indicates IFN- $\gamma$  like activity (figure 7.9). Oleic acid is also found in the control kidney, but at much lower concentration, which is confirmed by a low signal from the kidney tissue region in the implantation sample. In the positive ion mode,  $m/z$  157.9 is found, which is highly specific for IFN- $\gamma$  and LPS stimulated macrophages. When plotting the distribution of this signal in the implantation sample (figure 7.9), high abundance is seen in the implantation region and low abundance in the kidney region, which can be explained by its low abundance in the control kidney. This, once again indicates towards macrophages that are similar to the IFN- $\gamma$  polarized cells. However, although partially coincident with the oleic acid ( $m/z$  281.2) and  $m/z$  339.1 distributions, the distributions do not completely overlap. A reliable assignment can therefore not be given at this point. Another peak, at  $m/z$  383.3, which is most probably resulting from a vitamin D variant, shows a very distinct distribution along the edge of the implantation site, at the fibrous capsule region.

This peak was seen at high intensity in the M-CSF-stimulated cells, but also in the IFN- $\gamma$  and LPS stimulated cells. Its distribution partially corresponds to the cholesterol sulfate distribution, but there is no exact overlap.

The numerous cross-correlations between the various assessed peaks, shows the complexity of the immune response in general, and after polymer implantation in particular. Although no definite distinction between different macrophage phenotypes can be made at this point, these experiments potentially show insight in different signaling pathways. The images resulting from the implantation study show the potential of using TOF-SIMS imaging for distinguishing between several active domains in the foreign body response.

*Table 7.2 Overview of increased intensity peaks for the different macrophage polarizations as well as the control kidney and their correlations. Data presented for negative ion more SIMS. Indications are relative to the other samples: +++ indicates highly abundant, ++ indicates present, + indicates present at very low concentration, - indicates absent.*

mass	M1 type				M2 type	undefined type	control kidney	kidney with implant	
	M-CSF	GM-CSF	IFN- $\gamma$	TNF- $\alpha$	IL-10	LPS		implant	kidney
45		+++				+++	+	++	+
59					+++		+	+++	+
79		+++					++	++	+
80					++		++	+++	++
213	+++						++	++	-
214					+++		++	+	-
217	-	-	+++	+++	-	-	+	+++	++
281			+++				++	+++	+
411	+++						++	+	+
461					+++	+++	++	++	+
465	+++		++		++		+++	+++	++
490	+++				+++	++	+	+	+

**Table 7.3** Overview of increased intensity peaks for the different macrophage polarizations as well as the control kidney and their correlations. Data presented for positive ion mode SIMS. Indications are relative to the other samples: +++ indicates highly abundant, ++ indicates present, + indicates present at very low concentration, - indicates absent, +++/- indicates present, but very localized. Note that for certain peaks, an accurate mass is given, which is because one of two peaks at single nominal mass gave a different identity.

mass	M1 type				M2 type	undefined type	control kidney	kidney with implant	
	M-CSF	GM-CSF	IFN- $\gamma$	TNF- $\alpha$	IL-10	LPS		implant	kidney
85				+++			+	+++	-
158.05			+++			+++	++		++
158.93					+++		+++	++	+++
159		+++	+++				+++	++	+++
163				+++			+++/-	+	+
172						+++	+	-	-
175			-			-	+++	++	+++
213	+++	+++					+++	+++	++
274.85		+++	+++		+++		+++	+++	-
275	+++						+++	-	+
284	+++				+++		+++/-	-	-
286						+++	-	-	-
329						+++	++	++	-
339			+++			+++	+++/-	+++	-
343					+++		-	-	-
365	+	+++	++	+++	++	-	+	++	+
367	+++	+	+	+	+++	+	++	++	+++
369		-		-			+++	++	+++
371		-		-	+		+	++	+++
381	+	+++	++	+++	++	-	+	++	++
383	+++	+	+++	-		+++	++	++	+
387	+++						++	++	++
389	+++						++	+	+
395	++	++	++	-	-	++	++	+	+
429	+++	+++					+++	+++	+
433	+++	+++					+	++	+
479	+++	+++			+++		++	++	-
543	+++			+++			++	-	-
545	+++					+++	-	++	-
607		+++		+++			++	-	++
703.73	+++						++	-	-
705				+++			++	-	-
763						+++	-	-	-

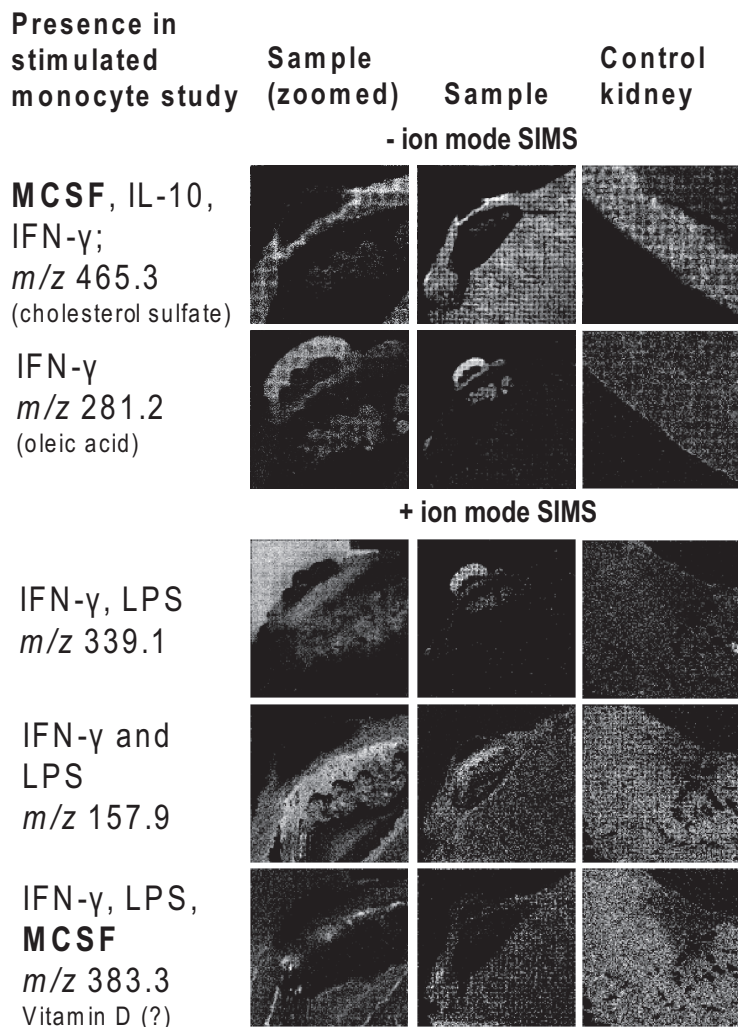


**Figure 7.9** Distribution at the gel implantation site of compounds that were found in the macrophage standards. The sample images show the same region with different magnification. The standards show bare kidney, showing the edge of the kidney, especially for the negative ion mode images.

#### 7.4 Discussion and outlook

This study has shown that TOF-SIMS is a technique with high potential for studying samples in which both synthetic polymers and biological activity play an important role. Both the polymer domain and the biological activity can be imaged in a single measurement using little or no sample preparation. Cellular infiltration was shown

in the polymer. This adds a novel dimension to the investigation of these types of samples. Issues like dissolving the polymer during immunohistochemical staining procedures, that often lead to a loss of the polymer are not faced when using TOF-SIMS. Therefore, direct evidence can be obtained on the presence of cells within the polymer hydrogel.

A distinction between macrophage polarizations was made by using different stimuli. This gave phenotype-specific peaks, but a reliable classification is so far not possible. To do this, a more extensive study is needed. To make a conclusive comparison with the implantation study, the use of rat macrophages instead of human macrophages is needed to exclude any species-specific differences<sup>260</sup>. Also a higher number of samples should be studied to get statistically reliable molecular profiles for each of the phenotypes. Complementing TOF-SIMS analysis with MALDI-TOF would give the data more confidence and make MS/MS based structural elucidation of the ions of interest possible. High mass resolution SIMS imaging using for instance a Fourier transform mass spectrometer (FTMS) as a mass analyzer could resolve molecules that have nominally the same mass and thus provide identification based on accurate mass measurement. This could further solidify the assignment of e.g. the sulfate and phosphate peaks.

Once a reliable profile for the different macrophage phenotypes is available, more definite observations can be made for the implantation samples. Recent developments in TOF-SIMS instrumentation<sup>5,6</sup>, allowing MS/MS analysis of TOF-SIMS generated ions can further solidify the assignment of the observed peaks. MALDI-TOF imaging can also contribute to the analysis of biological components but has the disadvantage of not being able to detect the polymer due to its high molecular weight and extensive supramolecular crosslinking. For biological molecules, MS/MS analysis using MALDI generated ions could however contribute to the complete understanding of the sample.

These results and the opportunities given for further research, show the enormous potential TOF-SIMS has in the analysis of implanted biomaterials. The advantage of not needing specific antibodies and being able to distinguish cellular, as well as synthetic components based on their molecular profile offers the opportunity to do explorative research on the foreign-body response and study the degradation of polymeric materials in-vivo. This adds a new dimension to biomaterials research, allowing access to a set of molecular information that cannot be obtained otherwise.





## BIBLIOGRAPHY

1. A.M. Piwowar, N.P. Lockyer and J.C. Vickerman, *Salt effects on ion formation in desorption mass spectrometry: An investigation into the role of alkali chlorides on peak suppression in time-of-flight-secondary ion mass spectrometry*. Analytical Chemistry, **2009**. 81(3): p. 1040-1048.
2. E.A. Jones, N.P. Lockyer, J. Kordys and J.C. Vickerman, *Suppression and Enhancement of Secondary Ion Formation Due to the Chemical Environment in Static-Secondary Ion Mass Spectrometry*. Journal of the American Society for Mass Spectrometry, **2007**. 18(8): p. 1559-1567.
3. R.M.A. Heeren, B. Kükrer-Kaletas, I.M. Taban, L. MacAleese and L.A. McDonnell, *Quality of surface: The influence of sample preparation on MS-based biomolecular tissue imaging with MALDI-MS and (ME-)SIMS*. Applied Surface Science, **2008**. 255(4): p. 1289-1297.
4. M. Stoeckli, D. Staab and A. Schweitzer, *Compound and metabolite distribution measured by MALDI mass spectrometric imaging in whole-body tissue sections*. International Journal of Mass Spectrometry; Imaging Mass Spectrometry Special Issue, **2007**. 260(2-3): p. 195-202.
5. P.D. Piehowski, A.J. Carado, M.E. Kurczy, S.G. Ostrowski, M.L. Heien, N. Winograd and A.G. Ewing, *MS/MS Methodology To Improve Subcellular Mapping of Cholesterol Using TOF-SIMS*. Analytical Chemistry, **2008**. 80(22): p. 8662-8667.
6. J.S. Fletcher, S. Rabbani, A. Henderson, P. Blenkinsopp, S.P. Thompson, N.P. Lockyer and J.C. Vickerman, *A New Dynamic in Mass Spectral Imaging of Single Biological Cells*. Analytical Chemistry, **2008**. 80(23): p. 9058-9064.
7. R.F.K. Herzog and F.P. Viehböck, *Ion Source for Mass Spectrography*. Physical Review, **1949**. 76(6): p. 855 LP - 856.
8. R.E. Honig, *Sputtering of Surfaces by Positive Ion Beams of Low Energy*. Journal of Applied Physics, **1958**. 29(3): p. 549-555.
9. J.C. Vickerman and D. Briggs, *ToF-SIMS: Surface Analysis by Mass Spectrometry*. **2001**: IM Publications and SurfaceSpectra Ltd.
10. P. Williams, R.K. Lewis, C.A. Evans and P.R. Hanley, *Evaluation of a cesium primary ion source on an ion microprobe mass spectrometer*. Analytical Chemistry, **1977**. 49(9): p. 1399-1403.
11. R.G. Forbest, *Understanding how the liquid-metal ion source works*. Vacuum, **1997**. 48(1): p. 85-97.
12. D. Briggs and M.J. Hearn, *Analysis of polymer surfaces by SIMS. Part 5. The effects of primary ion mass and energy on secondary ion relative intensities*. International Journal of Mass Spectrometry and Ion Processes, **1985**. 67(1): p. 47-56.
13. A.D. Appelhans and J.E. Delmore, *Comparison of polyatomic and atomic primary beams for secondary ion mass spectrometry of organics*. Analytical Chemistry, **1989**. 61(10): p. 1087-1093.
14. N. Davies, D.E. Weibel, P. Blenkinsopp, N. Lockyer, R. Hill and J.C. Vickerman, *Development and experimental application of a gold liquid metal ion source*. Applied Surface Science, **2003**. 203: p. 223-227.
15. T.C. Nguyen, D.W. Ward, J.A. Townes, A.K. White, K.D. Krantzman and B.J. Garrison, *A Theoretical Investigation of the Yield-to-Damage Enhancement with Polyatomic Projectiles in Organic SIMS*. Journal of Physical Chemistry B, **2000**. 104(34): p. 8221-8228.
16. B. Czerwinski, R. Samson, B.J. Garrison, N. Winograd and Z. Postawa, *Desorption of organic overlayers by Ga and C60 bombardment*. Vacuum, **2006**. 81(2): p. 167-173.
17. Z. Postawa, B. Czerwinski, N. Winograd and B.J. Garrison, *Microscopic insights into the sputtering of thin organic films on Ag{111} induced by C60 and Ga bombardment*. Journal of Physical Chemistry B, **2005**. 109(24): p. 11973-11979.

## Bibliography

18. Z. Postawa, *Sputtering simulations of organic overlayers on metal substrates by monoatomic and clusters projectiles*. Applied Surface Science, **2004**. 231-232: p. 22-28.
19. Z. Postawa, B. Czerwinski, M. Szweczyk, E.J. Smiley, N. Winograd and B.J. Garrison, *Enhancement of sputtering yields due to C60 versus Ga bombardment of Ag{111} as explored by molecular dynamics simulations*. Analytical Chemistry, **2003**. 75(17): p. 4402-4407.
20. R. Hill, R. Blenkinsopp, A. Barber and C. Everest, *The development of a range Of C-60 ion beam systems*. Applied Surface Science, **2006**. 252(19): p. 7304-7307.
21. J.S. Fletcher, X.A. Conlan, E.A. Jones, G. Biddulph, N.P. Lockyer and J.C. Vickerman, *TOF-SIMS analysis using C-60- effect of impact energy on yield and damage*. Analytical Chemistry, **2006**. 78(6): p. 1827-1831.
22. J. Cheng, J.Y. Xu, S.E. Martin, S. Dykstra, B.R. Peterson and N. Winograd, *Characterizing peptides on beads by ToF-SIMS with C60*. Abstracts of Papers of the American Chemical Society, **2004**. 228: p. 068-ANYL.
23. R. Hill and P.W.M. Blenkinsopp, *The development of C-60 and gold cluster ion guns for static SIMS analysis*. Applied Surface Science, **2004**. 231-2: p. 936-939.
24. D. Weibel, S. Wong, N. Lockyer, P. Blenkinsopp, R. Hill and J.C. Vickerman, *A C-60 primary ion beam system for time of flight secondary ion mass spectrometry: Its development and secondary ion yield characteristics*. Analytical Chemistry, **2003**. 75(7): p. 1754-1764.
25. S. Matt, B. Dunser, M. Lezius, H. Deutsch, K. Becker, A. Stamatovic, P. Scheier and T.D. Mark, *Absolute partial and total cross-section functions for the electron impact ionization of C[sub 60] and C[sub 70]*. The Journal of Chemical Physics, **1996**. 105(5): p. 1880-1896.
26. D.E. Weibel, N. Lockyer and J.C. Vickerman, *C60 cluster ion bombardment of organic surfaces*. Applied Surface Science, **2004**. 231-232: p. 146-152.
27. Z. Li, S.V. Verkhoturov, J.E. Locklear and E.A. Schweikert, *Secondary ion mass spectrometry with C-60(+) and Au-400(4+) projectiles: Depth and nature of secondary ion emission from multilayer assemblies*. International Journal of Mass Spectrometry, **2008**. 269(1-2): p. 112-117.
28. A. Tempez, J.A. Schultz, S. Della-Negra, J. Depauw, D. Jacquet, A. Novikov, Y. Lebeyec, M. Pautrat, M. Caroff, M. Ugarov, H. Bensaoula, M. Gonin, K. Fuhrer and A. Woods, *Orthogonal time-of-flight secondary ion mass spectrometric analysis of peptides using large gold clusters as primary ions*. Rapid Communications in Mass Spectrometry, **2004**. 18(4): p. 371-376.
29. L.A. Van Vaeck, Annemie; Gijbels, Renaat, *Static secondary ion mass spectrometry (S-SIMS) Part 1: methodology and structural interpretation*. Mass Spectrometry Reviews, **1999**. 18(1): p. 1-47.
30. A. Delcorte, P. Bertrand and B.J. Garrison, *Collision cascade and sputtering process in a polymer*. Journal of Physical Chemistry B, **2001**. 105(39): p. 9474-9486.
31. A. Delcorte and B.J. Garrison, *Particle-induced desorption of kilodalton molecules embedded in a matrix: A molecular dynamics study*. Journal of Physical Chemistry B, **2003**. 107(10): p. 2297-2310.
32. N. Winograd and B.J. Garrison, *Molecular desorption and secondary ion mass spectrometry*. International Journal of Mass Spectrometry, **2001**. 212(1-3): p. 467-475.
33. A. Delcorte and B.J. Garrison, *keV fullerene interaction with hydrocarbon targets: Projectile penetration, damage creation and removal*. Nuclear Instruments and Methods in Physics Research, Section B: Beam Interactions with Materials and Atoms, **2007**. 255(1): p. 223-228.
34. B. Czerwinski, L. Rzeznik, R. Paruch, B.J. Garrison and Z. Postawa, *Damage analysis of benzene induced by keV fullerene bombardment*. Nuclear Instruments and Methods in Physics Research, Section B: Beam Interactions with Materials and Atoms, **2009**. 267(8-9): p. 1440-1443.

35. K.D. Krantzman, Z. Postawa, B.J. Garrison, N. Winograd, S.J. Stuart and J.A. Harrison, *Understanding collision cascades in molecular solids*. Nuclear Instruments and Methods in Physics Research Section B: Beam Interactions with Materials and Atoms, **2001**. 180(1-4): p. 159-163.
36. S.C.C. Wong, N.P. Lockyer and J.C. Vickerman, *Mechanisms of secondary ion emission from self-assembled monolayers and multilayers*. Surface and Interface Analysis, **2005**. 37(9): p. 721-730.
37. Z. Postawa, K. Ludwig, J. Piaskowy, K. Krantzman, N. Winograd and B.J. Garrison, *Molecular dynamic simulations of the sputtering of multilayer organic systems*. Nuclear Instruments and Methods in Physics Research Section B: Beam Interactions with Materials and Atoms; 6th International Conference on Computer Simulation of Radiation, **2003**. 202: p. 168-174.
38. R. Mollers, N. Tuccitto, V. Torrisi, E. Niehuis and A. Licciardello, *Chemical effects in C-60 irradiation of polymers*. Applied Surface Science, **2006**. 252(19): p. 6509-6512.
39. I.S. Gilmore and M.P. Seah, *Electron flood gun damage in the analysis of polymers and organics in time-of-flight SIMS*. Applied Surface Science, **2002**. 187(1-2): p. 89-100.
40. K.J. Wu and R.W. Odom, *Matrix-enhanced secondary ion mass spectrometry: A method for molecular analysis of solid surfaces*. Analytical Chemistry, **1996**. 68(5): p. 873-882.
41. A.J. Nicola, D.C. Muddiman and D.M. Hercules, *Enhancement of ion intensity in time-of-flight secondary-ionization mass spectrometry*. Journal of the American Society for Mass Spectrometry, **1996**. 7(5): p. 467-472.
42. L. Adriaensen, F. Vangaeveer, J. Lenaerts and R. Gijbels, *Matrix-enhanced secondary ion mass spectrometry: the influence of MALDI matrices on molecular ion yields of thin organic films*. Rapid Communications in Mass Spectrometry, **2005**. 19(8): p. 1017-1024.
43. A.F. Altelaar, S.L. Luxembourg, L.A. McDonnell, S.R. Piersma and R.M. Heeren, *Imaging mass spectrometry at cellular length scales*. Nat Protoc, **2007**. 2(5): p. 1185-96.
44. S.L. Luxembourg and R.M.A. Heeren, *Fragmentation at and above surfaces in SIMS: Effects of biomolecular yield enhancing surface modifications*. International Journal of Mass Spectrometry, **2006**. 253(3): p. 181-192.
45. S.L. Luxembourg, L.A. McDonnell, M.C. Duursma, X.H. Guo and R.M.A. Heeren, *Effect of local matrix crystal variations in matrix-assisted ionization techniques for mass spectrometry*. Analytical Chemistry, **2003**. 75(10): p. 2333-2341.
46. J.F. Eloy, *Analyses chimiques semi-quantitatives par spectrographie de masse à ionisation par bombardement photonique (laser à rubis)*. International Journal of Mass Spectrometry and Ion Physics, **1971**. 6(1-2): p. 101-115.
47. M.A. Posthumus, *Laser desorption-mass spectrometry of polar nonvolatile bio-organic molecules*. Analytical Chemistry, **1978**. 50(7): p. 985-991.
48. F. Hillenkamp, E. Unsöld, R. Kaufmann and R. Nitsche, *Laser microprobe mass analysis of organic materials*. Nature, **1975**. 256(5513): p. 119-120.
49. M. Karas, D. Bachmann and F. Hillenkamp, *Influence of the wavelength in high-irradiance ultraviolet laser desorption mass spectrometry of organic molecules*. Analytical Chemistry, **1985**. 57(14): p. 2935-2939.
50. M. Karas, D. Bachmann, U. Bahr and F. Hillenkamp, *Matrix-assisted ultraviolet laser desorption of non-volatile compounds*. International Journal of Mass Spectrometry and Ion Processes, **1987**. 78: p. 53-68.
51. K. Dreisewerd, *The Desorption Process in MALDI*. Chem. Rev., **2003**. 103(2): p. 395-426.
52. R. Knochenmuss, *A bipolar rate equation model of MALDI primary and secondary ionization processes, with application to positive/negative analyte ion ratios and suppression effects*. International Journal of Mass Spectrometry, **2009**. 285(3): p. 105-113.

## Bibliography

53. W. Ens, Y. Mao, F. Mayer and K.G. Standing, *Properties of matrix-assisted laser desorption. Measurements with a time-to-digital converter*. Rapid Communications in Mass Spectrometry, **1991**. 5(3): p. 117-123.
54. X. Zhan and D.M. Desiderio, *MALDI-induced fragmentation of leucine enkephalin, nitro-Tyr-leucine enkephalin, and d5-Phe-nitro-Tyr-leucine enkephalin*. International Journal of Mass Spectrometry.
55. G. Luo, I. Marginean, L. Ye and A. Vertes, *Competing ion decomposition channels in matrix-assisted laser desorption ionization*. Journal of Physical Chemistry B, **2008**. 112(23): p. 6952-6956.
56. J.M. Campbell, M.L. Vestal, P.S. Blank, S.E. Stein, J.A. Epstein and A.L. Yergey, *Fragmentation of Leucine Enkephalin as a Function of Laser Fluence in a MALDI TOF-TOF*. Journal of the American Society for Mass Spectrometry, **2007**. 18(4): p. 607-616.
57. R.S. Brown, B.L. Carr and J.J. Lennon, *Factors that influence the observed fast fragmentation of peptides in matrix-assisted laser desorption*. Journal of the American Society for Mass Spectrometry, **1996**. 7(3): p. 225-232.
58. K. Dreisewerd, M. Schurenberg, M. Karas and F. Hillenkamp, *Influence of the Laser Intensity and Spot Size on the Desorption of Molecules and Ions in Matrix-Assisted Laser-Desorption Ionization with a Uniform Beam Profile*. International Journal of Mass Spectrometry and Ion Processes, **1995**. 141(2): p. 127-148.
59. E. Nordhoff, H. Lehrach and J. Gobom, *Exploring the limits and losses in MALDI sample preparation of attomole amounts of peptide mixtures*. International Journal of Mass Spectrometry, **2007**. 268(2-3): p. 139-146.
60. I. Garaguso and J. Borlak, *Matrix layer sample preparation: An improved MALDI-MS peptide analysis method for proteomic studies*. Proteomics, **2008**. 8(13): p. 2583-2595.
61. K. Dreisewerd, S. Berkenkamp, A. Leisner, A. Rohlfing and C. Menzel, *Fundamentals of matrix-assisted laser desorption/ionization mass spectrometry with pulsed infrared lasers*. International Journal of Mass Spectrometry, **2003**. 226(1): p. 189-209.
62. S. Berkenkamp, C. Menzel, M. Karas and F. Hillenkamp, *Performance of infrared matrix-assisted laser desorption/ionization mass spectrometry with lasers emitting in the 3  $\mu\text{m}$  wavelength range*. Rapid Communications in Mass Spectrometry, **1997**. 11(13): p. 1399-1406.
63. S. Berkenkamp, M. Karas and F. Hillenkamp, *Ice as a matrix for IR-matrix-assisted laser desorption/ionization: Mass spectra from a protein single crystal*. Proceedings of the National Academy of Sciences of the United States of America, **1996**. 93(14): p. 7003-7007.
64. R. Knochenmuss and L.V. Zhigilei, *Molecular Dynamics Model of Ultraviolet Matrix-Assisted Laser Desorption/Ionization Including Ionization Processes*. The Journal of Physical Chemistry B, **2005**. 109(48): p. 22947-22957.
65. F. Hillenkamp, E. Wafner, M.C. Jecklin and R. Zenobi, *Positive and negative analyte ion yield in matrix-assisted laser desorption/ionization revisited*. International Journal of Mass Spectrometry, **2009**. 285(3): p. 114-119.
66. G. Montaudo, F. Samperi and M.S. Montaudo, *Characterization of synthetic polymers by MALDI-MS*. Progress in Polymer Science, **2006**. 31(3): p. 277-357.
67. M.W.F. Nielen, *Maldi time-of-flight mass spectrometry of synthetic polymers*. Mass Spectrometry Reviews, **1999**. 18(5): p. 309-344.
68. A.J. Hotelling, W.J. Erb, R.J. Tyson and K.G. Owens, *Exploring the importance of the relative solubility of matrix and analyte in MALDI sample preparation using HPLC*. Analytical Chemistry, **2004**. 76(17): p. 5157-5164.
69. D.W. Armstrong, L.K. Zhang, L.F. He and M.L. Gross, *Ionic liquids as matrixes for matrix-assisted laser desorption/ionization mass spectrometry*. Analytical Chemistry, **2001**. 73(15): p. 3679-3686.

70. R. Lemaire, J.C. Tabet, P. Ducoroy, J.B. Hendra, M. Salzet and I. Fournier, *Solid ionic matrixes for direct tissue analysis and MALDI Imaging*. Analytical Chemistry, **2006**. 78(3): p. 809-819.
71. A.F.M. Altelaar, I. Klinkert, K. Jalink, R.P.J. de Lange, R.A.H. Adan, R.M.A. Heeren and S.R. Piersma, *Gold-enhanced biomolecular surface imaging of cells and tissue by SIMS and MALDI mass spectrometry*. Analytical Chemistry, **2006**. 78(3): p. 734-742.
72. A. Scherl, C.G. Zimmermann-Ivol, J. Di Dio, A.R. Vaezzadeh, P.-A. Binz, M. Amez-Droz, R. Cochard, J.-C. Sanchez, M. Glückmann and D.F. Hochstrasser, *Gold coating of non-conductive membranes before matrix-assisted laser desorption/ionization tandem mass spectrometric analysis prevents charging effect*. Rapid Communications in Mass Spectrometry, **2005**. 19(5): p. 605-610.
73. J.A. McLean, K.A. Stumpo and D.H. Russell, *Size-Selected (2 -10 nm) Gold Nanoparticles for Matrix Assisted Laser Desorption Ionization of Peptides*. Journal of the American Chemical Society, **2005**. 127(15): p. 5304-5305.
74. A. Tempez, M. Ugarov, T. Egan, J.A. Schultz, A. Novikov, S. Della-Negra, Y. Lebeyec, M. Pautrat, M. Caroff, V.S. Smentkowski, H.-Y.J. Wang, S.N. Jackson and A.S. Woods, *Matrix Implanted Laser Desorption Ionization (MILDI) Combined with Ion Mobility-Mass Spectrometry for Bio-Surface Analysis*. Journal of Proteome Research, **2005**. 4(2): p. 540-545.
75. A. Novikov, M. Caroff, S. Della-Negra, Y. Lebeyec, M. Pautrat, J.A. Schultz, A. Tempez, H.-Y.J. Wang, S.N. Jackson and A.S. Woods, *Matrix-Implanted Laser Desorption/Ionization Mass Spectrometry*. Analytical Chemistry, **2004**. 76(24): p. 7288-7293.
76. P. Lorkiewicz and M.C. Yappert, *Titanium microparticles and nanoparticles as matrixes for in vitro and in situ analysis of small molecules by MALDI-MS*. Analytical Chemistry, **2009**. 81(16): p. 6596-6603.
77. A.L. Castro, P.J. Amorim Madeira, M.R. Nunes, F.M. Costa and M.H. Florêncio, *Titanium dioxide anatase as matrix for matrix-assisted laser desorption/ionization analysis of small molecules*. Rapid Communications in Mass Spectrometry, **2008**. 22(23): p. 3761-3766.
78. S. Trimpin, A. Rouhanipour, R. Az, H.J. Räder and K. Müllen, *New aspects in matrix-assisted laser desorption/ionization time-of-flight mass spectrometry: A universal solvent-free sample preparation*. Rapid Communications in Mass Spectrometry, **2001**. 15(15): p. 1364-1373.
79. A. Marie, F. Fournier and J.C. Tabet, *Characterization of synthetic polymers by MALDI-TOF/MS: Investigation into new methods of sample target preparation and consequence on mass spectrum finger print*. Analytical Chemistry, **2000**. 72(20): p. 5106-5114.
80. L. Przybilla, J.-D. Brand, K. Yoshimura, H.J. Räder and K. Müllen, *MALDI-TOF mass spectrometry of insoluble giant polycyclic aromatic hydrocarbons by a new method of sample preparation*. Analytical Chemistry, **2000**. 72(19): p. 4591-4597.
81. R. Skelton, F. Dubois and R. Zenobi, *A MALDI sample preparation method suitable for insoluble polymers*. Analytical Chemistry, **2000**. 72(7): p. 1707-1710.
82. S.D. Hanton and D.M. Parees, *Extending the solvent-free MALDI sample preparation method*. Journal of the American Society for Mass Spectrometry, **2005**. 16(1): p. 90-93.
83. Z. Takáts, J.M. Wiseman, B. Gologan and R.G. Cooks, *Mass spectrometry sampling under ambient conditions with desorption electrospray ionization*. Science, **2004**. 306(5695): p. 471-473.
84. K. Hiraoka, K. Mori and D. Asakawa, *Fundamental aspects of electrospray droplet impact/SIMS*. Journal of Mass Spectrometry, **2006**. 41(7): p. 894-902.
85. C.L. Brummel, K.F. Willey, J.C. Vickerman and N. Winograd, *Ion beam induced desorption with postionization using high repetition femtosecond lasers*. International Journal of Mass Spectrometry and Ion Processes, **1995**. 143(C): p. 257-270.
86. M. Wood, Y. Zhou, C.L. Brummel and N. Winograd, *Imaging with ion beams and laser postionization*. Analytical Chemistry, **1994**. 66(15): p. 2425-2430.

## Bibliography

87. D. Lipinsky, R. Jede, J. Tuempner, O. Ganschow and A. Benninghoven, *Electron beam impact postionization of sputtered neutrals*. Surface and Interface Analysis, **1986**. 9(1-6): p. 73.
88. J.S. Sampson, A.M. Hawkrigde and D.C. Muddiman, *Direct characterization of intact polypeptides by matrix-assisted laser desorption electrospray ionization quadrupole Fourier transform ion cyclotron resonance mass spectrometry*. Rapid Communications in Mass Spectrometry, **2007**. 21(7): p. 1150-1154.
89. J.S. Sampson, A.M. Hawkrigde and D.C. Muddiman, *Generation and Detection of Multiply-Charged Peptides and Proteins by Matrix-Assisted Laser Desorption Electrospray Ionization (MALDESI) Fourier Transform Ion Cyclotron Resonance Mass Spectrometry*. Journal of the American Society for Mass Spectrometry, **2006**. 17(12): p. 1712-1716.
90. J.S. Sampson and D.C. Muddiman, *Atmospheric pressure infrared (10.6 micrometer) laser desorption electrospray ionization (IR-LDESI) coupled to a LTQ Fourier transform ion cyclotron resonance mass spectrometer*. Rapid Communications in Mass Spectrometry, **2009**. 23(13): p. 1989-1992.
91. I.X. Peng, J. Shiea, R.R.O. Loo and J.A. Loo, *Electrospray-assisted laser desorption/ionization and tandem mass spectrometry of peptides and proteins*. Rapid Communications in Mass Spectrometry, **2007**. 21(16): p. 2541-2546.
92. J. Shiea, M.-Z. Huang, H.-J. Hsu, C.-Y. Lee, C.-H. Yuan, I. Beech and J. Sunner, *Electrospray-assisted laser desorption/ionization mass spectrometry for direct ambient analysis of solids*. Rapid Communications in Mass Spectrometry, **2005**. 19(24): p. 3701-3704.
93. M.-Z. Huang, H.-J. Hsu, J.-Y. Lee, J. Jeng and J. Shiea, *Direct protein detection from biological media through electrospray-assisted laser desorption ionization/mass spectrometry*. Journal of Proteome Research, **2006**. 5(5): p. 1107-1116.
94. P. Nemes and A. Vertes, *Laser Ablation Electrospray Ionization for Atmospheric Pressure, in Vivo, and Imaging Mass Spectrometry*. Anal. Chem., **2007**. 79(21): p. 8098-8106.
95. A. Leisner, A. Rohlfing, S. Berkenkamp, F. Hillenkamp and K. Dreisewerd, *Infrared laser post-ionization of large biomolecules from an IR-MALD(I) plume*. Journal of the American Society for Mass Spectrometry, **2004**. 15(6): p. 934-941.
96. J.H. Futrell, ed. *Gaseous ion chemistry and mass spectrometry*. **1986**, Wiley-Interscience: New York. 335.
97. W.E. Stephens, *Proceedings of the American Physical Society*. Physical Review, **1946**. 69(11-12): p. 691.
98. Takekiyo Matsuo, Michisato Toyoda, Toru Sakurai and Morio Ishihara, *Ion optics for multi-turn time-of-flight mass spectrometers with variable mass resolution*. Journal of Mass Spectrometry, **1997**. 32(11): p. 1179-1185.
99. M.B. Comisarow and A.G. Marshall, *Fourier transform ion cyclotron resonance spectroscopy*. Chemical Physics Letters, **1974**. 25(2): p. 282-283.
100. A.G. Marshall, C.L. Hendrickson and G.S. Jackson, *Fourier transform ion cyclotron resonance mass spectrometry: A primer*. Mass Spectrometry Reviews, **1998**. 17(1): p. 1-35.
101. I.M. Taban, A.F.M. Altelaar, Y.E.M. van der Burgt, L.A. McDonnell, R.M.A. Heeren, J. Fuchser and G. Baykut, *Imaging of Peptides in the Rat Brain Using MALDI-FTICR Mass Spectrometry*. Journal of the American Society for Mass Spectrometry, **2007**. 18(1): p. 145-151.
102. K.K. Kutz, J.J. Schmidt and L. Li, *In Situ Tissue Analysis of Neuropeptides by MALDI FTMS In-Cell Accumulation*. Analytical Chemistry, **2004**. 76(19): p. 5630 LP - 5640.
103. J.C. Jurchen, S.S. Rubakhin and J.V. Sweedler, *MALDI-MS imaging of features smaller than the size of the laser beam*. Journal of the American Society for Mass Spectrometry, **2005**. 16(10): p. 1654-1659.

104. S.L. Luxembourg, *Mass Microscopy: Imaging Biomolecules on Surfaces*, PhD thesis, Faculty of Chemistry. **2005**. Utrecht, Utrecht University.
105. B.W. Schueler, *Microscope Imaging by Time-of-Flight Secondary Ion Mass-Spectrometry*. *Microscopy Microanalysis Microstructures*, **1992**. 3(2-3): p. 119-139.
106. B. Schueler, P. Sander and D.A. Reed, *A Time-of-Flight Secondary Ion-Microscope*. *Vacuum*, **1990**. 41(7-9): p. 1661-1664.
107. S.L. Luxembourg, T.H. Mize, L.A. McDonnell and R.M.A. Heeren, *High-Spatial Resolution Mass Spectrometric Imaging of Peptide and Protein Distributions on a Surface*. *Analytical Chemistry*, **2004**. 76(18): p. 5339-5344.
108. L.A. McDonnell, T.H. Mize, S.L. Luxembourg, S. Koster, G.B. Eijkel, E. Verpoorte, N.F. de Rooij and R.M.A. Heeren, *Using matrix peaks to map topography: Increased mass resolution and enhanced sensitivity in chemical imaging*. *Analytical Chemistry*, **2003**. 75(17): p. 4373-4381.
109. R. Lemaire, M. Wisztorski, A. Desmons, J.C. Tabet, R. Day, M. Salzet and I. Fournier, *MALDI-MS Direct Tissue Analysis of Proteins: Improving Signal Sensitivity Using Organic Treatments*. *Analytical Chemistry*, **2006**. 78(20): p. 7145-7153.
110. E.H. Seeley, S.R. Oppenheimer, D. Mi, P. Chaurand and R.M. Caprioli, *Enhancement of Protein Sensitivity for MALDI Imaging Mass Spectrometry After Chemical Treatment of Tissue Sections*. *Journal of the American Society for Mass Spectrometry*, **2008**. 19(8): p. 1069-1077.
111. B.K. Kaletas, I.M. van der Wiel, J. Stauber, L.J. Dekker, C. Guzel, J.M. Kros, T.M. Luider and R.M.A. Heeren, *Sample preparation issues for tissue imaging by imaging MS*. *Proteomics*, **2009**. 9(10): p. 2622-2633.
112. M. Stoeckli, D. Staab and S. Capretta, *Automated Matrix Deposition for MALDI MSI*. at 54th ASMS Conference on Mass Spectrometry and Allied Topics. **2006**. Seattle, WA: ASMS.
113. Jan Axelsson, Anne-Mette Hoberg, Carl Waterson, Paul Myatt, Gary L. Shield, Julie Varney, David M. Haddleton and Peter J. Derrick, *Improved Reproducibility and Increased Signal Intensity in Matrix-assisted Laser Desorption/Ionization as a Result of Electrospray Sample Preparation*. *Rapid Communications in Mass Spectrometry*, **1997**. 11(2): p. 209-213.
114. S.M. Puolitaival, K.E. Burnum, D.S. Cornett and R.M. Caprioli, *Solvent-Free Matrix Dry-Coating for MALDI Imaging of Phospholipids*. *Journal of the American Society for Mass Spectrometry*, **2008**. 19(6): p. 882-886.
115. J.A. Hankin, R.M. Barkley and R.C. Murphy, *Sublimation as a Method of Matrix Application for Mass Spectrometric Imaging*. *Journal of the American Society for Mass Spectrometry*, **2007**. 18(9): p. 1646-1652.
116. A. Delcorte, J. Bour, F. Aubriet, J.F. Muller and P. Bertrand, *Sample metallization for performance improvement in desorption/ionization of kilodalton molecules: Quantitative evaluation, imaging secondary ion MS, and laser ablation*. *Analytical Chemistry*, **2003**. 75(24): p. 6875-6885.
117. A. Delcorte and P. Bertrand, *Interest of silver and gold metallization for molecular SIMS and SIMS imaging*. *Applied Surface Science*, **2004**. 231-232: p. 250-255.
118. A. Delcorte, N. Medard and P. Bertrand, *Organic secondary ion mass spectrometry: Sensitivity enhancement by gold deposition*. *Analytical Chemistry*, **2002**. 74(19): p. 4955-4968.
119. A. Delcorte, S. Yunus, N. Wehbe, N. Nieuwjaer, C. Poleunis, A. Felten, L. Houssiau, J.J. Pireaux and P. Bertrand, *Metal-assisted secondary ion mass spectrometry using atomic (Ga<sup>+</sup>, In<sup>+</sup>) and fullerene projectiles*. *Analytical Chemistry*, **2007**. 79(10): p. 3673-3689.
120. R.W. Linton, M.P. Mawn, A.M. Belu, J.M. DeSimone, M.O. Hunt Jr., Y.Z. Menciloglu, H.G. Cramer and A. Benninghoven, *Time-of-flight secondary ion mass spectrometric analysis of polymer surfaces and additives*. *Surface and Interface Analysis*, **1993**. 20(12): p. 991-999.

## Bibliography

121. L.A. McDonnell, R.M.A. Heeren, R.P.J. de Lange and I.W. Fletcher, *Higher Sensitivity Secondary Ion Mass Spectrometry of Biological Molecules for High Resolution, Chemically Specific Imaging*. Journal of the American Society for Mass Spectrometry, **2006**. 17(9): p. 1195-1202.
122. K. Keune and J. J. Boon, *Enhancement of the static SIMS secondary ion yields of lipid moieties by ultrathin gold coating of aged oil paint surfaces*. Surface and Interface Analysis, **2004**. 36(13): p. 1620-1628.
123. L. Adriaensen, F. Vangaever and R. Gijbels, *Metal-Assisted Secondary Ion Mass Spectrometry: Influence of Ag and Au Deposition on Molecular Ion Yields*. Analytical Chemistry, **2004**. 76(22): p. 6777-6785.
124. A. Delcorte, J. Bour, F. Aubriet, J.-F. Muller and P. Bertrand, *Sample Metallization for Performance Improvement in Desorption/Ionization of Kilodalton Molecules: Quantitative Evaluation, Imaging Secondary Ion MS, and Laser Ablation*. Analytical Chemistry, **2003**. 75(24): p. 6875-6885.
125. A.F.M. Altelaar, I.M. Taban, L.A. McDonnell, P.D.E.M. Verhaert, R.P.J. de Lange, R.A.H. Adan, W.J. Mooi, R.M.A. Heeren and S.R. Piersma, *High-resolution MALDI imaging mass spectrometry allows localization of peptide distributions at cellular length scales in pituitary tissue sections*. International Journal of Mass Spectrometry, **2007**. 260(2-3): p. 203-211.
126. R. Knochenmuss, *Photoionization Pathways and Free Electrons in UV-MALDI*. Analytical Chemistry, **2004**. 76(11): p. 3179-3184.
127. G.Y. Li and J.L. Koenig, *FTIR imaging of oxidation of polyisoprene 2. The role of N-phenyl-N'-dimethyl-butyl-p-phenylenediamine antioxidant*. Polymer Degradation and Stability, **2003**. 81(3): p. 377-385.
128. R. Bhargava, S.Q. Wang and J.L. Koenig, *FTIR microspectroscopy of polymeric systems*. Advances in Polymer Science, **2003**. 163: p. 137-191.
129. J. van der Weerd, A. van Loon and J.J. Boon, *FTIR studies of the effects of pigments on the aging of oil*. Studies in Conservation, **2005**. 50(1): p. 3-22.
130. J. van der Weerd, H. Brammer, J.J. Boon and R.M.A. Heeren, *Fourier transform infrared microscopic imaging of an embedded paint cross-section*. Applied Spectroscopy, **2002**. 56(3): p. 275-283.
131. I.W. Levin and R. Bhargava, *Fourier transform infrared vibrational spectroscopic imaging: Integrating microscopy and molecular recognition*. Annual Review of Physical Chemistry, **2005**. 56: p. 429-474.
132. N.J. Everall, *Depth Profiling With Confocal Raman Microscopy, Part I*. Spectroscopy, **2004**. 19(10): p. 22 - 27.
133. N. Everall, *Depth Profiling With Confocal Raman Microscopy, Part II*. Spectroscopy, **2004**. 19(11): p. 16 - 24.
134. B.T. Wickes, Y. Kim and D.G. Castner, *Denoising and multivariate analysis of time-of-flight SIMS images*. Surface and Interface Analysis, **2003**. 35(8): p. 640-648.
135. A. Broersen, *Feature Visualization in Large Scale Imaging Mass Spectrometry Data*, PhD thesis. **2009**. Eindhoven, Eindhoven University of Technology.
136. A. Broersen, R. van Liere and R.M.A. Heeren, *Comparing three PCA-based Methods for the 3D Visualization of Imaging Spectroscopy Data*. at IASTED International Conference on Visualization, Imaging, & Image Processing. **2005**. Benidorm, Spain.
137. C. Bruuning, S. Hellweg, S. Dambach, D. Lipinsky and H.F. Arlinghaus, *Improving the interpretation of ToF-SIMS measurements on adsorbed proteins using PCA*. Surface and Interface Analysis, **2006**. 38(4): p. 191-193.
138. R. Bro and A.K. Smilde, *Centering and scaling in component analysis*. Journal of Chemometrics, **2003**. 17(1): p. 16-33.



139. D.J. Graham and B.D. Ratner, *Multivariate analysis of TOF-SIMS spectra from dodecanethiol SAM assembly on gold: Spectral interpretation and TOF-SIMS fragmentation processes*. *Langmuir*, **2002**. 18(15): p. 5861-5868.
140. M.R. Keenan and P.G. Kotula, *Accounting for Poisson noise in the multivariate analysis of ToF-SIMS spectrum images*. *Surface and Interface Analysis*, **2004**. 36(3): p. 203-212.
141. M.L. Pacholski, *Principal component analysis of TOF-SIMS spectra, images and depth profiles: an industrial perspective*. *Applied Surface Science*, **2004**. 231-2: p. 235-239.
142. S. Rangarajan and B.J. Tyler, *Interpretation of static time-of-flight ion mass spectral images of adsorbed protein films on topographically complex surfaces*. *Applied Surface Science*, **2004**. 231-2: p. 406-410.
143. B. Tyler, *Interpretation of TOF-SIMS images: multivariate and univariate approaches to image de-noising, image segmentation and compound identification*. *Applied Surface Science*, **2003**. 203: p. 825-831.
144. M.S. Wagner, B.J. Tyler and D.G. Castner, *Interpretation of static time-of-flight secondary ion mass spectra of adsorbed protein films by multivariate pattern recognition*. *Analytical Chemistry*, **2002**. 74(8): p. 1824-1835.
145. M.S. Wagner, D.J. Graham, B.D. Ratner and D.G. Castner, *Maximizing information obtained from secondary ion mass spectra of organic thin films using multivariate analysis*. *Surface Science*, **2004**. 570(1-2): p. 78-97.
146. L. Yang, Y.Y. Lua, G.L. Jiang, B.J. Tyler and M.R. Linford, *Multivariate analysis of TOF-SIMS spectra of monolayers on scribed silicon*. *Analytical Chemistry*, **2005**. 77(14): p. 4654-4661.
147. M.C. Biesinger, P.Y. Paepegaey, N.S. McIntyre, R.R. Harbottle and N.O. Petersent, *Principal component analysis of TOF-SIMS images of organic monolayers*. *Analytical Chemistry*, **2002**. 74(22): p. 5711-5716.
148. B.J. Tyler, G. Rayal and D.G. Castner, *Multivariate analysis strategies for processing ToF-SIMS images of biomaterials*. *Biomaterials*, **2007**. 28(15): p. 2412-2423.
149. M. Hanselmann, M. Kirchner, B.Y. Renard, E.R. Amstalden, K. Glunde, R.M.A. Heeren and F.A. Hamprecht, *Concise Representation of Mass Spectrometry Images by Probabilistic Latent Semantic Analysis*. *Analytical Chemistry*, **2008**. 80(24): p. 9649-9658.
150. L.A. Klerk, A. Broersen, I.W. Fletcher, R. van Liere and R.M.A. Heeren, *Extended data analysis strategies for high resolution imaging MS: New methods to deal with extremely large image hyperspectral datasets*. *International Journal of Mass Spectrometry; Imaging Mass Spectrometry Special Issue*, **2007**. 260(2-3): p. 222-236.
151. G.B. Eijkel, B.K. Kaletas, I.M. Van Der Wiel, J.M. Kros, T.M. Luider and R.M.A. Heeren, *Correlating MALDI and SIMS imaging mass spectrometric datasets of biological tissue surfaces*. *Surface and Interface Analysis*, **2009**. 41(8): p. 675-685.
152. A.T. Jackson, A. Bunn, L.R. Hutchings, F.T. Kiff, R.W. Richards, J. Williams, M.R. Green and R.H. Bateman, *The generation of end group information from poly(styrene)s by means of matrix-assisted laser desorption/ionisation-collision induced dissociation*. *Polymer*, **2000**. 41(20): p. 7437-7450.
153. S.D. Hanton, *New mass spectrometry techniques for the analysis of polymers for coatings applications: MALDI and ESI*. *JCT CoatingsTech*, **2004**. 1(1): p. 62-68.
154. S.D. Hanton, *Mass spectrometry of polymers and polymer surfaces*. *Chemical Reviews*, **2001**. 101(2): p. 527-569.
155. R.P. Lattimer, *Pyrolysis mass spectrometry of acrylic acid polymers*. *Journal of Analytical and Applied Pyrolysis*, **2003**. 68-69: p. 3-14.
156. R. Rial-Otero, M. Galesio, J.-L. Capelo and J. Simal-Gándara, *A review of synthetic polymer characterization by pyrolysis-GC-MS*. *Chromatographia*, **2009**. 70(3-4): p. 339-348.

## Bibliography

157. S.J. Wetzel, C.M. Guttman, K.M. Flynn and J.J. Filliben, *Significant parameters in the optimization of MALDI-TOF-MS for synthetic polymers*. Journal of the American Society for Mass Spectrometry, **2006**. 17(2): p. 246-252.
158. S.F. Macha and P.A. Limbach, *Matrix-assisted laser desorption/ionization (MALDI) mass spectrometry of polymers*. Current Opinion in Solid State & Materials Science, **2002**. 6(3): p. 213-220.
159. G. Montaudo, F. Samperi, M.S. Montaudo, S. Carroccio and C. Puglisi, *Current trends in matrix-assisted laser desorption/ionization of polymeric materials*. European Journal of Mass Spectrometry, **2005**. 11(1): p. 1-14.
160. A.T. Jackson, H.T. Yates, W.A. MacDonald, J.H. Scrivens, G. Critchley, J. Brown, M.J. Deery, K.R. Jennings and C. Brookes, *Time-lag focusing and cation attachment in the analysis of synthetic polymers by matrix-assisted laser desorption/ionization-time-of-flight-mass spectrometry*. Journal of the American Society for Mass Spectrometry, **1997**. 8(2): p. 132-139.
161. T. Yalcin, Y.Q. Dai and L. Li, *Matrix-assisted laser desorption/ionization time-of-flight mass spectrometry for polymer analysis: Solvent effect in sample preparation*. Journal of the American Society for Mass Spectrometry, **1998**. 9(12): p. 1303-1310.
162. S. Trimpin, S. Keune, H.J. Räder and K. Müllen, *Solvent-Free MALDI-MS: Developmental Improvements in the Reliability and the Potential of MALDI in the Analysis of Synthetic Polymers and Giant Organic Molecules*. Journal of the American Society for Mass Spectrometry, **2006**. 17(5): p. 661-671.
163. M. Nefliu, A. Venter and R.G. Cooks, *Desorption electrospray ionization and electrosonic spray ionization for solid- and solution-phase analysis of industrial polymers*. Chemical Communications, **2006**(8): p. 888-890.
164. A.T. Jackson, J.P. Williams and J.H. Scrivens, *Desorption electrospray ionisation mass spectrometry and tandem mass spectrometry of low molecular weight synthetic polymers*. Rapid Communications in Mass Spectrometry, **2006**. 20(18): p. 2717-2727.
165. R.M. Braun, J. Cheng, E.E. Parsonage, J. Moeller and N. Winograd, *Surface and depth profiling investigation of a drug-loaded copolymer utilized to coat Taxus Express(2) stents*. Analytical Chemistry, **2006**. 78(24): p. 8347-8353.
166. A.G. Shard, M.C. Davies, S.J.B. Tendler, D.E. Jackson, P.N. Lan, E. Schacht and M.D. Purbrick, *Surface Organization of Polyurethanes Observed by Static Secondary-Ion Mass-Spectrometry*. Polymer, **1995**. 36(4): p. 775-779.
167. M.P. Chiarelli, A. Proctor, I.V. Bletsos, D.M. Hercules, H. Feld, A. Leute and A. Benninghoven, *High-Resolution ToF-Sims Studies of Substituted Polystyrenes*. Macromolecules, **1992**. 25(25): p. 6970-6976.
168. J.G. Newman, B.A. Carlson, R.S. Michael, J.F. Moulder and T.A. Hohlt, *Static SIMS handbook of polymer analysis*. **1991**, Eden Prairie, MN: Perkin-Elmer Corporation, Physical Electronics division.
169. S.D. Hanton and K.G. Owens, *Using MESIMS to analyze polymer MALDI matrix solubility*. Journal of the American Society for Mass Spectrometry, **2005**. 16(7): p. 1172-1180.
170. S.D. Hanton, P.A.C. Clark and K.G. Owens, *Investigations of matrix-assisted laser desorption/ionization sample preparation by time-of-flight secondary ion mass spectrometry*. Journal of the American Society for Mass Spectrometry, **1999**. 10(2): p. 104-111.
171. S.D. Hanton, I.Z. Hyder, J.R. Stets, K.G. Owens, W.R. Blair, C.M. Guttman and A.A. Giuseppetti, *Investigations of electrospray sample deposition for polymer MALDI mass spectrometry*. Journal of the American Society for Mass Spectrometry, **2004**. 15(2): p. 168-179.

172. A.T. Jackson, J.H. Scrivens, J.P. Williams, E.S. Baker, J. Gidden and M.T. Bowers, *Microstructural and conformational studies of polyether copolymers*. International Journal of Mass Spectrometry, **2004**. 238(3): p. 287-297.
173. S. Roberson, A. Sehgal, A. Fahey and A. Karim, *Time-of-flight secondary ion mass spectrometry (TOF-SIMS) for high-throughput characterization of biosurfaces*. Applied Surface Science, **2003**. 203-204: p. 855-858.
174. A.M. Piwowar and J.A. Gardella, *Time-of-Flight Secondary Ion Mass Spectrometric Analysis of Polymer Tertiary Structure in Langmuir Monolayer Films of Poly(dimethylsiloxane)*. Anal. Chem., **2007**. 79(11): p. 4126-4134.
175. L.T. Weng and C.M. Chan, *SSIMS analysis of organics, polymer blends and interfaces*. Applied Surface Science, **2006**. 252(19): p. 6570-6574.
176. I.L. Bolotin, S.H. Tetzler and L. Hanley, *Sputtering yields of PMMA films bombarded by keV C60+ ions*. Applied Surface Science, **2006**. 252(19): p. 6533-6536.
177. S.J. Hinder, J.F. Watts and C. Lowe, *Surface and interface analysis of complex polymeric paint formulations*. Surface and Interface Analysis, **2006**. 38(4): p. 557-560.
178. S.L. McArthur, M.S. Wagner, P.G. Hartley, K.M. McLean, H.J. Griesser and D.G. Castner, *Characterization of sequentially grafted polysaccharide coatings using time-of-flight secondary ion mass spectrometry (ToF-SIMS) and principal component analysis (PCA)*. Surface and Interface Analysis, **2002**. 33(12): p. 924-931.
179. K. Keune and J.J. Boon, *Enhancement of the static SIMS secondary ion yields of lipid moieties by ultrathin gold coating of aged oil paint surfaces*. Surface and Interface Analysis, **2004**. 36(13): p. 1620-1628.
180. S.R. Bryan, A.M. Belu, T. Hoshi and R. Oiwa, *Evaluation of a gold LMIG for detecting small molecules in a polymer matrix by ToF-SIMS*. Applied Surface Science, **2004**. 231-232: p. 201-206.
181. C.M. Mahoney, J.X. Yu, A. Fahey and J.A. Gardella, *SIMS depth profiling of polymer blends with protein based drugs*. Applied Surface Science, **2006**. 252(19): p. 6609-6614.
182. C.A. Prestidge, T.J. Barnes and W. Skinner, *Time-of-flight secondary-ion mass spectrometry for the surface characterization of solid-state pharmaceuticals*. Journal of Pharmacy and Pharmacology, **2007**. 59(2): p. 251-259.
183. C.M. Mahoney and A.J. Fahey, *Three-dimensional compositional analysis of drug eluting stent coatings using cluster secondary ion mass spectrometry*. Analytical Chemistry, **2008**. 80(3): p. 624-632.
184. J.Y. Xu, R.M. Braun and N. Winograd, *Rapid screening of molecular arrays using imaging TOF-SIMS*. Applied Surface Science, **2003**. 203: p. 201-204.
185. J.Y. Feng, L. Li, C.M. Chan and L.T. Weng, *Inter-diffusion between PMMA and PVDF during lamination studied by time-of-flight secondary ion mass spectrometry chemical imaging*. Surface and Interface Analysis, **2002**. 33(5): p. 455-458.
186. K. Thalassinou, A.T. Jackson, J.P. Williams, G.R. Hilton, S.E. Slade and J.H. Scrivens, *Novel Software for the Assignment of Peaks from Tandem Mass Spectrometry Spectra of Synthetic Polymers*. Journal of the American Society for Mass Spectrometry, **2007**. 18(7): p. 1324-1331.
187. F. Hillenkamp, M. Karas, R.C. Beavis and B.T. Chait, *Matrix-Assisted Laser Desorption Ionization Mass-Spectrometry of Biopolymers*. Analytical Chemistry, **1991**. 63(24): p. A1193-A1202.
188. B. Stahl, A. Linos, M. Karas, F. Hillenkamp and M. Steup, *Analysis of fructans from higher plants by matrix-assisted laser desorption/ionization mass spectrometry*. Analytical Biochemistry, **1997**. 246(2): p. 195-204.
189. C.G. Dekoster, M.C. Duursma, G.J. Vanrooij, R.M.A. Heeren and J.J. Boon, *Endgroup Analysis of Polyethylene-Glycol Polymers by Matrix-Assisted Laser-Desorption Ionization Fourier-Transform Ion-*

## Bibliography

- Cyclotron Resonance Mass-Spectrometry*. Rapid Communications in Mass Spectrometry, **1995**. 9(10): p. 957-962.
190. H.J. Griesser, P. Kingshott, S.L. McArthur, K.M. McLean, G.R. Kinsel and R.B.R.B. Timmons, *Surface-MALDI mass spectrometry in biomaterials research*. Biomaterials, **2004**. 25(20): p. 4861-4875.
191. J. Godovac-Zimmermann and L.R. Brown, *Perspectives for mass spectrometry and functional proteomics*. Mass Spectrometry Reviews, **2001**. 20(1): p. 1-57.
192. L.A. McDonnell and R.M.A. Heeren, *Imaging mass spectrometry*. Mass Spectrometry Reviews, **2007**. 26(4): p. 606-643.
193. D.S. Cornett, M.L. Reyzer, P. Chaurand and R.M. Caprioli, *MALDI imaging mass spectrometry: molecular snapshots of biochemical systems*. Nature Methods, **2007**. 4(10): p. 828-833.
194. S. Khatib-Shahidi, M. Andersson, J.L. Herman, T.A. Gillespie and R.M. Caprioli, *Direct molecular analysis of whole-body animal tissue sections by imaging MALDI mass spectrometry*. Analytical Chemistry, **2006**. 78(18): p. 6448-6456.
195. L.A. McDonnell, S.R. Piersma, A.F.M. Altelaar, T.H. Mize, S.L. Luxembourg, P.D.E.M. Verhaert, J. van Minnen and R.M.A. Heeren, *Subcellular imaging mass spectrometry of brain tissue*. Journal of Mass Spectrometry, **2005**. 40(2): p. 160-168.
196. B. Spengler and M. Hubert, *Scanning microprobe matrix-assisted laser desorption ionization (SMALDI) mass spectrometry: instrumentation for sub-micrometer resolved LDI and MALDI surface analysis*. Journal of the American Society for Mass Spectrometry, **2002**. 13(6): p. 735-748.
197. A. Ingendoh, M. Karas, F. Killenkamp and U. Giessmann, *Factors Affecting the Resolution in Matrix-Assisted Laser-Desorption Ionization Mass-Spectrometry*. International Journal of Mass Spectrometry and Ion Processes, **1994**. 131: p. 345-354.
198. I. Klinkert, L.A. McDonnell, S.L. Luxembourg, A.F.M. Altelaar, E.R. Amstalden, S.R. Piersma and R.M.A. Heeren, *Tools and strategies for visualization of large image data sets in high-resolution imaging mass spectrometry*. Review of Scientific Instruments, **2007**. 78(5): p. 053716-(1-10).
199. R. Meier and P. Eberhardt, *Velocity and ion species dependence of the gain of microchannel plates*. International Journal of Mass Spectrometry and Ion Processes, **1993**. 123(1): p. 19-27.
200. A. Delcorte, *Matrix-enhanced secondary ion mass spectrometry: The Alchemist's solution?* Applied Surface Science, **2006**. 252(19): p. 6582-6587.
201. A. Brunelle, D. Touboul and O. Lapr evote, *Biological tissue imaging with time-of-flight secondary ion mass spectrometry and cluster ion sources*. Journal of Mass Spectrometry, **2005**. 40(8): p. 985-999.
202. H.H. Andersen and H.L. Bay, *Nonlinear effects in heavy-ion sputtering*. Journal of Applied Physics, **1974**. 45(2): p. 953-954.
203. M. Benguerba, A. Brunelle, S. Della-Negra, J. Depauw, H. Joret, Y. Le Beyec, M.G. Blain, E.A. Schweikert, G.B. Assayag and P. Sudraud, *Impact of slow gold clusters on various solids: nonlinear effects in secondary ion emission*. Nuclear Inst. and Methods in Physics Research, B, **1991**. 62(1): p. 8-22.
204. D. Touboul, F. Halgand, A. Brunelle, R. Kersting, E. Tallarek, B. Hagenhoff and O. Lapr evote, *Tissue Molecular Ion Imaging by Gold Cluster Ion Bombardment*. Analytical Chemistry, **2004**. 76(6): p. 1550-1559.
205. D. Touboul, F. Kollmer, E. Niehuis, A. Brunelle and O. Lapr evote, *Improvement of biological time-of-flight-secondary ion mass spectrometry imaging with a bismuth cluster ion source*. Journal of the American Society for Mass Spectrometry, **2005**. 16(10): p. 1608-1618.

206. E.A. Jones, N.P. Lockyer and J.C. Vickerman, *Mass spectral analysis and imaging of tissue by ToF-SIMS--The role of buckminsterfullerene, C60+, primary ions*. International Journal of Mass Spectrometry; Imaging Mass Spectrometry Special Issue, **2007**. 260(2-3): p. 146-157.
207. M.J. Baker, J.S. Fletcher, H. Jungnickel, N.P. Lockyer and J.C. Vickerman, *A comparative study of secondary ion yield from model biological membranes using Au-n(+) and C-60(+) primary ion sources*. Applied Surface Science, **2006**. 252(19): p. 6731-6733.
208. R. De Mondt, L. Van Vaeck, A. Heile, H.F. Arlinghaus, N. Nieuwjaer, A. Delcorte, P. Bertrand, J. Lenaerts and F. Vangaever, *Ion yield improvement for static secondary ion mass spectrometry by use of polyatomic primary ions*. Rapid Communications in Mass Spectrometry, **2008**. 22(10): p. 1481-1496.
209. P. Sjövall, J. Lausmaa and B. Johansson, *Mass spectrometric imaging of lipids in brain tissue*. Analytical Chemistry, **2004**. 76(15): p. 4271-4278.
210. K.E. Ryan, I.A. Wojciechowski and B.J. Garrison, *Reaction dynamics following keV cluster bombardment*. Journal of Physical Chemistry C, **2007**. 111(34): p. 12822-12826.
211. J. Cheng, J. Kozole, R. Hengstebeck and N. Winograd, *Direct Comparison of Au3+ and C60+ Cluster Projectiles in SIMS Molecular Depth Profiling*. Journal of the American Society for Mass Spectrometry, **2007**. 18(3): p. 406-412.
212. F. Kötter and A. Benninghoven, *Secondary ion emission from polymer surfaces under Ar+, Xe+ and SF5+ ion bombardment*. Applied Surface Science, **1998**. 133(1-2): p. 47-57.
213. A. Benninghoven, D. Jaspers and W. Sichtermann, *Secondary-ion emission of amino acids*. Applied Physics, **1976**. 11(1): p. 35-39.
214. J.S. Fletcher, N.P. Lockyer and J.C. Vickerman, Mass Spec. Rev. in press.
215. A. Delcorte, *On the road to high-resolution 3D molecular imaging*. Applied Surface Science; Proceedings of the Sixteenth International Conference on Secondary Ion Mass Spectrometry, SIMS XVI, **2008**. 255(4): p. 954-958.
216. J.S. Fletcher, N.P. Lockyer and J.C. Vickerman, *C-60, buckminsterfullerene: its impact on biological ToF-SIMS analysis*. Surface and Interface Analysis, **2006**. 38(11): p. 1393-1400.
217. M. Froesch, A. Kharchenko, S.L. Luxembourg, D. Verheijde and R.M.A. Heeren, *Imaging mass spectrometry using a delay line detector*. European Journal of Mass Spectrometry, **2009**. Accepted.
218. A. Oelsner, O. Schmidt, M. Schicketanz, M. Klais, G. Schonhense, V. Mergel, O. Jagutzki and H. Schmidt-Bocking, *Microspectroscopy and imaging using a delay line detector in time-of-flight photoemission microscopy*. Review of Scientific Instruments, **2001**. 72(10): p. 3968-3974.
219. I.S. Gilmore and M.P. Seah, *Ion detection efficiency in SIMS: Dependencies on energy, mass and composition for microchannel plates used in mass spectrometry*. International Journal of Mass Spectrometry, **2000**. 202(1-3): p. 217-229.
220. O. Jagutzki, V. Mergel, K. Ullmann-Pfleger, L. Spielberger, U. Spillmann, R. Dorner and H. Schmidt-Bocking, *A broad-application microchannel-plate detector system for advanced particle or photon detection tasks: large area imaging, precise multi-hit timing information and high detection rate*. Nuclear Instruments & Methods in Physics Research Section a-Accelerators Spectrometers Detectors and Associated Equipment, **2002**. 477(1-3): p. 244-249.
221. O. Jagutzki, A. Cerezo, A. Czasch, R. Dorner, M. Hattass, M. Huang, V. Mergel, U. Spillmann, K. Ullmann-Pfleger, T. Weber, H. Schmidt-Bocking and G.D.W. Smith, *Multiple hit readout of a microchannel plate detector with a three-layer delay-line anode*. Ieee Transactions on Nuclear Science, **2002**. 49(5): p. 2477-2483.

## Bibliography

222. R.P. Sijbesma, F.H. Beijer, L. Brunsveld, B.J.B. Folmer, J.H.K.K. Hirschberg, R.F.M. Lange, J.K.L. Lowe and E.W. Meijer, *Reversible polymers formed from self-complementary monomers using quadruple hydrogen bonding*. *Science*, **1997**. 278(5343): p. 1601-1604.
223. P.Y.W. Dankers, E.N.M. van Leeuwen, G.M.L. van Gemert, A.J.H. Spiering, M.C. Harmsen, L.A. Brouwer, H.M. Janssen, A.W. Bosman, M.J.A. van Luyn and E.W. Meijer, *Chemical and biological properties of supramolecular polymer systems based on oligocaprolactones*. *Biomaterials*, **2006**. 27(32): p. 5490-5501.
224. P.Y.W. Dankers, M.C. Harmsen, L.A. Brouwer, M.J.A. Van Luyn and E.W. Meijer, *A modular and supramolecular approach to bioactive scaffolds for tissue engineering*. *Nature Materials*, **2005**. 4(7): p. 568-574.
225. L.A. Klerk, A.F.M. Altelaar, M. Froesch, L.A. McDonnell and R.M.A. Heeren, *Fast and automated large-area imaging MALDI mass spectrometry in microprobe and microscope mode*. *International Journal of Mass Spectrometry*, **2009**. 285(1-2): p. 19-26.
226. K.R. Thorp and L.F. Tian, *A Review on Remote Sensing of Weeds in Agriculture*. *Precision Agriculture*, **2004**. 5(5): p. 477-508.
227. J.M. Piwowar and E.F. LeDrew, *Hypertemporal analysis of remotely sensed sea ice data for climate change studies*. *Progress in Physical Geography*, **1995**. 19(2): p. 216-242.
228. B.H.P. Maathuis and J.L. van Genderen, *A review of satellite and airborne sensors for remote sensing based detection of minefields and landmines*. *International Journal of Remote Sensing*, **2004**. 25(23): p. 5201 - 5245.
229. N.J. Everall, J.M. Chalmers, L.H. Kidder, E.N. Lewis, M. Schaeberle and I. Levin, *Mapping and imaging orientation, crystallinity, and chemical composition in polymer articles using IR and Raman microscopies*. *Abstracts of Papers of the American Chemical Society*, **2000**. 219: p. U502-U502.
230. N.J. Everall, *Raman spectroscopy coatings research and analysis: Part I. Basic principles*. *Jct Coatingstech*, **2005**. 2(19): p. 38-44.
231. P.J. Todd, T.G. Schaaff, P. Chaurand and R.M. Caprioli, *Organic ion imaging of biological tissue with secondary ion mass spectrometry and matrix-assisted laser desorption/ionization*. *Journal of Mass Spectrometry*, **2001**. 36(4): p. 355-369.
232. A.M. Belu, D.J. Graham and D.G. Castner, *Time-of-flight secondary ion mass spectrometry: techniques and applications for the characterization of biomaterial surfaces*. *Biomaterials*, **2003**. 24(21): p. 3635-3653.
233. R.R. Meglen, *Examining Large Databases - a Chemometric Approach Using Principal Component Analysis*. *Marine Chemistry*, **1992**. 39(1-3): p. 217-237.
234. V.S. Smentkowski, J.A. Ohlhausen, P.G. Kotula and M.R. Keenan, *Multivariate statistical analysis of time-of-flight secondary ion mass spectrometry images-looking beyond the obvious*. *Applied Surface Science*, **2004**. 231-2: p. 245-249.
235. G. McCombie, D. Staab, M. Stoeckli and R. Knochenmuss, *Spatial and spectral correlations in MALDI mass spectrometry images by clustering and multivariate analysis*. *Analytical Chemistry*, **2005**. 77(19): p. 6118-6124.
236. A. Broersen, R. Van Liere and R.M.A. Heeren, *Zooming in multi-spectral datacubes using PCA*. at *Proceedings of SPIE - The International Society for Optical Engineering*. **2008**.
237. M.R. Keenan and P.G. Kotula, *Optimal scaling of TOF-SIMS spectrum-images prior to multivariate statistical analysis*. *Applied Surface Science*, **2004**. 231-2: p. 240-244.
238. M.R. Keenan, *Maximum likelihood principal component analysis of time-of-flight secondary ion mass spectrometry spectral images*. *Journal of Vacuum Science & Technology A*, **2005**. 23(4): p. 746-750.

239. I.T. Jolliffe, *Principal Component Analysis*. 2 ed. Springer series in statistics. **2002**: Springer-Verlag.
240. R.B. Lehoucq, D.C. Sorensen and C. Yang, *ARPACK Users' Guide: Solution of Large-Scale Eigenvalue Problems with Implicitly Restarted Arnoldi Methods*. **1998**, Philadelphia: SIAM Publications.
241. D.C. Sorensen, *Implicit Application of Polynomial Filters in a K-Step Arnoldi Method*. Siam Journal on Matrix Analysis and Applications, **1992**. 13(1): p. 357-385.
242. H.F. Kaiser, *The varimax criterion for analytic rotation in factor analysis*. at Psychometrika. **1958**.
243. R.A. Harshman, *Foundations of the PARAFAC procedure: Models and conditions for an explanatory multimodal factor analysis*. at UCLA Working Papers in Phonetics. **1970**.
244. J.D. Carroll and J.J. Chang, *Analysis of Individual Differences in Multidimensional scaling via an N-way generalization of Eckart-Young decomposition*. at Psychometrika. **1970**.
245. R. Bro, *PARAFAC, tutorial and applications*. at Chemometrics and Intelligent Laboratory Systems. **1997**.
246. A. Broersen and R. van Lieere, *Transfer Functions for Imaging Spectroscopy Data using Principle Component Analysis*. **2005**. Eurographics / IEEE VGTC Symposium on Visualization.
247. B.D. Ratner, A.S. Hoffmann, F.J. Schoen and J.E. Lemons, eds. *Biomaterials science: an introduction to materials in medicine*. **1996**, Academic Press: San Diego, CA. 484.
248. P.Y.W. Dankers, A. Huizinga-van der Vlag, G. M.L van Gemert, A.H. Petersen, E.W. Meijer, H.M. Janssen, A.W. Bosman, M.J.A. van Luyn and E.R. Popa, *Foreign body response to novel supramolecular hydrogels for renal drug delivery*. To be submitted, **2009**.
249. S.W. Kim, Y.H. Bae and T. Okano, *Hydrogels: Swelling, drug loading, and release*. Pharmaceutical Research, **1992**. 9(3): p. 283-290.
250. S. Parry and N. Winograd, *High-Resolution TOF-SIMS Imaging of Eukaryotic Cells Preserved in a Trehalose Matrix*. Analytical Chemistry, **2005**. 77(24): p. 7950-7957.
251. S.A. Parry, M.E. Kurczy, X. Fan, M.S. Halleck, R.A. Schlegel and N. Winograd, *Imaging macrophages in trehalose with SIMS*. Applied Surface Science; Proceedings of the Sixteenth International Conference on Secondary Ion Mass Spectrometry, SIMS XVI, **2008**. 255(4): p. 929-933.
252. J.S. Fletcher, N.P. Lockyer, S. Vaidyanathan and J.C. Vickerman, *TOF-SIMS 3D biomolecular imaging of Xenopus laevis oocytes using buckminsterfullerene (C-60) primary ions*. Analytical Chemistry, **2007**. 79(6): p. 2199-2206.
253. J.-W. Lee and J.A. Gardella, *Simultaneous Time-of-Flight Secondary Ion MS Quantitative Analysis of Drug Surface Concentration and Polymer Degradation Kinetics in Biodegradable Poly(L-lactic acid) Blends*. Anal. Chem., **2003**. 75(13): p. 2950-2958.
254. A. Mantovani, A. Sica and M. Locati, *New vistas on macrophage differentiation and activation*. Eur J Immunol, **2007**. 37(1): p. 14-6.
255. D.M. Mosser and J.P. Edwards, *Exploring the full spectrum of macrophage activation*. Nat Rev Immunol, **2008**. 8(12): p. 958-69.
256. M. Iwamori, H.W. Moser and Y. Kishimoto, *Cholesterol sulfate in rat tissues. Tissue distribution, developmental change and brain subcellular localization*. Biochim Biophys Acta, **1976**. 441(2): p. 268-79.
257. C.A. Strott and Y. Higashi, *Cholesterol sulfate in human physiology: what's it all about?* J. Lipid Res., **2003**. 44(7): p. 1268-1278.
258. W.W. Christie, *The lipid library*;. **2009**, Scottish Crop Research Institute.

## Bibliography

259. D. Touboul, S. Roy, D.P. Germain, P. Chaminade, A. Brunelle and O. Lapr evote, *MALDI-TOF and cluster-TOF-SIMS imaging of Fabry disease biomarkers*. International Journal of Mass Spectrometry; Imaging Mass Spectrometry Special Issue, **2007**. 260(2-3): p. 158-165.
260. D. Strauss-Ayali, S.M. Conrad and D.M. Mosser, *Monocyte subpopulations and their differentiation patterns during infection*. Journal of Leukocyte Biology, **2007**. 82(2): p. 244-252.



## SUMMARY

Polymers play an important role in everyday life. Over the past century, the application of polymeric materials has increased to virtually any type of consumer products, medical devices, pharmaceuticals, adhesives and coatings. In the development and engineering of increasingly complex polymer systems, it is of great importance to understand both their spatial and molecular properties. Knowledge of the composition and organization of polymer mixtures and microsystems is important to understand their functioning and failure. Imaging mass spectrometry (MS) is a technique that provides spatial information based on the molecular weight of materials. In this way, domains in a polymeric system can be differentiated based on their molecular composition.

In short, imaging mass spectrometry is a technique that makes images of molecular distributions at surfaces based on mass spectral information. At a range (typically a raster) of positions, a mass spectrum is measured from the surface. This mass spectrum is a characteristic fingerprint for the material that is present at the position analyzed. By selecting a peak from the spectrum that is specific for a certain compound, a distribution map of this compound can be made for all positions at the surface. To determine the mass of molecules in an imaging experiment, they are brought into the gas phase and ionized using a laser or ion beam. The mass of these ions is subsequently determined in a mass analyzer.

**Chapter 2** gives a general description of the mass spectrometric techniques that are used in imaging MS as well as several methodologies needed for the successful application of imaging MS. For a successful imaging MS experiment, various steps have to be performed and optimized for each different sample type. Sample preparation is a key issue in imaging MS because it largely determines which molecules are detected from the sample and which ones are not, and how these molecules will present themselves in the mass spectra. In the second step the surface material is brought into the gas phase and ionized. In this thesis, two major techniques are used for this purpose, the choice of which depends on the anticipated information. Laser desorption and ionization (LDI), uses a laser for ion generation. The surface is often coated with a light-absorbing matrix coating to assist the desorption and ionization process, in which case it is named matrix assisted LDI (MALDI). In secondary ion mass spectrometry (SIMS) an ion beam is used to generate ions from the surface. MALDI typically provides intact molecules for mass analysis. SIMS provides few intact molecular ions and a substantial amount of fragment ions. These fragment ions are specific for the structure of the original molecule and can therefore provide structural information. Once the surface

material is brought into vacuum and ionized, the mass analysis takes place. There are many methods for mass analysis, but the most commonly used method for imaging MS is time-of-flight (TOF) mass spectrometry, which was also used for this work. After data acquisition, the data needs to be analyzed in order to convert the peaks in the spectra and the distribution they show at the surface into meaningful information. Manual exploration gives direct insight in the acquired data. Because of the high complexity of this data however, automated analysis like for instance principal component analysis (PCA) is helpful. PCA makes correlations between different compounds insightful. For instance it shows which compounds tend to co-localize at the surface, giving an idea on their correlated biological activity, common origin in a production process or their common origin as fragments from a single compound. Methods of analyzing these correlations are discussed in **chapter 6**. An overview of three different methods: PCA, PCA with VARIMAX optimization and PARAFAC, is given. Their performances on different datasets as well as the computation time needed for analysis are compared. It is shown that different samples may need different approaches and there should always be a trade-off made between analysis time and performance. Memory limitations are a major issue when performing statistical analysis on large datasets. The nature of imaging MS datasets, especially when analyzed at high spectral resolution, is that they are very sparse due to the many empty (zero) values between the peaks. The use of sparse-type data storage and processing increases the maximum amount of data that can be used for statistical analysis and moreover speeds up the analysis.

Showing correlation between peaks in the mass spectrum is of special importance when imaging polymer systems, which is one of the key messages of **chapter 3**. Because polymers are built up from a chain of monomers, which leads to a variety of polymer chain lengths, polymers show up in a mass spectrum as a collection of peaks with a slightly different mass. A single peak of this distribution can be so small that it is hardly seen in the total image spectrum, especially when only a small part of the imaged area contains polymer. By using the natural correlation between these peaks, a molecular weight distribution can nevertheless be obtained and the distribution of the polymer can be visualized with sufficient image intensity. **Chapter 3** discusses some more possibilities and challenges that are faced in the mass spectrometric imaging of polymers. SIMS has an established position as an imaging technique. MALDI however has only been widely applied for bulk polymer analysis whereas MALDI imaging applications are generally limited to biological studies. The widespread application of MALDI as an imaging MS technique is challenged mainly by sample preparation. Solvent choice considerations are a main challenge in sample preparation because the choice of solvent determines which component is extracted

from a surface. Differences in physical properties between different copolymer compositions as well as polymer chain length variations can cause a biased result when not considered carefully because of their differences in solubility and diffusion behaviour.

Just like any other imaging technique, there is an ever-lasting interest in seeing more detail. In the most common type of imaging MS experiment, the surface is scanned with a focused microprobe beam. Therefore, the image resolution is determined by the spot size of the ionization beam (the laser or ion beam). Obviously, decreasing the beam diameter will improve the spatial resolution of the experiment. It does however also lead to an exponential increase in data acquisition time (doubling the resolution quadruples the number of acquisition points and hence the acquisition time). Moreover, the MALDI process becomes less efficient at very small spot size and for some primary ion beams used in SIMS, there is a limit to the focusing diameter at which the source is still bright enough to get useful signal. These issues are discussed in **chapters 4 and 5**. By using a microscope approach rather than a microprobe approach these problems can be largely circumvented. A microscope mass spectrometer makes use of ion optics that are designed to project a direct ion optical image of the sample onto a position sensitive detector, similar to how it is done in an optical microscope. In this manner, the image resolution is no longer dependant on the ionization beam diameter but rather on the quality of the ion optics and the detector. This means that irrespectively the diameter of the ionization beam, the same image resolution is obtained. **Chapter 4** shows how this method can be applied for selected mass imaging and how these images can be recorded in an automated way with no image size constraints. It also shows how microprobe data can be recorded at the same time as microscope images, making correlations between spectral features and microscopic images possible. **Chapter 5** introduces a novel detector for microscope mode imaging mass spectrometry. This delay-line detector records both the mass and the position of each single ion and therefore, for the first time, provides a full set of mass spectral images in the microscope mode. It is shown for  $C_{60}$  primary ions that this increases both contrast and resolution in a SIMS imaging experiment, which is explained by the limited focusing capabilities that are inherent to  $C_{60}$  sources and the larger area that can be analyzed at once, at a higher  $C_{60}$  current. The use of software tools makes it possible to stitch together a mosaic of these microscope mode imaging datasets, taking away any image size constraint.

Finally all these subjects come together and are applied on a sample that combines biological and polymeric features in **chapter 7**. The biomedical engineering field is an important and fast-growing application field for polymeric materials. Polymers

## Summary

can for instance be used as carriers for controlled drug delivery. To engineer polymer products for biomedical use, it is important to have a thorough understanding of the response of the body on the polymer and the response of a polymer on the body. In this example, a biodegradable polymer is implanted under the capsule of a rat kidney. The simultaneous analysis of both polymer material and biological activity shows the power of MS imaging to chemically analyze diverse samples. This provides molecular cartography of the polymer implant as well as the cellular signature of the implantation environment in one single experiment. Cellular infiltration into the polymer is visualized based on cellular molecular signatures. Because it is known that macrophages play an important role in the foreign body response, the molecular signatures are compared with macrophage standards cultured in different polarization environments. Based on this comparison, an assessment can be made on which type of macrophages localize in which region around the implantation site. This is an example of how modern imaging MS methodologies are exploited for the analysis of both polymeric and biological systems at the same time. As such, it shows the applicability of most of the techniques and methodologies discussed in this thesis.

## SAMENVATTING

Polymeren spelen een belangrijke rol in het dagelijkse leven. Gedurende de afgelopen eeuw is de toepassing van polymere materialen (kunststoffen) zodanig toegenomen dat ze worden gebruikt in vrijwel alle soorten consumentenproducten, medische apparaten, geneesmiddelen, lijmen en coatings. Bij het ontwerp en de ontwikkeling van polymeersystemen met steeds grotere complexiteit, is kennis van zowel de ruimtelijke als de moleculaire eigenschappen daarvan van groot belang. Kennis van de samenstelling en ruimtelijke structuur van polymeermengsels en microsystemen zijn belangrijk om hun werking te begrijpen en als ze niet werken zoals bedoeld is, dit te begrijpen en te verbeteren. Plaatsopgeloste massaspectrometrie (MS) is een techniek die ruimtelijke informatie geeft op basis van moleculaire informatie. Hierdoor kunnen verschillende gedeelten van een materiaal onderscheiden worden op basis van hun moleculaire samenstelling.

Kort gezegd is plaatsopgeloste MS een techniek die moleculaire verdelingen op een oppervlak inzichtelijk maakt op basis van massaspectrometrische informatie. Op een raster van posities wordt een massaspectrum gemeten vanaf het oppervlak. Dit massaspectrum is karakteristiek voor het materiaal dat zich op die positie bevindt. Door nu een piek in het massaspectrum te selecteren die specifiek is voor een bepaalde stof, kan voor deze stof op elke positie op het oppervlak de hoeveelheid bepaald worden. Door die hoeveelheid uit te beelden in een intensiteitsplaatje wordt de verdeling van die stof op het oppervlak in kaart gebracht. Om de massa van moleculen te bepalen moeten deze in de gasfase worden gebracht en worden geïoniseerd. Dit gebeurt meestal met een ionenbundel of met behulp van laserlicht. Hierna wordt de massa van deze ionen gemeten in een massaspectrometer. Door de massa van de moleculen die op het oppervlak aanwezig zijn te meten, wordt informatie verkregen over welke stoffen dit zijn, omdat de molecuulmassa één van de karakteristieke eigenschappen van een stof is.

**Hoofdstuk 2** geeft een algemene beschrijving van de massaspectrometrische technieken die voor plaatsopgeloste MS worden gebruikt. Daarnaast wordt een overzicht gegeven van de methoden die nodig zijn om plaatsopgeloste MS toe te passen. Verschillende stappen zijn cruciaal voor het succes van een analyse. Ten eerste moeten de te meten monsters dusdanig voorbereid worden dat ze goed te meten zijn. De manier waarop monsters voorbereid worden bepaalt in grote mate welke moleculen worden waargenomen in de massaspectrometer. De tweede stap is het in gas fase brengen (desorberen) en ioniseren van de moleculen op het oppervlak. In deze dissertatie wordt voornamelijk gebruik gemaakt van twee technieken. Bij laserdesorptie en -ionisatie (LDI) wordt een laser gebruikt om ionen vrij te maken

van het oppervlak. Vaak wordt een oppervlak eerst met een matrix van een lichtabsorberend molecuul bedekt, dat helpt bij het in gasfase brengen en ioniseren van de moleculen. Men spreekt dan van Matrix geAssisteerde LDI (MALDI). Bij secundaire ionen massaspectrometrie (SIMS) worden ionen met behulp van een ionenbundel gegenereerd. MALDI resulteert met name in geïoniseerde intacte moleculen. SIMS kan intacte moleculen opleveren, maar geeft in ieder geval ook fragmenten van moleculen. Deze fragmenten zijn specifiek voor het molecuul en kunnen dus structuurinformatie geven. Vervolgens wordt de massa van de geïoniseerde moleculen gemeten. Dit wordt in dit proefschrift in de meeste gevallen gedaan via een “time-of-flight” (TOF), ofwel vluchttijd bepaling. Na de meting moeten de gegevens worden omgezet in zinvolle informatie. Dit kan door direct naar de gegevens te kijken, maar dat is niet altijd de handigste methode vanwege de enorme complexiteit en de enorme hoeveelheid meetgegevens. Om de gegevens inzichtelijker te maken, kunnen geautomatiseerde methoden gebruikt worden zoals bijvoorbeeld principale componenten analyse (PCA). PCA is een wiskundige methode die verbanden legt binnen de gegevens. Op die manier geeft het een overzicht van welke stoffen op dezelfde plek op het oppervlak aanwezig zijn en welke stoffen vaak tegelijkertijd aanwezig zijn op een bepaalde positie. De gemeten ionen kunnen bijvoorbeeld, in geval van een plaatsopgeloste MS meting aan biologisch weefsel, een gezamenlijke biologische betekenis hebben, of het kunnen fragmenten zijn van een bepaald molecuul. Methoden om deze verbanden te vinden worden behandeld in **hoofdstuk 6**. Er wordt daar een overzicht gegeven van drie verschillende methoden: PCA, PCA met VARIMAX optimalisatie en PARAFAC. De kwaliteit van resultaten van deze verschillende methoden wordt vergeleken, maar ook de analysetijd wordt in ogenschouw genomen. Hieruit blijkt dat soms per monster verschillende methoden tot het beste resultaat leiden en dat er veelal een afweging moet worden gemaakt tussen rekentijd en kwaliteit van de analyse. Geheugenbeperkingen in de gebruikte computers vormen soms ook een probleem. Aangezien in plaatsopgeloste massaspectrometriemetingen nogal veel “nullen” voorkomen wordt voor een implementatie van de rekenmethoden gekozen waarbij deze nullen uit de gegevens worden weggelaten. Hierdoor kunnen grotere hoeveelheden meetgegevens worden geanalyseerd kunnen de analyses bovendien sneller uitgevoerd worden.

Wanneer polymeersystemen worden bekeken, is het vinden van correlaties in de gegevens extra belangrijk. Dit is één van de belangrijkste boodschappen van **hoofdstuk 3**. Omdat polymeren opgebouwd zijn uit ketens van monomeren, wat tijdens de synthese leidt tot een variatie in ketenlengte, geven polymeren in een massaspectrum een verzameling van pieken met een iets verschillende waarde. Een

enkele piek in zo'n verdeling is vaak zo weinig intens dat hij gemakkelijk over het hoofd kan worden gezien in het spectrum van het totale monster, vooral als maar een klein stukje van het oppervlak uit polymeer bestaat. Door de correlatie tussen deze pieken te vinden kan de volledige moleculaire massaverdeling worden verkregen en kan bovendien de totale intensiteit van deze pieken gebruikt worden om het uiteindelijke beeld te vormen. **Hoofdstuk 3** reikt verder mogelijkheden aan om de specifieke uitdagingen aan te pakken waarmee plaatsopgeloste massaspectrometrie van polymeersystemen gepaard gaat. SIMS heeft een gevestigde positie als analysemethode voor polymeren. MALDI wordt echter alleen grootschalig gebruikt bij het analyseren van polymeren in bulk, terwijl plaatsopgeloste MALDI experimenten zich veelal beperken tot biologische systemen. De grootste uitdaging om MALDI als plaatsopgeloste techniek toe te passen ligt in de monstervoorbereiding. Met name de keuze van het oplosmiddel tijdens het coaten van het oppervlak met matrix is van groot belang, omdat het oplosmiddel in grote mate bepaalt welke stoffen uit het oppervlak worden geëxtraheerd en dus uiteindelijk kunnen worden gemeten. Verschillen in fysische eigenschappen tussen verschillende samenstellingen van copolymeren en polymeerketenlengtes kunnen leiden tot een vertekend beeld in het uiteindelijke resultaat omdat sommige moleculen zich beter uit een oppervlak laten extraheren dan andere.

Zoals bij alle technieken waarin beelden worden gemaakt, is er aldoor de vraag naar hogere resolutie om meer detail te kunnen zien. De meest gebruikelijke manier om plaatsopgeloste massaspectrometrie te doen, is via een microprobe-techniek, waarbij het oppervlak wordt gescand met een gefocuste laser of ionenbundel. De beeldresolutie wordt hier dan ook bepaald door de diameter van de gebruikte bundel. Dit betekent ook dat wanneer de bundel tot een kleinere diameter wordt gefocust, er een hogere beeldresolutie verkregen kan worden. Een hogere resolutie leidt echter onvermijdelijk tot een exponentiële toename van de meettijd (een verdubbeling van de resolutie leidt tot een verviervoudiging van het aantal pixels, en dus meetposities). Bovendien neemt de efficiëntie van het MALDI proces af naarmate de laserbundel kleiner wordt en is het voor sommige soorten ionenbronnen die in SIMS worden gebruikt moeilijk om deze tot een kleine diameter te focuseren. **Hoofdstukken 4 en 5** gaan daar verder op in en bieden hiervoor oplossingen. Door een microscoop-benadering te kiezen worden deze problemen omzeild. Een massamicroscoop, maakt gebruik van ionenoptiek die ontworpen is om een directe projectie van het gemeten oppervlak te maken op de detector, vergelijkbaar met hoe dit gebeurt in een optische microscoop. Door dit te doen is de beeldresolutie niet afhankelijk van de diameter van de ionisatie-bundel, maar van de kwaliteit van de ionenoptiek en van de detector. Dit betekent dat, onafhankelijk van

de diameter van de ionisatie-bundel, altijd dezelfde beeldresolutie behaald wordt. **Hoofdstuk 4** laat zien hoe deze methode kan worden toegepast als een bepaalde massa wordt geselecteerd en hoe deze beelden op een geautomatiseerde manier kunnen worden verkregen zonder last te hebben van een beperkt blikveld. Het laat ook zien hoe tegelijkertijd microprobe-spectra en microscoopbeelden kunnen worden verkregen, waardoor correlaties kunnen worden gezien tussen spectrale informatie en de microscoopbeelden. **Hoofdstuk 5** introduceert een nieuw soort detector voor plaatsopgeloste massaspectrometrie in de microscoopmodus. Met deze "delay-line" detector kunnen, voor het eerst, zowel de massa als de positie van elk ion gemeten worden. SIMS experimenten, waarbij fullereen ( $C_{60}$ ) wordt gebruikt als primair ion tonen aan dat met deze aanpak zowel het contrast als de beeldresolutie verbetert. Dit komt doordat  $C_{60}$  een moeilijk te focuseren bron is en door het grotere gebied dat in één keer in kaart kan worden gebracht bij een hogere  $C_{60}$  intensiteit. Door speciale programmatuur te gebruiken kan een mozaïek van dit soort metingen aan elkaar worden gezet, waardoor ook grote oppervlakken kunnen worden gemeten.

Tenslotte komen al deze aspecten samen en worden deze in **hoofdstuk 7** toegepast op een monster dat bestaat uit zowel biologisch weefsel als polymeer. De biomedische technologie is een belangrijk toepassingsveld van polymere materialen. Polymeren kunnen bijvoorbeeld gebruikt worden als drager in een afgiftesysteem voor geneesmiddelen. Om polymeren voor geneeskundig gebruik te ontwikkelen, is het belangrijk om goed inzicht te hebben in de reactie van het lichaam op het polymeer en de reactie van het polymeer op het lichaam. In dit specifieke geval, wordt een polymeer geïmplanteerd onder het kapsel van een rattennier. De gelijktijdige analyse van zowel het polymeer als het omliggende weefsel geeft een uniek beeld waarin tegelijkertijd zowel het synthetische als het biologische systeem te zien zijn. Op deze manier worden zowel het polymeer als het omliggende weefsel in kaart gebracht op basis van hun moleculaire samenstelling. Hierbij is infiltratie van cellen in het polymeer te zien op basis van de moleculen die specifiek zijn voor die bepaalde cellen. Omdat bekend is dat macrofagen een belangrijke rol spelen in de reactie van een lichaam op een geïmplanteerd materiaal, wordt ook een vergelijking gemaakt met macrofaagstandaarden die in een celcultuur zijn gekweekt. Door de moleculaire profielen van de gekweekte cellen en van de cellen in de implantatie studie te vergelijken, kan een inschatting worden gemaakt van het soort cellen dat rond de plek van implantatie te zien is. Dit laatste hoofdstuk laat zien hoe moderne plaatsopgeloste MS technieken gebruikt kunnen worden om tegelijkertijd biologische systemen en polymeersystemen in beeld te brengen en laat op die manier de toepasbaarheid zien van de meesten van de in dit proefschrift beschreven technieken.



## DANKWOORD

Het is bijzonder dat de meest gelezen pagina's van een proefschrift niet meetellen in de beoordeling van een promotie. En het is niet voor niets dat precies deze pagina's het dankwoord bevatten. Een promotie kun je niet alleen en het is daarom van niet te onderschatten belang waardering uit te spreken richting de mensen die hun bijdrage hebben geleverd aan het tot stand komen van dit proefschrift. Een promotie is tenslotte gebaseerd op het werk van de promovendus met de onmisbare hulp en inspiratie van een groep mensen.

Als eerste wil ik daarom mijn promotor Ron Heeren bedanken. Ron, je hebt me veel vertrouwen gegeven en de vrijheid om nieuwe wegen in te slaan. Daarnaast was je er met je enthousiasme en nieuwe ideeën, en peptalk voor als ik het allemaal even niet meer zag zitten met mijn onderzoek. Ik voelde me bij jou vrij om elke mogelijke discussie aan te gaan en ik denk dat dit cruciaal is voor het vormen van een wetenschappelijke en kritische attitude.

Een aantal mensen heeft mij tijdens het begin van mijn promotie bijzonder goed wegwijs gemaakt in de imaging MS in het algemeen, en de op AMOLF gebruikte technieken in het bijzonder. Hiervoor wil ik Liam McDonnell en Maarten Altelaar in het bijzonder bedanken, maar ook de rest van de groep heeft mij daarbij geholpen. From the industrial side of the project, I had the pleasure to work with Tony Jackson and Ian Fletcher from the Measurement Science Group of ICI, which is now part of Intertek. Thank you both for the fruitful discussions. Special thanks to Ian for sharing your enormous experience while doing experiments together.

Mijn eerste paper schreef ik samen met Alexander Broersen. Alex, bedankt voor de prettige samenwerking, waarbij we af en toe moeite moesten doen om elkaars expertisegebied helemaal te doorgronden, wat het wat mij betreft juist zo leuk maakte. Ik vond dat een erg leuke en nuttige ervaring.

In the last year of my PhD project, I had the pleasure to collaborate with one of the greatest pioneering groups of the SIMS society, the surface analysis group headed by Prof. John Vickerman. The weeks I spent with Nicholas Lockyer of the University of Manchester to get their  $C_{60}$  gun and our delay line detector work together were not only enjoyable and instructive, but eventually also very successful. Also the visit in Manchester was pleasant and productive.

Na mijn afstuderen in Eindhoven kon ik toch nog niet helemaal afscheid nemen van de UPy's. Patricia Dankers, ik vond het ontzettend leuk om weer met jou samen te werken, deze keer ieder vanuit een verschillend expertiseveld, jouw enthousiasme stimuleert enorm. Ik ben in dezen ook dank verschuldigd aan Eliane Popa van UMC

Groningen. Verder heeft Marjolein Sanders bij het AMC macrofagen voor ons gegroeid, and we had fruitful discussions with Kris Reedquist on our study and the challenges we were facing. Thanks to both of you!

Terug naar AMOLF was daar altijd de sterke ondersteuning die AMOLF als instituut onderscheidt en het soort onderzoek dat gedaan wordt mogelijk maakt: uitdagend, vernieuwend en technologisch gezien soms op het randje van wat mogelijk is. Ivo heeft ontzettend veel data analyse software geschreven: onmisbaar als je imaging MS experimenten doet. Gert is er met zijn immer-verder-ontwikkellende data-analyse software. Verder is er natuurlijk de elektronica afdeling waarin ik vooral veel met Duncan en Ronald heb gewerkt, en de rest van de softwareondersteuning en de afdeling ICT. Binnen de groep heb ik heel veel hands-on techniek geleerd van Frans en vooral ook veel plezier gehad aan onze samenwerking. Frans, bedankt voor je inzet en humor! Natuurlijk was daar ook de hulp van Marc en als dat zo uitkwam van onze bijna-groepsgeenoot Jerre. Verder dank ik mijn kamergenoten Başak (inclusief frequent bezoeker Han-Kwang), Romulus, Luke, Lara, en in de nieuwbouw Andrei voor het plezier, het gedeelde lief en leed en de (wetenschappelijke) discussies. Met de rest van mijn collega's heb ik veel plezier beleefd aan wetenschappelijke, en vooral ook niet-wetenschappelijke activiteiten. Sander, Stefan, Maarten, Liam, Ioana, Don, Rimco, Erika, Aleksey, Yuri, Joe, Martin, Kamila, Julia, Andras Karelia, Piet, Jaap en Frank en alle frequente en minder frequente bezoekers: jullie hebben allemaal op jullie manier bijgedragen aan dit proefschrift. Rest mij nogmaals de sfeer en ondersteuning bij AMOLF die het werken zo plezierig maken te roemen. De mensen waarmee ik ruim twee jaar PV activiteiten heb georganiseerd zorgden voor leuke ontspanning-door-inspanning (dat laatste met name in de decembermaand). De administratieve ondersteuning, de bibliotheek, de mensen van de werkplaats en de tekenkamer, de technische dienst, de kantine en last-but-not-least de huishoudelijke dienst zijn allemaal bereid constructief mee te denken om het onderzoek en alles daaromheen zo soepel mogelijk te laten verlopen.

Ook buiten AMOLF om heb ik steun gehad in mijn werk. Mijn (schoon)familie en vrienden wil ik dan ook bedanken voor hun steun, begrip en interesse. Het is ook niet voor niets dat ik dit boekje heb opgedragen aan mijn ouders die mij altijd hebben gesteund en gestimuleerd in wat ik voor mijn studie deed.

Als laatste wil ik mijn schat van een vrouw bedanken. Annelies, ik had aan het begin van mijn promotie niet gedacht dat ik in die vier jaar de ideale vrouw tegen zou komen en ook nog eens met haar zou trouwen. Dat is toch gebeurd, en dat is niet voor niets. Je bent mij tot grote steun geweest, met name in de laatste maanden waarin ik je soms niet de aandacht kon geven die je verdient. Ik prijs me elke dag weer gelukkig met jou.

## CURRICULUM VITAE

Leendert Aart (Lennaert) Klerk werd geboren op 6 december 1982 in Eindhoven. Na het afronden van het VWO aan het Ichthus College te Veenendaal in 2000 koos hij voor een dubbele studie natuurkunde en scheikunde aan de Universiteit Utrecht. In de afrondende fase van deze studie deed hij onderzoek naar de groeiprocessen van plasma-gedeponeerde silicium zonnecellen met behulp van massaspectrometrie. Verder ging hij als uitwisselingsstudent naar de University of Florida (USA) om daar vakken te volgen in de richting van de biomedische technologie en biomateriaalkunde en deed hij een stage bij het Medtronic Bakken research center in Maastricht. Zijn afstudeeronderzoek deed hij aan de TU Eindhoven in de groep van prof. E.W. (Bert) Meijer aan supramoleculaire polymeren voor biomedisch gebruik. Na het behalen van beide doctoraal diploma's in 2005 ging hij als onderzoeker in opleiding (OIO) aan de slag bij het FOM instituut AMOLF in Amsterdam. Hier deed hij in de groep "macromolecular ion physics" van prof. Ron M.A. Heeren onderzoek op het gebied van plaatsopgeloste massaspectrometrie, gericht op karakterisatie van polymeersystemen. Dit onderzoek heeft geresulteerd in verschillende publicaties in internationale vaktijdschriften alsmede presentaties op nationale en internationale conferenties. De resultaten van dit onderzoek zijn samengevat in dit proefschrift en worden op 9 december 2009 verdedigd aan de Universiteit Utrecht.



## LIST OF PUBLICATIONS

### *Publications*

- **L.A. Klerk, P.Y.W. Dankers, M.J.A. Van Luyn, M.E. Sanders, K.A. Reedquist, R.M.A. Heeren**, Mass spectrometric imaging of a polymeric hydrogel implant, *in preparation*. **(chapter 7)**
- **L. A. Klerk, N. P. Lockyer, A. Kharchenko, L. MacAleese, P. Y. W. Dankers, J. C. Vickerman, R. M. A. Heeren**, Full-current  $C_{60}^+$  secondary ion MS microscopy using a delay line detector, *Analytical Chemistry*, submitted. **(chapter 5)**
- **L. A. Klerk, A.F.M. Altelaar, M. Froesch, L.A. McDonnell, R.M.A. Heeren**, Fast and automated large-area imaging MALDI mass spectrometry in microprobe and microscope mode, *International Journal of Mass Spectrometry*, 285 (2009) 25. **(chapter 4)**
- **L. A. Klerk, A. Broersen, I. W. Fletcher, R. van Lieere, R. M. A. Heeren**, Extended data analysis strategies for high resolution imaging MS: New methods to deal with extremely large image hyperspectral datasets, *International Journal of Mass Spectrometry, Imaging Mass Spectrometry Special Issue* 260 (2007)222. **(chapter 6)**
- **J. K. Rath, L. A. Klerk, A. Gordijn, R. E. I. Schropp**, Mechanism of hydrogen interaction with the growing silicon film, *Sol. Energy Mater. Sol. Cells* 90 (2006)3385.

### *Presentations at conferences*

- 2009 “Mass spectrometry as an imaging tool for elucidating the foreign body response to polymer implants” (poster), *22nd European Conference on Biomaterials*, Lausanne, Switzerland.
- 2009 “Imaging mass spectrometry of the foreign body response to polymer implants” (oral), *International Mass Spectrometry Conference*, Bremen, Germany.
- 2009 “High resolution C-60 SIMS and MALDI microscopy using a Delay Line Detector”, (oral), *56th ASMS Conference on Mass Spectrometry*, Philadelphia, Pennsylvania, USA.
- 2009 High resolution C-60 SIMS imaging”, (oral), *NVMS - BSMS 2009*, Rolduc, The Netherlands.

List of publications

- 2009 “Imaging Mass Spectrometry at the Interface of Biology and Polymers“, (poster), *Physics@FOM*, Veldhoven.
- 2008 “Bringing Imaging Mass Spectrometry from Biology to Synthetics”, (oral), *56th ASMS Conference on Mass Spectrometry*, Denver, Colorado, USA.
- 2007 “Imaging techniques for the analysis of polymers and polymer additives”, (poster), *Sanibel Conference on Imaging Mass Spectrometry*, Sanibel Island, Florida, USA.
- 2006 “Imaging Mass Spectrometry of Complex Polymeric Systems”, (oral), *International Mass Spectrometry Conference*, Prague, Czech Republic.